Characterization of the size-dependent indentation behavior and dislocation structures of single-crystalline tungsten

Zur Erlangung des akademischen Grades einer
Doktorin der Ingenieurwissenschaften (Dr.-Ing.)
von der KIT-Fakultät für Maschinenbau des
Karlsruher Instituts für Technologie (KIT)

genehmigte
Dissertation
von

M.Sc. Jin Wang

Tag der mündlichen Prüfung:	19. Januar 2021
Referent:	Prof. Dr. rer. nat. Oliver Kraft
Korreferentin:	Prof. Dr. rer. nat. Ruth Schwaiger
Korreferentin:	Prof. Dr. mont. Sabine Weygand

Kurzfassung

Wolfram hat den höchsten Schmelzpunkt aller Metalle sowie einen sehr geringen Ausdehnungskoeffizienten und hervorragende Wärmeleitfähigkeit. Wolfram und seine Legierungen sind damit sehr vielversprechende Kandidaten für den Einsatz als Strukturwerkstoff bei hohen Anwendungstemperaturen, insbesondere in Anwendungen der Energietechnik. Die Sprödigkeit bei Raumtemperatur und der Spröd-duktil-Übergang, der weit oberhalb der Raumtemperatur stattfindet, stellen allerdings limitierende Faktoren dar. Um die Eigenschaften von wolframbasierten Werkstoffen bei Raumtemperatur gezielt zu beeinflussen, ist ein umfassendes Verständnis der Verformungsmechanismen notwendig. Im Rahmen dieser Arbeit wurden verschiedene Eindruckverfahren eingesetzt mit dem Ziel die Größeneffekte bei der plastischen Verformung von einkristallinem Wolfram sowie die damit verbundenen Versetzungsstrukturen zu untersuchen. Die Charakterisierung der Versetzungsmikrostruktur wurde unter Verwendung von Transmissions-Kikuchi-Beugung in einem Rasterelektronenmikroskop durchgeführt.

Die Härte zeigt eine ausgeprägte Abhängigkeit von der Eindringtiefe, wobei der Härteverlauf nicht durch die bekannten Modelle beschrieben werden kann. Unter Berücksichtigung der sich ausbildenden Versetzungsstruktur wird im Rahmen dieser Arbeit ein neues Modell eingeführt, welches das beobachtete Verhalten beschreibt. Zur Analyse der Versetzungsstrukturen wurden Härteeindrücke mit einer keilförmigen Spitze durchgeführt, wobei der Keil so ausgerichtet wurde, dass das verformte Volumen einen ebenen Dehnungszustand aufwies. Damit konnten die Versetzungsstrukturen unter Anwendung

des Kröner-Nye Tensors quantitativ beschrieben werden. Die Dichte der geometrisch notwendigen Versetzungen wurde für die verschiedenen Gleitsysteme identifiziert und die Ausbildung von Kleinwinkelkorngrenzen bei großen Eindringtiefen beobachtet. Die Verteilung der geometrisch notwendigen Versetzungen zeigt deutliche Unterschiede für kleine und große Eindringtiefen. Bei großen Eindringtiefen sind die Versetzungsstrukturen vergleichbar zum Rissspitzenfeld eines stationären Risses. Die Versetzungsaktivität wurde weiterhin durch Variation der Belastungsgeschwindigkeit untersucht. Bei Raumtemperatur zeigen die mit der Versetzungsnukleation verbundenen Größen keine Abhängigkeit von der Belastungsrate. Im Gegensatz dazu nimmt das Aktivierungsvolumen mit zunehmender Eindringtiefe zu, bis ein Plateauwert erreicht wird, der von der Kristallorientierung abhängt und die Ausbildung von Kink-Paaren für die verschiedenen Gleitsysteme reflektiert.

Abstract

Tungsten has the highest melting point of all metals as well as a very low coefficient of thermal expansion and excellent thermal conductivity. Tungsten and its alloys are therefore very promising candidates for use as structural materials at high application temperatures, especially in energy applications. However, the brittleness at room temperature and the brittle-to-ductile transition, which takes place well above room temperature, are limiting factors. In order to tune the properties of tungsten-based materials at room temperature, a comprehensive understanding of the deformation mechanisms is necessary. In the context of this work, various indentation methods were used with the aim of investigating the size effects during the plastic deformation of single-crystal tungsten and the associated dislocation structures. The characterization of the dislocation microstructure was performed using transmission Kikuchi diffraction in a scanning electron microscope.

The hardness shows a pronounced dependence on the penetration depth, while the hardness curve cannot be described by the known models. Taking into account the developing dislocation structure, a new model is introduced in this thesis that describes the observed behavior. To analyze the dislocation structures, indents were made with a wedge-shaped tip, with the wedge aligned in such a way that the deformed volume exhibited a plane strain condition. This allowed the dislocation structures to be described quantitatively using the Kröner-Nye tensor. The density of the geometrically necessary dislocations was identified for the various slip systems and the formation of low-angle grain boundaries at larger penetration depths was observed. The distribution of the geometrically necessary dislocations shows clear differences for small

and large penetration depths. At higher depths, the dislocation structures are comparable to the crack tip field of a stationary crack. The dislocation activity was further investigated by varying the rate of loading. At room temperature, the variables associated with dislocation nucleation show no dependence on the loading rate. By contrast, the activation volume increases with increasing penetration depth until a plateau value is reached, which depends on the crystal orientation and reflects the formation of kink-pairs for the various slip systems.

Danksagung

Die vorliegende Dissertation dokumentiert den Hauptteil meiner Arbeit als Doktorandin am Institut für Angwandte Materialien - Werkstoff- und Biomechanik (IAM-WBM) im Rahmen des kooperativen Promotionskollegs „Gefügestrukturanalyse und Prozessbewertung". Ohne die Unterstützung und Mithilfe meiner Kollegen/-innen und Freunde wäre die Verwirklichung dieser Arbeit nicht möglich gewesen.

Zuerst gilt mein besonderer Dank Herr Prof. Dr. Oliver Kraft, Frau Prof. Dr. Ruth Schwaiger und Frau. Prof. Dr. Sabine Weygand für die Übernahme der Haupt- und Korreferate. Bei Herrn Prof. Dr. Kraft möchte ich mich für die Vorstellung dieses Forschungsthemas, die stetige Ermutigung und sein Vertrauen bedanken. Bei Frau Prof. Dr. Schwaiger bedanke ich mich für das Angebot der Promotionsarbeit, wissenschaftliche Diskussionen und Betreuung, ihr Vertrauen, ihre Unterstützung und Freundschaft. Darüber hinaus bedanke ich mich bei Frau Prof. Dr. Weygand für fachliche Diskussionen und den Austausch im Rahmen des kooperativen Projekts.

Ebenfalls möchte ich mich bei Herrn Prof. Dr. Ulrich Maas für die Übernahme des Vorsitzs meiner Verteidigung und mündlichen Prüfung bedanken.

Im Besonderen bedanke ich mich bei meinem Projektpartner Dr. Tillmann Volz für die kooperative Zusammenarbeit, sowie bei meinen ehemaligen Zimmerkollegen Dr. Stephan Weyand, Dr. Likang Luan, und Frau Alexandra Wahn für die freundschaftliche und kreative Arbeitsumgebung.

Bei Dr. Moritz Wenk und Herrn Thomas Kreuter bedanke ich mich für die Einweisung in die Mikroskopie und EBSD, und bei Herrn Prof. Dr. Marc Kamlah, Frau Jana Herzog, Herrn Ewald Ernst, Frau Exner Daniela, Frau Gabriele Rizzi für administrative und technische Unterstützung am IAM-WBM. Ebenso danke ich Dr. Christian Greiner und Dr. Zilong Liu für ihre Hilfe und den Zugang zur REM am IAM-CMS.

Mein Dank gilt ebenfalls den Teamkollegen der Gruppe Schwaiger für ihre vorbildlichen Arbeiten, unsere gegenseitige Unterstützung, die vielfältigen und wissenschaftlichen Diskussionen und die freundschaftliche Zusammenarbeit. Des weiteren gilt die Kollegen am IAM-WBM mein Dank für die schöne Zeit.

Vor allem aber danke ich meiner Familie für ihre bedingungslose Unterstützung und das Verständnis für die gesamte Zeit meines Studiums und meiner Promotion in Karlsruhe, die trotz großer Sehnsucht mich stets bekräftigt haben. Mein Dank gilt ebenfalls meinem Freund Chia-Yu Wu für die Ermutigung, und meiner Freundin Fangfei Li für den Rückhalt. Ich bedanke mich bei den Beiden für ihre Liebe und Geduld, die Begleitung und unsere gemeinsamen Erlebnisse.

Nicht zuletzt bedanke ich mich für die Finanzierung des kooperativen Promotionskollegs bei Karlsruhe House of Young Scientists (KHYS) und dem Ministerium für Wissenschaft, Forschung und Kunst Baden-Württemberg, sowie bei Frau Prof. Dr. Schwaiger und dem IAM-WBM für die Finanzierung meiner konferenzteilnahme. Manchmal liegt der Sinn der Forschung nicht nur in den praktischen Applikationen, sondern auch darin die fundamentalen Fragen zu beantworten. Ohne solche Finanzierung verliert die Wissenschaft teilweise die Erde der Neugier, Kreativität und Vielfältigkeit.

Diese Dissertation entstand im Jahr 2020. Das Jahr 2020 war ein trauiges und schwieriges Jahr für die gesamte Menschheit, dennoch verlangen diese besonderen Zeiten die Solidarität und Verantwortung aller. Ich bedanke mich deshalb

abschließend ebenfalls bei allen medizinischen Mitarbeitern und Mitarbeiterinnen, sowie dem fachlichen Personal, die gegen diese Pandemie kämpfen und gekämpft haben.

Düren, im Januar 2021 *Jin Wang*

List of abbreviations and symbols

Abbreviations

2D	two dimensional
3D	three dimensional
BC	band contrast
bcc	body-centered cubic
BDT	brittle-to-ductile transition
BDTT	brittle-to-ductile transition temperature
CDF	cumulative distribution function
CLR	constant loading rate
CLRT	constant loading rate test
CMSG	conventional mechanism-based strain gradient plasticity
CSM	continuous stiffness measurement
CSR	constant strain rate
CSRT	constant strain rate test
DCM	dynamic contact module
e^-	electron
EBSD	electron backscatter diffraction
ECCI	electron channeling contrast imaging
EI	elastic-interaction
fcc	face-centered cubic
FIB	focused ion beam
GND	geometrically necessary dislocation

IPF	inverse pole figure
ISE	indentation size effect
KAM	kernel average misorientation
LAGB	low angle grain boundary
LT	line-tension
ND	normal direction
RD	rolling direction
SEM	scanning electron microscopy
SGP	strain gradient plasticity
SSD	statistically stored dislocation
TD	transverse direction
TEM	transmission electron microscopy
TKD	transmission Kikuchi diffraction

Elements

Ag	silver
Al	aluminum
Cu	copper
Ga, Ga^+	gallium, gallium ion
Ir	iridium
MgO	magnesium oxide
Mo	molybdenum
NaOH	sodium hydroxide
Pt	platinum
SiC	silicon carbide
W	tungsten

Latin characters

$\dot{P}$	loading rate
A	projected contact area
a	indent tip contact radius

b, b_i	Burgers vector
D, d	neighboring dislocation distance of KAM
E	Young's modulus
E_r	reduced modulus
f	cumulative distribution function
H	hardness
h	indentation depth
h^*	characteristic material length scale
H_0	depth-independent macroscopic hardness
h_0	transition depth of bi-linear ISE model
$h_{\{110\}}$, $h_{\{112\}}$	kink height between {110} and {112} slip planes
h_c	contact depth of indent
h_kink, λ^*	kink height, kink width
i, j	number of axes in coordinate system
k	Boltzmann constant
m	strain rate sensitivity
m_0, ... m_n	indent tip calibration parameter
n	proportion of saturated volume in total GND volume
N_0	attempt frequency of nucleation event
P	load
P_m	maximum pressure
$P_\mathrm{pop-in}$	pop-in load
R	indent tip radius
r	position of dislocation loop
r_0	radius of saturated GND volume
R_a	arithmetical mean roughness value
S	stiffness
s, $s(r)$	uniform and non-uniform dislocation loop spacing
T	temperature
t, t_j	dislocation line vector
T_m	melting temperature

V	GND volume
V^*	activation volume
V_y^*	activation volume of yielding
wt%	weight percent
(x_1, x_2, x_3), (x, y, z)	coordinate system
dx, ∂x	step size of EBSD and TKD measurement

Greek characters

$\dot{\varepsilon}$	indentation strain rate
α	dislocation parameter
α_{ij}	dislocation tensor
β	indent tip geometry factor
$\Delta\theta$	bending angle
$\dot{\tau}$	stress rate
κ_{ij}	curvature tensor
λ, $\lambda(r)$	total length of dislocation loops
μ	shear modulus
ν	Poisson's ratio
π	Pi
ρ	dislocation density
ρ_G	GND density
ρ_{KAM}	local GND density of KAM
ρ_S	SSD density
ρ_{total}	total GND density
σ	flow stress
σ_0, σ_P	Peierls stress
τ	shear stress
θ	indent tip contact angle
ε	activation energy
ξ	coordinate of dislocation core
$V(\xi)$	Peierls potential

$(\varphi_1, \Phi, \varphi_2)$, $(\mathrm{d}\varphi_1, \mathrm{d}\Phi, \mathrm{d}\varphi_2)$	Bunge Euler angles, deviation of Euler angles
$\mathrm{d}\theta$, $\partial\theta$	misorientation

Contents

1 Introduction

With the development of the industrialization worldwide, the materials of promising application prospects, especially the metallic materials were in higher demand since the middle of the last century [1]. Interests increase in studying the metals of great mechanical properties, and their reliability under extreme conditions, such as high temperature. Tungsten is one of the most essential candidates of the structural materials for the applications at high temperature due to its outstanding mechanical properties at temperature >1400°C [2]. Nevertheless, there are still some uncertainties left in the underlying mechanisms of the mechanical behaviors of tungsten.

To be able to understand the mechanical behaviors of materials, various measurement techniques were developed. During the developing of the characterization techniques, people realized that the macroscopic properties of the materials are notably influenced by their microstructures, such as grains and dislocations [3–5]. Also, if the size of the material varies, its properties might vary, too [6]. In the last decades, relevant mechanical properties like Young's modulus and hardness could be determined with higher accuracy at the length scales of the micrometer to the nanometer range using the nanoindentation technique [7, 8]. For many materials including single-crystalline tungsten, their hardness values increase with decreasing indentation depth [9, 10]. The so-called indentation size effect (ISE) is associated with the dislocation density, i.e. the geometrically necessary dislocation (GND) density, in the material [9, 11, 12].

The quantitative characterization of the ISE of single-crystalline tungsten is not only a proper approach to understand the underlying mechanisms of the dislocation activities in tungsten, but can be applied to materials of the similar crystal structure. With the help of material characterization methods, such as scanning electron microscopy (SEM), electron backscatter diffraction (EBSD), and transmission Kikuchi diffraction (TKD), the dislocation structures can be visualized and the density quantitatively determined [13, 14]. In this work, a model describing the ISE of single-crystalline tungsten is presented and discussed. Then, the indentation-induced dislocation structures are quantitatively characterized using the TKD measurement. The model is validated by the experimental results of the hardness and the dislocation density determined from the nanoindentation and the the TKD measurement, respectively.

2 Background and literature overview

Tungsten has great potential as a structural material under extreme conditions, in particular because of its high melting point and its high specific strength above 1400°C [2]. Over the last decades,with the increasing requirements of the nuclear energy industry, where the high-temperature mechanical behaviors of materials play a dominating role, the investments into research on tungsten and tungsten alloys have been increasing [2, 15]. Although the strength and high temperature performance of tungsten are excellent, the material is brittle at room temperature [3, 4, 15]. The brittleness of tungsten and its fairly high brittle-to-ductile transition (BDT) above room temperature [3],have limited its application. Becoming the Achilles' heel of tungsten, it is therefore quite meaningful to study the mechanical behaviors, especially the plastic deformation behaviors below the BDT temperature (BDTT) of tungsten to the purpose of a better understanding of the underlying mechanisms.

According to literature by Gumbsch et al. and Rupp, [3–5], the mechanical properties of tungsten are significantly affected or even dominated by grain size and grain orientations. For polycrystalline tungsten it has been confirmed that the cracks generally occur at the grain boundaries, which would finally result in failure [5].

Recently, a series of micro-cantilever experiments of tungsten single crystals are reported to characterize the fracture behavior if single-crystalline tungsten with different crystal orientations [16–19]. According to the results by

Schmitt [16], in addition to an orientation dependency of the fracture properties, small size samples showed a significant size effect and notable plasticity compared to the larger samples [16]. However, fabricating micron-size cantilever samples for the bending test is complex and time-consuming, which limits its applicability for the study of size effects in the plastic deformation behavior.

In this work nanoindentation was employed to study the size effects in the plastic deformation of single-crystalline tungsten and the related dislocation activities. Nanoindentation has several advantages to offer as a micromechanical testing method [7,20], where the relatively easy sample preparation is probably the most prominent one. The microstructures underneath indentations to different depths were analyzed quantitatively using transmission Kikuchi diffraction (TKD).

2.1 Dislocation evolution in bcc metal: from nucleation to motion

In crystalline materials the plastic deformation is in general associated with dislocation activity. In a dislocation-free solid body, the evolution of dislocations would include firstly nucleation, then propagation, and motion towards a larger volume of material [21]. Activation volume V^* is a parameter characterizing the energy barrier of thermal related dislocation activities, such as nucleation, motion, and forest [22, 23]. Generally, it is a non-physical volume [21], but describes a concept of the threshold volume that a certain dislocation activity would occupy [22, 24, 25].

In a defect-free crystal, the homogeneous nucleation would occur, and the dislocation loop would nucleate in a defect-free volume [26–28]. However, the

homogeneous nucleation was rarely detected as it requires ideal purity and perfect crystallographic structure of the material. Typically, heterogeneous dislocation nucleation is observed in crystalline materials [21,24,29–31]. Both processes can be distinguished by the activation volume of yielding, i.e. V_y^* [24]. Compared to homogeneous nucleation, heterogeneous dislocation nucleation requires lower energy and a smaller activation volume [24], as the previously existed defects such as impurity atoms, vacancies and vacancy clusters, benefit the dislocation nucleation [21,32].

In nanoindentation testing, a distinct displacement burst can be observed in the load-displacement curve of a dislocation-free sample. The burst, also known as "pop-in" indicates the end of elastic behavior and the initiation of plastic deformation, and remarks the nucleation of dislocations [24,29,31,33,34]. The corresponding stress at this point [35,36] is equivalent to the yield stress in uniaxial mechanical testing and should be comparable to the theoretical strength of the respective method [37]. After nucleation, dislocations propagate and multiply, and their density increases dramatically. The mechanical properties such as flow stress or hardness are proportional to the square-root of the dislocation density, following the Taylor relation [38].

A body-centered cubic (bcc) unit cell with the possible slip systems is shown in Figure 2.1. Compared to face-centered cubic (fcc) materials (e.g. Cu, Ag, Al), the mechanical properties of bcc metals usually reveal a strong temperature dependence. Bcc metals tend to achieve less plasticity and ductility at lower temperature (below the BDT). Also, flow stress and hardness of bcc single crystals were reported to be strain rate sensitive, while such properties of fcc materials are independent of strain rate [39–41].

In fcc metals, plastic deformation is dominated by the motion of edge dislocations. Due to its planar core structure the edge dislocations can easily move along the 12 fcc slip systems {111}<110> [21,44]. On each slip plane, the glide of edge dislocations can occur along three axes in six directions. Also,

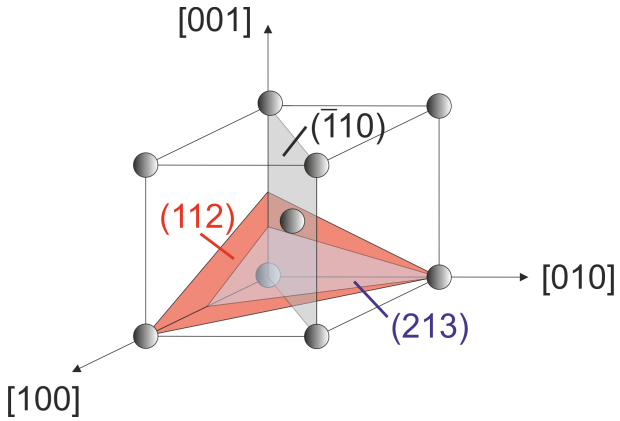

Figure 2.1
Bcc unit cell with the different possible slip systems. Examples for the slip planes of three possible slip system families, which are {110}, {112} and {123} are indicated with grey, red and blue planes. For the three slip system families, the slip direction is the same along <111>. The latter two slip system families are more difficult to activate at room temperature [42, 43].

the dissociation of full edge dislocations in fcc crystals enables the motion taking place at a favorable lower energy level due to the reduced square of Burgers vector b^2 of partial dislocations [45].

In bcc metals, while 12 main slip systems {110}<111> exist, the number of slip axes on each slip plane is reduced to two. Also, in addition to edge dislocations, screw dislocations contribute to the plastic deformation, too. Considering the parallel Burgers and line vectors of screw dislocations, their core structure is no longer planar [46–55]. This non-planar structures, which are less mobile at a lower temperature, determine the particular properties of bcc metals, such as the higher yield stress, and non-Schmid deformation behavior [44]. Due to the high stress that is required for moving the screw dislocations, a peculiar dislocation structure called kink-pair generate and are identified as the main dislocation mechanism governing the plastic deformation of bcc crystals [21]. Generally, the kink-pair nucleates and propagates along the screw dislocation lines, as schematically shown in Figure 2.2. This thermally activated process

is responsible for the macroscopic temperature and rate dependent mechanical behaviors of bcc metals and can be quantitatively characterized by the concept of activation volume V^*. Geometrically, activation volume of motion is the critical volume that one kink-pair would occupy [22, 25].

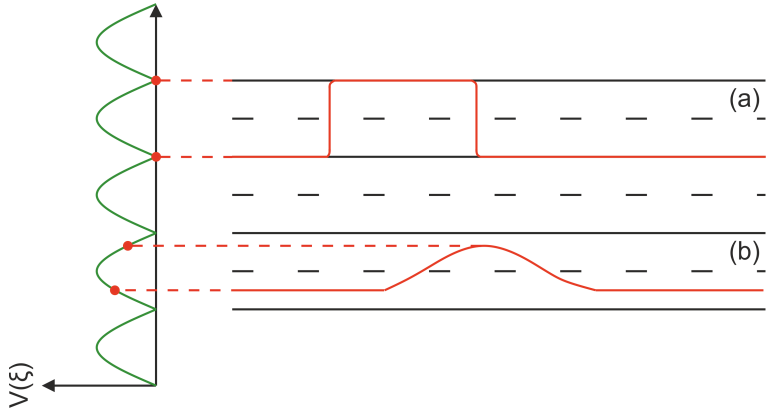

Figure 2.2
Schematic of two kink-pair models in bcc crystals [21, 44, 54]: (a) elastic-interaction (EI) model and (b) line-tension (LT) model. The red lines indicate the dislocation cores of the kink-pair. According to the Peierls potential indicated by the green line on the left-hand side, when the dislocation cores located on the Peierls valleys (black solid lines on the right-hand side), Peierls potential reaches the minimum. While in the middle of two Peierls valleys, the Peierls potential has the maximum called the Peierls hills (black dashed lines). In the case of EI model in (a), the screw dislocations locate on the Peierls valleys, while in LT model in (b), the dislocation cores can locate in-between.

The formation of kink-pair is thermal and related to the so-called Peierls potential [25] (see $V(\xi)$ in Figure 2.2), which describes the energy of the dislocation motion [21]. The Peierls potential $V(\xi)$ is usually waving with the coordinate of the dislocation ξ (see the red dots in Figure 2.2). For crystalline materials of certain slip systems, $V(\xi)$ reaches a minimum periodically with the minimum of $V(\xi)$ denoted as the Peierls valley [21, 44]. The distance between the neighboring Peierls valleys can be approximately estimated by the distance of

the corresponding slip planes [43]. Using this framework, the kink-pair structure can be described as shown in Figure 2.2: There are generally two models describing the kink-pair structure in the different temperature regimes, (Figure 2.2), i.e. the elastic-interaction (EI) model, and the line-tension (LT) model. In the high-temperature and low-stress regime, the kink-pair would fully develop (Figure 2.2(a)), while in the low-temperature and high-stress regime, the kink-pair cannot expand completely (Figure 2.2(b)) [21, 43, 44]. In the case of single crystalline tungsten, due to the high melting temperature, the kink-pair configuration of the EI-model is only possible at temperatures beyond 600 K. At room temperature, the LT-model describes the kink-pair dislocation activity [43].

2.2 Indentation size effect

The relation between hardness H, flow stress σ and dislocation density ρ can be described by the following equation [9, 38]:

$$H = 3\sigma = 3\sqrt{3}\alpha\mu b\sqrt{\rho}, \tag{2.1}$$

where α is a constant related to the dislocation structure, μ the shear modulus and b the magnitude of Burgers vector of a material. Macroscopically, the hardness of a crystalline material is usually size- and depth-independent. Reducing the length scale of indentation depth to the micrometer range, some materials, e.g., single-crystalline Cu, Ag, Ir, MgO and W, exhibit the so-called indentation size effect (ISE) meaning that the hardness H increases with decreasing depth h [10, 41, 56–66]. Several experimental reports indicate that the ISE is neither related to the crystal structure, nor to alloying elements, but rather dependent on the density of geometrically necessary dislocations (GNDs). In contrast to the statistically stored dislocations (SSDs), which are usually randomly distributed in a material through uniform straining, GNDs are associated with the

plastic strain gradients and cause an additional increase of strength or hardness. According to the strain gradient plasticity (SGP), strain gradients are inversely proportional to the length scale of plastic deformation, which is the depth in nanoindentation. Therefore, the influence of strain gradients, and the GNDs, become more pronounced when the length scale is reduced [11, 12].

There are several models to mathematically describe the ISE [9, 62, 63, 67, 68], among which the Nix-Gao model [9] is probably the one most widely discussed and applied. Based on SGP, Nix and Gao assumed that the GNDs are concentrated uniformly beneath a conical indenter tip in a hemispherical volume, the size of which is defined by the contact radius of indenter a. Based on this assumptions, the total length of dislocation loops and the dislocation density can be determined. In Figure 2.3, the GND distribution according to the Nix-Gao model is shown schematically [9].

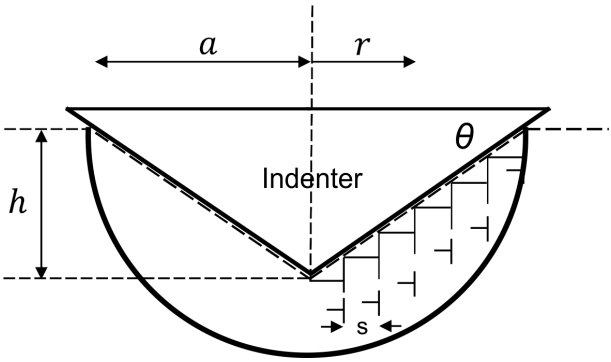

Figure 2.3
Schematic of the GND distribution beneath a conical indenter tip of contact angle θ according to Nix-Gao model [9]. The GND distribution is symmetrical, and for the sake of clarity, only the dislocations on the right hand side are illustrated.

The spacing between two slip steps s has been assumed constant and can be written as:

$$s = \frac{\mathrm{b}}{\tan\theta} = \frac{\mathrm{b}a}{h}. \tag{2.2}$$

Thus, the length of a dislocation loop at the position r can be written as:

$$\mathrm{d}\lambda = 2\pi r \frac{\mathrm{d}r}{s} = 2\pi r \frac{h}{\mathrm{b}a}\mathrm{d}r, \tag{2.3}$$

and the total length of dislocation loops in the GND volume is:

$$\lambda = \int_0^a \frac{h}{\mathrm{b}a} 2\pi r \mathrm{d}r = \frac{\pi h a}{\mathrm{b}}. \tag{2.4}$$

Note that the uniform dislocation spacing s according to equation (2.2) is the minimum value between two full GNDs, which indicates that in the Nix-Gao model, GNDs are closely packed in the hemispherical volume. Under this condition, the GND density as well as the hardness as suggested by the model are upper limits and associated with the size $V = 2/3\pi a^3$ of the GND volume. Accordingly, the GND density ρ_{G} according to the Nix-Gao model is:

$$\rho_{\mathrm{G}} = \frac{\lambda}{V} = \frac{3h}{2\mathrm{b}a^2} = \frac{3}{2\mathrm{b}h}\tan^2\theta. \tag{2.5}$$

As the total dislocation density ρ is a sum of GND density ρ_{G} and SSD density ρ_{S}, equation (2.1) can be rewritten like:

$$H = 3\sigma = 3\sqrt{3}\alpha\mu\mathrm{b}\sqrt{\rho_{\mathrm{S}} + \rho_{\mathrm{G}}}. \tag{2.6}$$

The square of hardness H^2 can be represented as

$$H^2 = {H_0}^2 + {H_0}^2 \cdot \frac{h^*}{h} \tag{2.7}$$

with the depth-independent hardness (macroscopic hardness) H_0 only depended on ρ_{S}

$$H_0 = 3\sqrt{3}\alpha\mu\mathrm{b}\sqrt{\rho_{\mathrm{S}}} \tag{2.8}$$

and a characteristic length scale h^*

$$h^* = \frac{81}{2} \mathrm{b}\alpha^2 \tan^2\theta \left(\frac{\mu}{H_0}\right)^2. \tag{2.9}$$

With the further development of indentation testing techniques, the classical model revealed some shortcomings for the case of nanohardness [59, 60, 62–64, 66]. At indentation depths of a few hundred nanometers, an overestimation of the model to the hardness data for some materials was observed [41, 59, 60, 62–64, 66, 67]. Focusing on understanding this breakdown, two major ideas were brought forward and discussed. The first one suggested that the GNDs would spread towards a larger volume than predicted [59,62,63], i.e. the size of the hemispherical volume V is larger than $2/3\pi a^3$. To determine the expanded GND volume, Durst et al. [62–64, 66] introduced a material-dependent factor f to describe the extension of the plastic zone:

$$f = \frac{a_{\mathrm{PZ}}}{a}, \tag{2.10}$$

where a_{PZ} is the effective radius of the extended plastic zone. Consequently, GND density would be reduced due to the larger volume

$$\rho_{\mathrm{G,PZ}} = \frac{\lambda}{V_{\mathrm{PZ}}} = \frac{3}{2f^3 \mathrm{b}h} \tan^2\theta \tag{2.11}$$

and the characteristic length scale h^* is rewritten as:

$$h^*_{\mathrm{PZ}} = \frac{81}{2f^3} \mathrm{b}\alpha^2 \tan^2\theta \left(\frac{\mu}{H_0}\right)^2. \tag{2.12}$$

According to Durst et al. [62–64,66], the plot of H^2 versus $1/h$ is still linear but the slope is decreased. The modified model was compared with nanohardness data of different materials and provided a better description than the classical model at the smaller depths [62–64, 66]. Nevertheless, the reported f, which varied between 1.5 to 2.5, was often determined by fitting experimental data

and not based on a direct observation. The model [62,63] is therefore regarded rather as empirical than physics-based as mentioned by Pharr et al. [10].

The second approach to fix the overestimation at small depth of the classical model is to assume the existence of an upper limit of GND density in the deformation volume [67]. Respecting the non-linear ISE that was observed on Ir and MgO, they had set a limited GND density empirically, then repeated applying their model with the conventional mechanism-based strain gradient plasticity (CMSG) finite element analysis on the experimental data of both materials, until the best fit was achieved. For Ir and MgO, the maximum GND density is approximately determined as 1×10^{15} m^{-2} and 1×10^{16} m^{-2}, respectively. Due to the upper limit, the relationship between H^2 and $1/h$ is no longer linear. However, this non-linear ISE model is still controversial, since the determined maximum GND density for MgO was too high [10,63], and the experimentally observed non-linear ISE could have been an artifact related to the testing techniques e.g., the continuous stiffness measurement (CSM) or a blunt tip [10,63,69–71].

However, the non-linear ISE, has been observed for a range of materials, including bcc metals [63, 68]. For bcc metals, the non-linear ISE could result from the non-negligible internal friction stress, namely the Peierls stress [68, 72]. Accounting for the Peierls stress within the framework of SGP, the relation of H^2 to $1/h$ becomes parabolic, instead of linear.

Observations of the ISE of different single-crystalline materials [36,41,56–63] and the corresponding models discussed over the last decades [9,62,63,67,68] are summarized in Figure 2.4.

In some cases, the different models cannot capture the ISE on different length scales from the micron to the sub-micron regime, except for the model introduced by Huang et al. [67] whose parameters were determined by fitting experimental data. Another fact to be noticed is that hardness data, which were not determined from CSM also reveal non-linear behavior, such as the Cu data obtained by McElhaney et al. [57] or W and Mo data from Maier

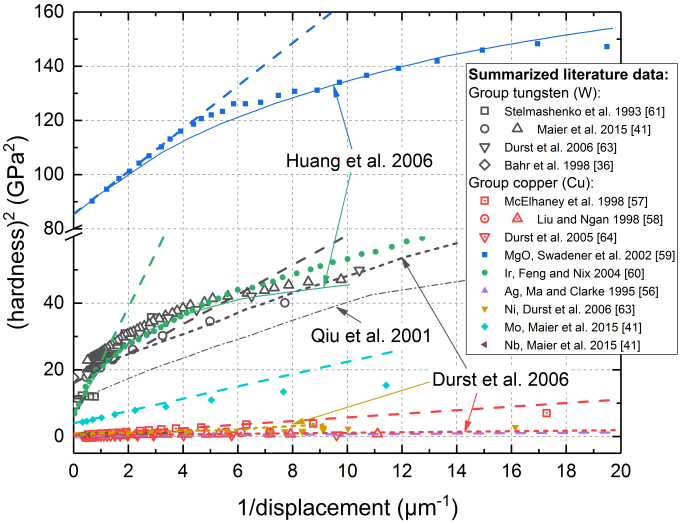

Figure 2.4
ISE of different single-crystalline materials [36, 36, 41, 56–63] and ISE models [9, 62, 63, 67, 68] in a plot of H^2 to $1/h$. The dashed lines show the prediction of the Nix-Gao model. Several data sets in the literature exhibit obvious bi-linear behavior.

et al.'s work [41] (Figure 2.4), which were determined by loading/unloading cycles. Some studies of the microstructure of indented materials, employing transmission electron microscopy (TEM) and electron backscatter diffraction (EBSD) taken on the cross section of deformed areas, indicated differences of the dislocations including GND structures at different length scales between sub-micron and several microns [73–76]. At smaller indentation depth, both TEM and EBSD captured lower dislocation densities than that predicted by the Nix-Gao model. Such observation evidenced that the non-linear ISE was not caused by the CSM techniques or tip blunting, but might be related to a change of dominant hardening mechanisms.

2.3 Quantifying dislocation density in SEM

Transmission electron microscopy is a powerful technique to visualize and analyze dislocation structures at high resolution [77]. The sample preparation is rather time consuming, though, and the information quite local.

Dislocations can also be investigated by electron channeling contrast imaging (ECCI) [78], which involves easier sample preparation. While the defects on the surface, such as dislocations and stacking faults are nicely visible over a wider area in scanning electron microscope (SEM), this technique is highly dependent on the microscope and requires a parallel electron beam with high resolution. ECCI is well-suited to qualitatively study the morphology and the structure of dislocations, but less applicable to determine the dislocation density [78–82].

Another classic method to observe dislocations are "etch pits" [21]. At the locations on the sample surface where dislocations emerge the etching rate is higher due to the strain energy of the dislocation, while results in pits on the surface [21]. The dislocations are thereby magnified and can be traced by such etch pits, which are easily detected in SEM or even under the optical microscope. This technique was very popular in the 1950s and was applied on many different crystalline materials [83, 84]. Recently, the etch pits method was applied to study the distribution of dislocations induced by nanoindentation on ceramic single crystals [85–87]. While dislocation pile-ups and expansion of dislocations could be detected on the sample surface, the dislocation density was difficult to quantify considering the overlap of etch pits due to the magnification of the dislocations. Moreover, etch pits give surface information rather than information regarding the cross section, whereas the latter would be more interesting for studying the ISE mechanism.

Focusing on quantitative characterization of the GNDs, a series of publications introduced the EBSD method as a suitable approach since it can be used to analyze a fairly large sample area yielding, e.g., information regarding the crystal

type, crystallographic orientation and local misorientation [14, 73, 88–103]. In SEM, the sample is scanned by the electron beam and the diffracted, backscattered electrons at each scanning point are collected and analyzed. The resulting diffraction pattern, also known as Kikuchi pattern [104] contains information about lattice distance and direction so that the crystal type and orientation of the sample can be identified. Since the crystallographic orientation at each point is determined, the difference between the individual points, which is the local misorientation, can be determined. Based on the EBSD method, a refined microstructural characterization operating in transmission, i.e. transmission Kikuchi diffraction (TKD), was developed [13, 105–108]. Still an TKD, SEM-based method, allows the analysis of microstructures at a higher resolution of less than 10 nm [105].

2.3.1 Kernel average misorientation (KAM)

GND density can be calculated if the local misorientation of a deformed zone is known. By introducing the low angle grain boundary (LAGB) model [109, 110], the misorientation angle can be associated with the spacing between dislocations, based on which the dislocation density can be defined. Accordingly, energy stored during the early stages of deformation at lower temperatures ($T \leq 0.3T_{\mathrm{m}}$, with T_{m} as the melting temperature) can be released by rearrangement of dislocations into certain configurations of lower energy. The dislocation configurations are the low angle grain boundaries [109, 110]. A simplified case of the tilt boundary consists of edge dislocations as illustrated in Figure 2.5. It was assumed that the GNDs were generated from plastic bending in the deformed region x at a total bending angle θ. The stored energy would not produce more dislocations but only drive the randomly distributed GNDs aligning along a line, "building a boundary". By rearranging the randomly distributed dislocations to aligned LAGBs, the bent bulk material can be separated

to smaller regions, in each exists an individual LAGB (Figure 2.5). Based on that, the dislocation density ρ can be further determined. [109, 110].

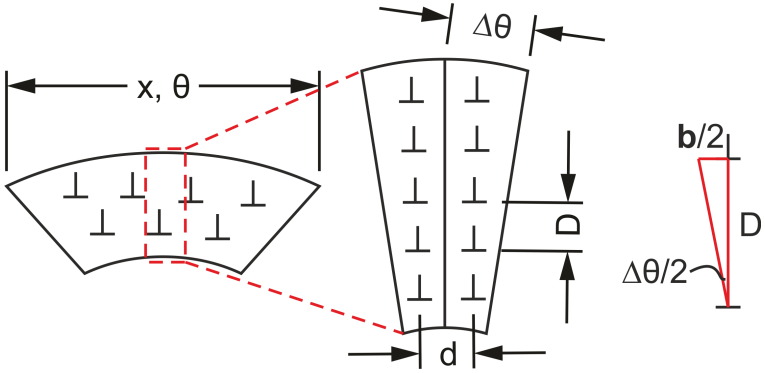

Figure 2.5
Schematic diagram illustrating the LAGB model [109, 110]. GNDs generated in crystal after a bending deformation and resulting LAGB due to the release of the stored energy. In each LAGB affected, small region, the small amount of bending angle is denoted as $\Delta\theta$, the spacing of two dislocations in the LAGB is D, while d denotes the spacing of two LAGBs. The Burgers vector of the dislocation is denoted as b.

According to the literature [109–111], spacing of two dislocations in the LAGB is geometrically dependent on the bending angle:

$$\tan\frac{\Delta\theta}{2} = \frac{\mathrm{b}/2}{D}, \tag{2.13}$$

with b and D as the Burgers vector of the dislocation and distance between two neighboring dislocations of the same LAGB, respectively. For small bending angles, $\tan(\Delta\theta/2) \approx \Delta\theta/2$, resulting in:

$$\Delta\theta \approx \frac{\mathrm{b}}{D}. \tag{2.14}$$

The total bending angle θ is easily calculated by multiplying $\Delta\theta$ by the total number of LAGBs N in the region x [88]:

$$\theta = N \cdot \Delta\theta \approx \frac{x}{d} \cdot \frac{\mathrm{b}}{D} = \frac{x\mathrm{b}}{dD} \tag{2.15}$$

with d the distance of two neighboring LAGBs. Therefore, the average spacing of dislocations d_{av} in region x is

$$d_{\mathrm{av}} = \sqrt{dD}. \tag{2.16}$$

The GND density is defined as:

$$\rho = \frac{1}{d_{\mathrm{av}}^2} = \frac{\theta}{x\mathrm{b}}. \tag{2.17}$$

For the case of screw dislocations, LAGB would also appear but turn to a form of twist boundary instead of tilt [109, 110]. The corresponding spacing of dislocations is the same as in the case of edge dislocations.

With EBSD or TKD, measuring local misorientation in a deformed area is accomplished by comparing the orientation of the center point, which is the so-called kernel, to its neighbor points. Depending on the number of neighboring points, the so-called kernel average misorientation (KAM) can be categorized as, for example, KAM4 and KAM8 as indicated in Figure 2.6.

The average misorientation $\mathrm{d}\theta_{\mathrm{av}}$ is the averaged value of $\mathrm{d}\theta_n$:

$$\mathrm{d}\theta_{\mathrm{av}} = \frac{\sum_n \mathrm{d}\theta_n}{n}, \tag{2.18}$$

where n is the number of neighbors as shown in Figure 2.6. The local GND density ρ_{KAM} at each kernel point is determined, according to equation (2.17) and (2.18):

$$\rho_{\mathrm{KAM}} = \frac{\mathrm{d}\theta_{\mathrm{av}}}{\mathrm{d}x\mathrm{b}}. \tag{2.19}$$

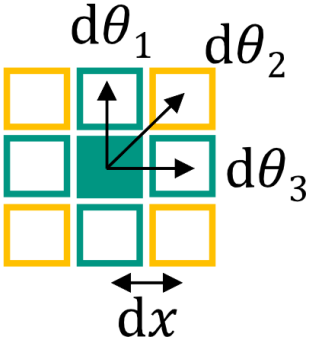

Figure 2.6
Schematic of the kernel average misorientation analysis [18]. For the case of KAM4 (indicated with green frames) and KAM8 (green and yellow frames), the orientation of the kernel point (solid green square) is compared to 4 and 8 neighboring points, respectively. $d\theta_i$ describes the misorientation in i direction. The distance between measured points is the step size dx.

Accordingly, the GND density is proportional to the misorientation. KAM analysis is often applied for 2D measurements, but the application could be extended to 3D cases depending on the EBSD results [14, 93–97, 112].

2.3.2 Nye and Kröner tensor

KAM analysis can be employed to determine the GND density through the average misorientation angle, though, this analysis could be regarded as a simple estimation of dislocation density [111]. Also, GND density determined by KAM is a mixed result of all slip systems [113]. Taking this into consideration, GND components relating to the individual slip systems can be estimated by the application of Nye-Kröner tensor [14, 98, 100, 101, 114, 115]. The Kröner tensor is written as:

$$\alpha_{ij} = \rho b_i \otimes t_j. \tag{2.20}$$

α_{ij} is the so-called dislocation tensor, which can be approximated by the curvature κ according to Nye's work [114]. b_i and t_j are the Burgers vector and the line vector of GND, respectively, referring to certain slip systems, which are known quantities as long as the slip system is defined. i and j are the number of axes describing the coordinate system.

Figure 2.7 shows a schematic of an indented sample coordinate system, with the TKD measurement points and the corresponding curvature vectors κ [98].

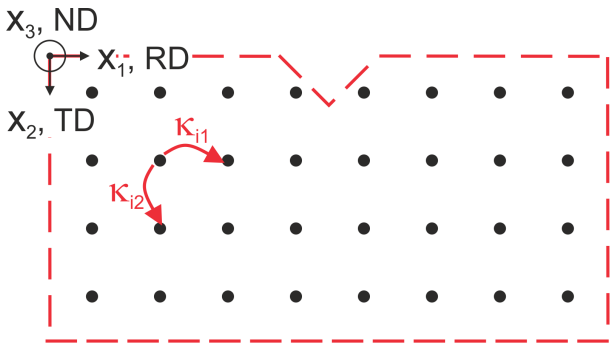

Figure 2.7
Determination of curvature κ after TKD measurement on the cross section of an indent. Black dots are the measuring points with their coordinates and orientations recorded. Here x_1 and x_2 are the two in-plane directions, namely the rolling direction (RD) and transverse direction (TD), respectively. x_3 is the normal direction (ND).

Thus, instead of averaging the misorientation of every kernel point as done in the KAM analysis, the curvature tensor κ_{ij} is experimentally determined from [98, 114]:

$$\kappa_{ij} = \frac{\partial \theta_i}{\partial x_j}, \tag{2.21}$$

where $\partial\theta_i$ represents the change of orientation angle, namely the lattice rotation about the i axis, and ∂x_j the displacement vector in j direction [100, 114].

With EBSD or TKD measurement, $\partial\theta_i$ and ∂x_j are accessible. The terms $\partial\theta_i$ and ∂x_j can be written as $\mathrm{d}\theta_i$ and $\mathrm{d}x_j$, as well.

According to Nye's original paper [114], the complete dislocation tensor α_{ij} can be replaced by curvature vectors:

$$\alpha_{ij} = \begin{pmatrix} -(\kappa_{22}+\kappa_{33}) & \kappa_{21} & \kappa_{31} \\ \kappa_{12} & -(\kappa_{11}+\kappa_{33}) & \kappa_{32} \\ \kappa_{13} & \kappa_{23} & -(\kappa_{11}+\kappa_{22}) \end{pmatrix}. \tag{2.22}$$

Combining the equation 2.22 and 2.20, the dislocation density ρ can be determined, as long as the α_{ij} and κ_{ij} are determined experimentally.

2.3.3 Reducing the 3D problem to 2D

The complete dislocation tensor α_{ij} is a 3×3 matrix, which means that a 3D EBSD measurement would be required to solve this tensor. A few publications reported the 3D EBSD implementation [14, 93–97, 112, 116], and applied the Nye tensor for post-processing of the data. However, 3D EBSD is fairly time-consuming since it requires slicing the material along the x_3 direction. Also, the resolution in the x_3 direction is limited as the material removal is usually achieved by mechanical polishing or focused ion beam (FIB) milling [14].

Therefore, it would be more efficient if the 3D problem were reduced to a 2D problem. For 2D, however, only five vectors in the 3×3 matrix of α_{ij} are accessible. All components containing κ_{i3} cannot be determined, since the term $\mathrm{d}x_3$ cannot be measured experimentally by EBSD or TKD analysis of an area. The only accessible components determined by a 2D measurement are [114]

$$\alpha_{12} = \kappa_{21} \tag{2.23a}$$

$$\alpha_{13} = \kappa_{31} \tag{2.23b}$$

$$\alpha_{21} = \kappa_{12} \tag{2.23c}$$

$$\alpha_{23} = \kappa_{32} \tag{2.23d}$$

$$\alpha_{33} = -(\kappa_{11} + \kappa_{22}). \tag{2.23e}$$

The 3D problem can be reduced to a 2D problem, as long as the plane strain condition is accomplished [100,101,117]. As stated by Rice [117], for both bcc and fcc materials, plane strain is associated with tensile cracks, having crack plane (010) and growing along [101], or crack plane (101) and direction of growth [010]. Equivalent loading condition is realized by indentation testing if a line load along the defined direction instead of a point load is applied [100, 101].

Applying plane strain loading condition within the indentation testing, therefore, reduces the experimental effort as well as the post-processing of the data. The similarities to the complex crack tip problem may contribute to our understanding of the stress and strain fields of the crack tip.

If plane strain deformation is achieved in a single crystal, points having the same coordinate (x_1, x_2) but different x_3 (see Figure 2.8), will have identical crystallographic orientation along the x_3 axis after deformation, as only planar rotation in the (x_1, x_2) plane occurs.

Therefore, the missing term κ_{33} (equation 2.22) is zero for a cross section, because $\mathrm{d}\theta_3$ about x_3 is zero. The two components in the α_{ij} tensor containing κ_{33} are determined, correspondingly:

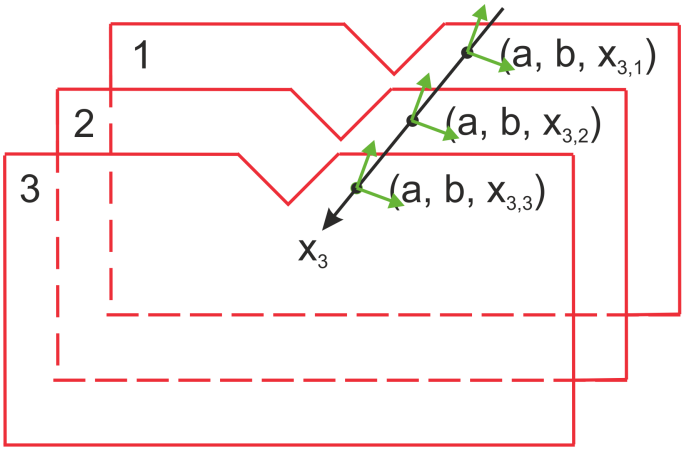

Figure 2.8
Schematic representation of points in the same position (x_1, x_2)=(a, b) on different slices (1, 2, 3...) along the x_3 axis. After the plane strain deformation, misorientation between these points are theoretically equal to zero.

$$\alpha_{11} = -\kappa_{22} \tag{2.24a}$$

$$\alpha_{22} = -\kappa_{11} \tag{2.24b}$$

According to the plane strain deformation, only in-plane rotation about the x_3 axis occurs. In other words, no deformation should occur about the x_1 and x_2 axes, so that $\mathrm{d}\theta_1$ and $\mathrm{d}\theta_2$ are zero. As a conclusion, only two components in the dislocation tensor α_{ij} in equation (2.23) are left non-zero, i.e. α_{13} and α_{23}. Experimentally, this theoretical result has indeed been observed and proven by Kysar et al. [100, 101]. As the dislocation tensor can be determined experimentally, Nye tensor together with Kröner tensor can be simplified and rewritten as:

$$\begin{pmatrix} 0 & 0 & \kappa_{31} \\ 0 & 0 & \kappa_{32} \\ 0 & 0 & 0 \end{pmatrix} = \rho b_i \otimes t_j, \tag{2.25}$$

with i,j=1,2,3. Thereby the GND density ρ associated with different individual slip systems can be determined. The total GND density ρ_{total} is easily calculated:

$$\rho_{total} = \sum_n \rho_{\mathrm{n}}. \tag{2.26}$$

Here n stands for the number of independent slip systems. It should be noted that the three components along the main diagonal in equation 2.25 represent the screw components. Equation 2.25, thus, shows that no screw dislocations are generated in the cross section under plane strain deformation.

3 Objectives of this work

Regardless of the excellent high-temperature performance of tungsten and tungsten-based materials, their application has been restricted due to the brittleness at room temperature. The mechanical reliability of tungsten-based alloys at room temperature can be problematic, which complicates the process to machine technical components.

The mechanical properties of a material, such as strength, hardness, and ductility, are highly dependent on its microstructures.

The mechanical behavior and the deformation microstructures of single-crystalline tungsten were studied using nanoindentation. Different nanoindentation methods were employed to obtain a comprehensive understanding of the dislocation mechanisms. The characterization of microstructures, i.e. dislocation structure and dislocation density, was performed using transmission Kikuchi diffraction (TKD) in a scanning electron microscope (SEM). The mechanical properties and the microstructures determined by different methods of nanoindentation and TKD were analyzed in the same framework. Therefore, the dislocation mechanisms as well as the influence of dislocations on the strength of single-crystalline tungsten were revealed at the nanometer and micrometer scale.

4 Experimental methods

In this work single-crystalline tungsten was studied using nanoindentation. The details of the sample preparation, the design of the nanoindentation experiments, and the characterization methods used, are described in this chapter.

4.1 Sample preparation

The tungsten sample studied in this work, was prepared from a tungsten bicrystal provided by Institute of Solid State Physics in Russia [16]. It was produced by hot-rolling two single crystals under vacuum and subsequent recrystallization [118]. A diamond wire saw was then used to cut the cylinder sample into smaller pieces with a thickness of approximately 2 mm.

As suggested by Rochlus et al. [119], the 2 mm thick tungsten sample was molded in EpoFix (Struers GmbH, Willich, Germany) with extra hardness regulator (Aequidur Typ H, SCAN-DIA GmbH & Co. KG, Hagen, Germany). To achieve a flat and horizontal surface, the sample was ground (Saphir 520, ATM Qness GmbH, Mammelzen, Germany) by SiC-paper from 300 to 1200 grit size, then mechanically polished (Saphir 520, ATM Qness GmbH, Mammelzen, Germany) with diamond suspension down to 1 µm grain size, followed by OP-A (acidic alumina) of 0.06 µm grain size. Finally, to reduce the work hardening effect due to the mechanical polishing process, the sample was electro-chemically polished (LectroPol, Struers GmbH, Willich, Germany) using 2 wt% NaOH solution. The individual steps of the sample surface preparation polishing process are summarized in Table B.1 in the Appendix.

After polishing, the sample was analyzed using the 3D laser scanning confocal microscope VK-9710K (Keyence Corporation, Osaka, Japan). The surface roughness (R_a) after the electrolytic polishing was reduced to less than 0.009 µm (determined by area measurement, measured area $\sim$5 µm^2). The flatness of the surface was checked by measuring the tilt angle in two orthogonal directions, i.e. longitudinal and transversal. The tilt angles are listed in Table 4.1. Figure 4.1 shows an EBSD mapping at the grain boundary of the bi-crystal. The measurement was conducted using an FEI DualBeam scanning electron microscope (Nova 200 NanoLab, FEI Company, now Thermo Fischer Scientific Inc., Massachusetts, U.S.) equipped with an HKL EBSD detector. The sample was tilted to 70° with a proper working distance of 10 mm to the electron beam. The SEM was operated at acceleration voltage and beam current of 20 kV and 9.5 nA, respectively. The beam was scanned over the sample surface with a step size of 4 µm. The crystal orientations perpendicular to the surface were (001) and (112), as confirmed by EBSD.

Table 4.1
Tilt angles in two orthogonal directions of the polished tungsten bi-crystal sample determined by 3D laser scanning confocal microscope.

tilt angle longitudinal (°)	**tilt angle transversal** (°)
0.305 ± 0.021	0.035 ± 0.007

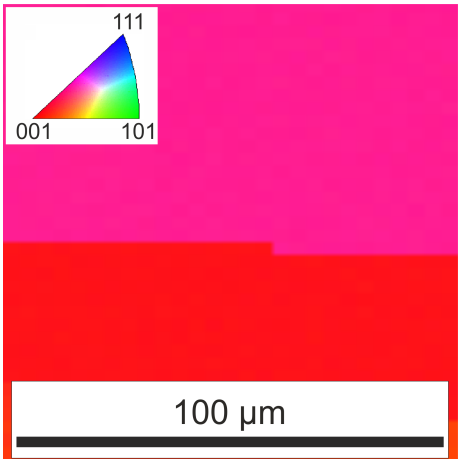

Figure 4.1
EBSD map at the grain boundary of the bi-crystalline tungsten sample: the out-of-plane orientations were confirmed as (001) and (112) as regarded in [16].

4.2 Nanoindentation testing

The mechanical behavior of single-crystalline tungsten was tested on different length scales ranging from nanometers to several micrometers. Young's modulus, hardness and pop-in loads were determined by nanoindentation using different indentation strain and loading rates. Furthermore, the activation volume was calculated to characterize the dislocation mechanisms.

A typical nanoindentation process (Figure 4.2) consists of a loading and unloading process, interrupted by two constant load segments performed at the maximum load to allow for relaxation of material and at 90% of the maximum load to measure the thermal drift rate during each measurement, respectively. For a dislocation-free surface, the typical indentation curve consists of two distinct portions, reflecting elastic deformation and elastic-plastic deformation, respectively. The transition between the two regimes is characterized by a jump in the load or depth signal depending on the control mode of nanoindenter setup used [120, 121]. This so-called pop-in effect [34] is schematically shown in Figure 4.2 for a defect-free surface indented using a load-controlled nanoindenter.

In this work, the nanoindentation tests were performed using a Nano Indenter G200 (Agilent/Keysight Technologies, Inc. California, USA, now KLA-Tencor Corporation, California, USA) with a diamond Berkovich tip, which is a three-sided pyramid (Figure 4.3). To study the deformation behaviors of the different length scale, the XP load (with a nominal maximum load of 500 mN) and the Dynamic Contact Module (DCM II, with a nominal maximum load of 30 mN) [122] were used. In addition to determining the unloading stiffness following the Oliver-Pharr method [7], the contact stiffness was also determined dynamically during loading using the Continuous Stiffness Measurement (CSM) option [123]. In the sections below, the analysis methods employed will be described.

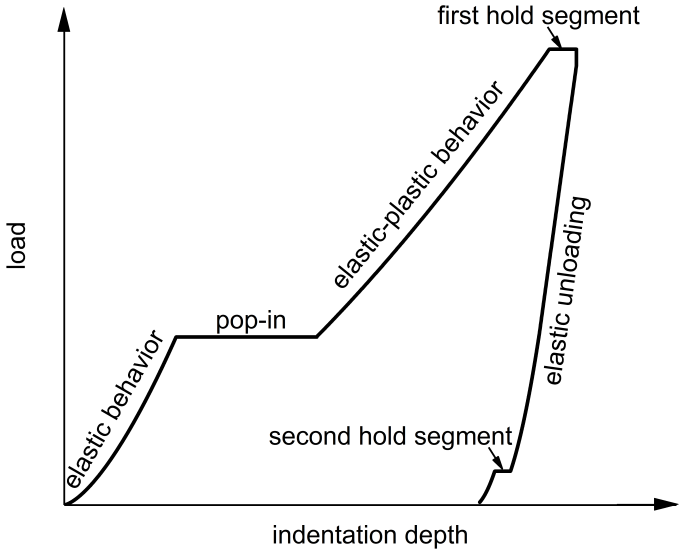

Figure 4.2
Schematic of a nanoindentation load-displacement curve reflecting the behavior of a dislocation-free material surface. Elastic and elastic-plastic regimes can be clearly distinguished. The pop-in is typical of a load controlled nanoindenter and is related to the nucleation of dislocations [28].

4.2.1 Determination of Young's modulus and hardness

Conventionally, indentation hardness is defined by the following equation:

$$H = \frac{P_{\max}}{A} \tag{4.1}$$

with $P_{\max}$ as the maximum load, and A the projected contact area. On the millimeter to micrometer scales, A can be determined by measuring the area of the imprint by optical microscopy [124]. However, reduced to the nanometer scale, measuring the projected contact area of nanoindents becomes difficult since the imprint is rather small.

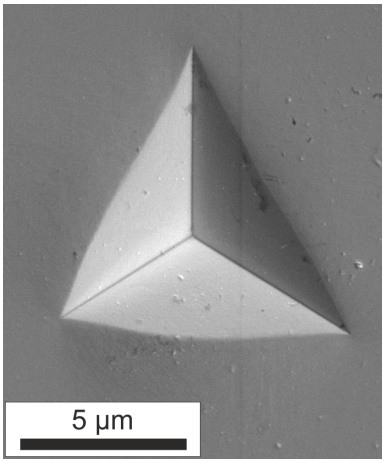

Figure 4.3
SEM micrograph of a showing typical residual imprint after Berkovich indentation. In this case, the indentation depth was 2000 nm.

In case of nanoindentation the Young's modulus and the hardness can be determined by estimating the stiffness from the upper part of unloading data in the load-displacement curve as described by Oliver and Pharr [7] (Figure 4.4).

With the unloading stiffness, S, the reduced modulus E_r is calculated by [7]:

$$E_r = \frac{\sqrt{\pi} S}{2\beta\sqrt{A}} \tag{4.2}$$

with the tip geometry factor β, which is 1.034 for a Berkovich tip. E_r is related to Young's modulus E and Poisson's ratio ν of the specimen and calculated from

$$\frac{1}{E_r} = \frac{1-\nu^2}{E} + \frac{1-\nu_i{}^2}{E_i} \tag{4.3}$$

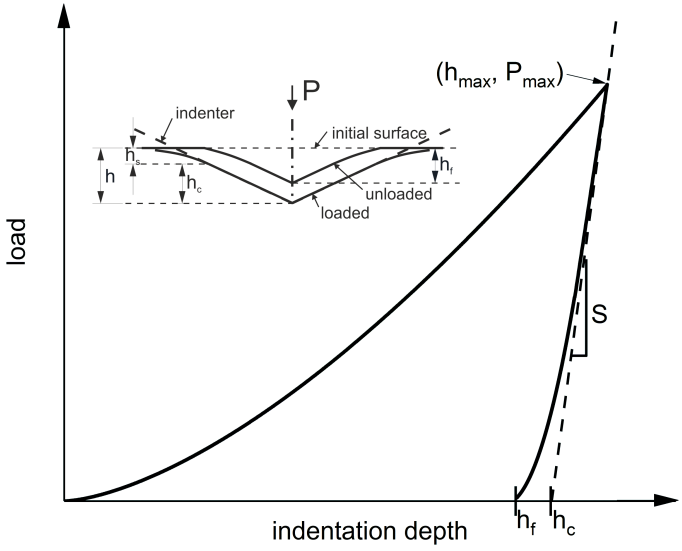

Figure 4.4
Schematic of determining stiffness and other characteristic parameters from load-displacement (*P*-*h*) curve. Maximum depth and load were revealed at the summit of the curve. Stiffness *S* has been estimated by measuring the slope of the upper experimental data. The x-intercept of the dashed line, which indicates elastic relation, is the estimated contact depth h_c. h_f stand for residual depth after indentation. A schematic illustration is shown in the inset, indicating the relevant parameters of the loading process and unloaded state of the nanoindentation [125]. During the nanoindentation, material sink-in was assumed [7, 125], characterized by a sink-in depth h_s.

with E_i=1141 GPa and ν_i=0.07 representing Young's modulus and Poisson's ratio of the indenter tip, respectively. For a Berkovich tip, the projected contact area A is determined as

$$A = 24.5{h_c}^2 \tag{4.4}$$

with h_c as the contact depth

$$h_c = h - \varepsilon\frac{P}{S} \tag{4.5}$$

that ε is a parameter and empirically defined as 0.75 for Berkovich tip [7]. However, in reality, the indenter is not perfectly shaped and the tip is rounded over the course of several experiments. The tip area can be expressed as [7,122]

$$A = m_0 {h_c}^2 + m_1 h_c + m_2 {h_c}^{\frac{1}{2}} + \cdots + m_n {h_c}^{\frac{1}{2^{(n-1)}}} \tag{4.6}$$

where m_0 to m_n are constants and can be fixed by tip calibration. Experimentally, the area function was determined by indentation testing of a fused silica standard, whose elastic properties are known, i.e. $E = 74.453$ GPa and $\nu = 0.188$. Using equation 4.2, the contact area is determined from the indentation data and the contact area function derived from a fit to the data using equation 4.6.

As an alternative to the unloading stiffness, the contact stiffness can be determined dynamically during "loading" [20, 123] by applying an oscillation additionally during the loading process. In this way, multiple unloading segments can be induced in one single measurement, and stiffness, Young's modulus, and hardness can be obtained continuously [20].

In this work, the indentation hardness of single-crystalline tungsten was determined by both the unloading stiffness measurement i.e. quasi-static method, and the dynamic measurement, i.e. CSM method.

For the unloading stiffness measurement, the first 10% of the unloading data was used and filled as described in [7]. A series of indents were conducted to different depths ranging from 100 to 450 nm in steps of 50 nm. For the dynamic measurement, constant strain rate (CSR) testing was applied while the indentation strain rates range from 0.005 s^{-1} to 0.5 s^{-1}. At each strain rate, more than 10 indents were made. The indentation strain rate $\dot{\varepsilon}$ for a self-similar tip geometry, such as the Berkovich tip, is defined as $\dot{P}/P$ [126] and is controlled by increasing the loading rate $\dot{P}$ with increasing load P. Therefore, the strain rate sensitivity m is defined as [41]

$$m = \frac{\partial \ln H}{\partial \ln \dot{\varepsilon}} = \frac{\ln H_2 - \ln H_1}{\ln \dot{\varepsilon}_2 - \ln \dot{\varepsilon}_1} \tag{4.7}$$

which can be determined by the slope of double-logarithm H-$\dot{\varepsilon}$ plot.

The activation volume V^* for single-crystalline tungsten of different orientations can be determined after the constant strain rate testing by this equation [30]

$$V^* = 3\sqrt{3}kT \left(\frac{\partial \ln \dot{\varepsilon}}{\partial H} \right) \tag{4.8}$$

with k and T as the Boltzmann constant and temperature, respectively.

4.2.2 Determination of maximum shear stress

The pop-in effect (Figure 4.2) indicates the transition from elastic to elastic-plastic deformation [34] for nanoindentation of a dislocation-free surface. In this regime, the tip shape changes from a spherical to a Berkovich geometry. Before the pop-in, the elastic load-displacement behavior can be described by the Hertzian contact equation [35]:

$$P = \frac{4}{3} E_\mathrm{r} \sqrt{R h^3}. \tag{4.9}$$

Here, R is the tip radius that can be estimated by fitting equation 4.9 to the experimental P-h data. The maximum shear stress τ_max [35, 36] under a spherical elastic contact can be estimated from the maximum pressure P_m according to

$$\tau_\mathrm{max} = 0.31 P_\mathrm{m} = 0.31 \left(\frac{6 E_\mathrm{r}^2}{\pi^3 R^2} P_\mathrm{pop-in} \right)^{\frac{1}{3}}. \tag{4.10}$$

The relevant force $P_\mathrm{pop-in}$ to calculate τ_max is the load at the onset of the displacement excursion (Figure 4.2). Note that the stress rate is proportional to the loading rate.

τ_{max} was determined for different constant indentation loading rates, referred to as constant loading rate (CLR) testing in the following chapter 5. Based on the τ_{max} measurements, the activation volume V_y^* related to the initiation of yield, i.e. dislocation nucleation activity, was estimated accordingly [24, 29, 34]:

$$f = 1 - \exp\left[-\frac{N_0 kT}{\dot{\tau} V_y^*} \cdot \exp\left(-\frac{\varepsilon}{kT}\right) \cdot \left(\frac{\tau V_y^*}{kT}\right)\right], \tag{4.11}$$

$$\ln\left[-\ln(1-f)\right] = \ln\frac{N_0 kT}{\dot{\tau} V_y^*} - \frac{\varepsilon}{kT} + \frac{\tau V_y^*}{kT}. \tag{4.12}$$

f is the cumulative distribution function (CDF), which describes the distribution of data points in terms of the τ value. Applying these equations to the CLR tests, τ and $\dot{\tau}$ are the maximum shear stress τ_{max}, and its stress rate, respectively. Here the term $N_0 \cdot \exp(-\varepsilon/kT)$ in equation 4.11 is the introduced parameter to describe the intrinsic dislocation nucleation probability [34], with N_0 the attempt frequency of nucleation event, and ε the activation energy.

V_y^* appears as an unknown parameter associating with variables $\dot{\tau}$ and τ, according to equation 4.11. Considering that the indents were conducted at constant temperature and loading rate ($\dot{\tau} \propto \dot{P}$), the two terms, $N_0 kT/\dot{\tau} V_y^*$, and $\exp(-\varepsilon/kT)$ are constant. Rewriting this equation 4.11 to 4.12, a linear behavior between $\ln\left[-\ln(1-f)\right]$ and τ_{max} is expected. Therefore, the slope of the linear relation is V_y^*/kT and V_y^* can be determined, since kT as the Boltzmann constant and temperature, are known.

Indents were made on two different crystal orientations using different loading rates, i.e. 0.05 mN/s, 0.1 mN/s, 0.2 mN/s and 0.5 mN/s. Around 100 indents per loading rate on (001) crystal were analyzed and τ_{max} determined. For (112) orientated sample, ca. 100 indents were conducted by the loading rate of 0.1 mN/s.

4.2.3 Summary of nanoindentation experiments

The sets of nanoindentation experiments conducted to study the indentation size effect single-crystalline tungsten and the plasticity mechanisms are summarized in Table 4.2.

Table 4.2
Summary of nanoindentation experiments using a Berkovich tip. The number of the CSM tests is shown in the table under the different experimental conditions. In addition, the number of the quasi-static nanoindentation is marked by an underline.

crystal orientation		**(001)**		**(112)**	
G200 module		**XP**	**DCM** II	**XP**	**DCM** II
	$\dot{P}/P$ **(s^{-1})**	**number of tests**			
CSRT	0.005	20*, 6†		6†	
	0.010	20*, 6†		6†	
	0.016	20*, 6†		6†	
	0.025	20*, 6†		6†	
	0.050	20*, 6†	6*, <u>48</u>*	20*, 6†	
	0.100	20*, 6†		6†	
	0.160	20*, 6†		6†	
	0.250	20*, 6†		6†	
	0.500	20*, 6†		6†	
	$\dot{P}$ **(mN/s)**	**number of tests**			
CLRT	0.05		100†		
	0.10		100†		100†
	0.20		100†		
	0.50		100†		

Data including constant strain rate tests (CSRT) and constant loading rate tests (CLRT) are shown in sections: * section 5.1; † section 5.2.

4.3 Dislocation structure analysis

To better understand the mechanical behavior of single-crystalline tungsten, the dislocation structure in the deformed region under the indents was analyzed. A wedge-shaped indenter tip was used and a line load applied along a defined crystallographic orientation, thereby introducing plane-strain deformation. A thin electron-transparent lamella of the deformed material was then prepared by focused ion beam (FIB) milling along specific crystallographic directions. Transmission Kikuchi diffraction (TKD) analysis was performed. The deformed structure such as dislocations and sub-grains beneath the wedge indent was quantitatively characterized.

4.3.1 Wedge indentation

Wedge-shaped indenter tips were used to indent the (001) single crystal. Depending on the size of the indents, the length of the wedge need to be 10 times larger than the indentation depth, to ensure the plane-strain condition. The maximum indentation depth was therefore 2 µm. Two different wedge indenter tips with tip angles of 90° and 60° and wedge length of 25 µm and 40 µm, respectively, were used. A typical residual indent of the wedge-shaped tip is shown in Figure 4.5.

The indents were conducted at three constant strain rates, i.e. 0.005 s^{-1}, 0.05 s^{-1} and 0.5 s^{-1}. The indentation depth was varied from 150 nm to 2000 nm. For all tests, the wedge indenter was aligned along a [110] direction on the (001) crystallographic plane (Figure 4.5). The experimental parameters are summarized in Table 4.3.

In addition to indents into bulk material, wedge indentation was conducted on a thin section of the material. The thin section was milled by FIB into the bulk single-crystalline tungsten sample. The thin section (Figure 4.6) had a length of 20 µm and a width of 5 µm. At least to a depth of 10 µm the material was

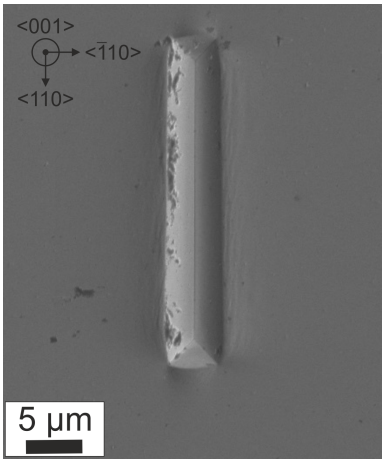

Figure 4.5
SEM micrograph of the residual indent produced by a wedge tip (tip angle 90°, wedge length 25 µm). The wedge indentation was aligned along a [110] direction on a (001) plane. The indentation depth was 2000 nm.

Table 4.3
Experimental details of the wedge indentation experiments on (001) single-crystalline tungsten (bulk material). The quasi-static nanoindentation experiments were conducted at three strain rates. Data marked by "√" will be presented in chapter 6.

wedge angle	$\dot{P}/P$ **(s^{-1})**	**indentation depth (nm)**			
		150	200	500	2000
90°	0.005		√		√
	0.05	√	√	√	√
	0.5		√		√
60°	0.05		√		√

removed from both sides of the "bridge". The wedge tip angle was 90°, aligned along the [110] direction and the indentation depth was set to 2000 nm at the indentation strain rate of 0.05 s^{-1}. SEM images before and after the wedge indentation of the thin section are shown in Figure 4.6.

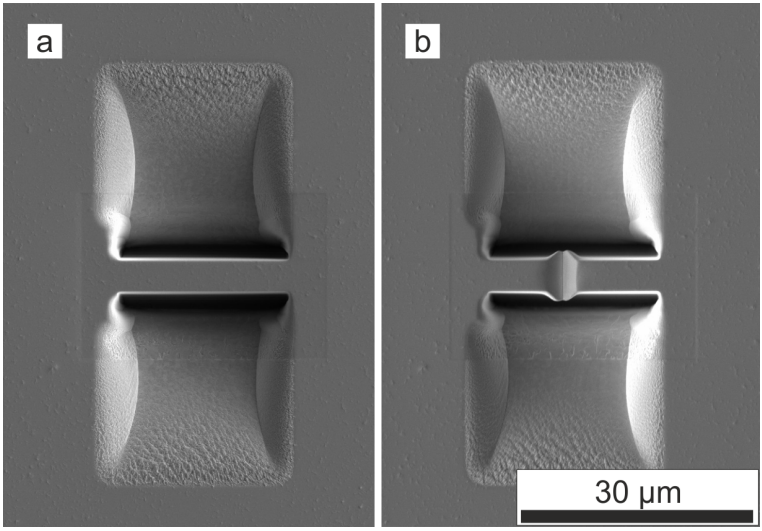

Figure 4.6
SEM micrographs of the thin section (a) before and (b) after wedge indentation. The "bridge" was prepared by FIB milling. To ensure the indenter tip could be aligned in the center of the bridge, trenches of 22 µm length were milled on both sides.

This specific geometry was selected, to facilitate a direct comparison with the numerical simulation by Tillmann Volz from the University of Applied Sciences in Karlsruhe [127].

4.3.2 Sample preparation for transmission Kikuchi diffraction

Transmission Kikuchi diffraction measurement was conducted on several cross sections through wedge indents in the bulk material (Table 4.3) and the thin section (Figure 4.6). The preparation of the TKD lamellae was accomplished using the Helios NanoLab 650 DualBeam microscope (FEI Company, now Thermo Fischer Scientific Inc., Massachusetts, U.S.) by FIB.

To protect the surface during the FIB milling, Pt was deposited over the region of interest using the electron beam operated at acceleration voltage of 2 kV followed by the Gallium ion (Ga^+) beam operated at 30 kV acceleration voltage. The beam current was varied according to the size of the area. Then, large trenches on both sides of the cross section were milled with the Ga^+ beam operated at acceleration voltage and beam current of 30 kV and 45 nA, respectively. The surface quality of the lamella was refined by applying the "cleaning cross section" step by step with reduced beam currents from 9.5 nA down to 0.77 nA. The thickness of the lamella was reduced approximately 1 µm. The lamella was then transferred using a micromanipulator (Omniprobe, Oxford Instruments GmbH, Wiesbaden, Germany) to a TEM copper grid for further preparation.

It was further thinned from both sides to the final thickness, of around 100 to 150 nm. The beam current was further reduced during the process from 0.77 nA to 0.83 pA. Finally, the thin lamella was polished by the ion beam operated at 2 kV and 44 pA, in order to reduce the damage caused by Ga ions from the previous steps of the preparation process. The process for FIB prepared TKD lamella is summarized in Figure 4.7.

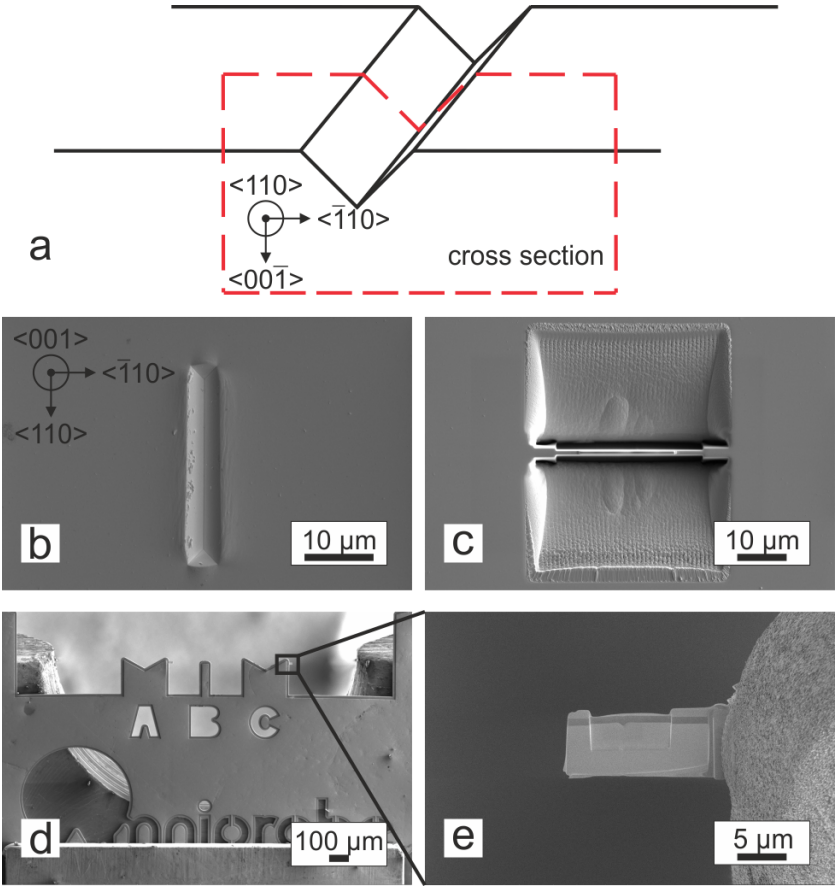

Figure 4.7
For TKD analysis, an electron-transparent lamella of a cross section through a wedge-indent was prepared using a FIB. (a) The wedge was aligned with specific crystallographic directions and lifted out from the mid-section of the indent. (b)-(e) show the main FIB preparation steps. After Pt deposition, a thin section (approximately 1 µm thickness) was prepared by FIB milling. The lamella was then transferred to a Cu grid. The region of interest beneath the indent was then further thinned to the final thickness of 100-150 nm.

4.3.3 Measuring crystallographic orientation by transmission Kikuchi diffraction

The TKD measurements were carried out using the AZtec EBSD system with AZtecHKL as software (Oxford Instruments GmbH, Wiesbaden, Germany) and the high definition EBSD detector e$^-$Flash^{HD} (QUANTAX EBSD, Bruker Nano GmbH, Berlin, Germany). The acceleration voltage and beam current of the electron beam were the same for all the measurements, i.e. 30 kV and 6.4 nA, respectively.

The fundamental principle of TKD is the same as of conventional EBSD. The focused electron beam strikes the surface of a specimen, and some backscattered electrons traveling along the crystallographic plane diffract. Their diffraction cones hit the phosphor screen, namely the detector, and generate the so-called Kikuchi pattern. By analyzing the width and angle of the Kikuchi bands, which indicate the distance and orientation of individual crystallographic planes, the crystallographic orientation of the specimen can be determined [90–92, 128].

In the case of EBSD, the electron beam hits directly at the bulk material and only the reflected diffraction can be captured by the detector. Therefore, the bulk specimen is usually tilted to 70° to enhance the reflected diffraction signal (Figure 4.8). Accordingly, the resolution of EBSD is limited due to the interaction volume of the electron beam and the material. While the EBSD signal comes from 10-20 nm beneath the material surface, the corresponding interaction volume encompasses a depth of approximately 100 nm [105] (Figure 4.8(a)).

TKD measurements require a thin electron-transparent lamella and the diffraction signal of the backscattered electrons are captured in transmission. Instead of tilting to 70°, the lamella is installed almost horizontally and the tilted angle should not be bigger than 20° (Figure 4.8). The incoming electron beam hits the sample almost perpendicularly and the electron interaction volume

is significantly reduced. The effective resolution of TKD can be improved to less than 20 nm, which benefits the accuracy of dislocation characterization [13, 105, 107, 108]. The characterize geometries of EBSD and TKD are illustrated in Figure 4.8.

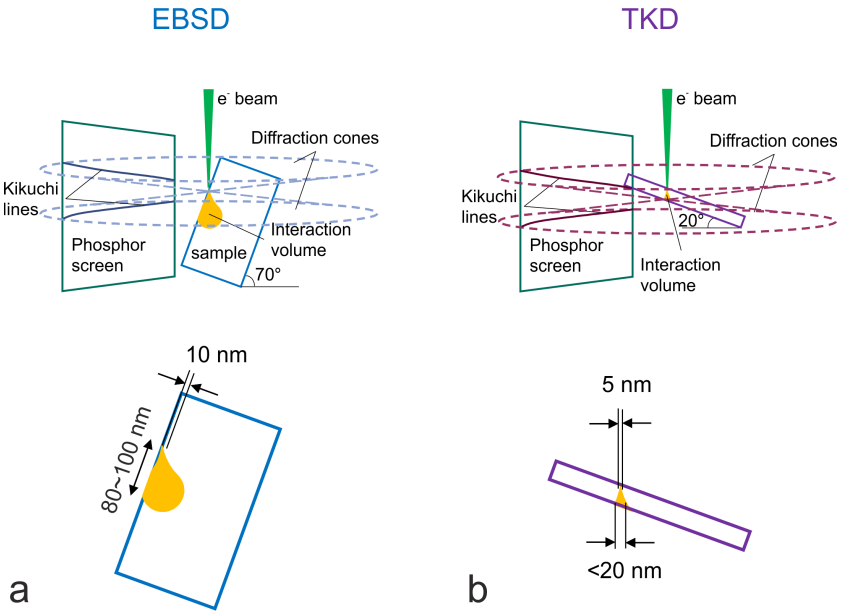

Figure 4.8
Based on the same fundamental principles,(a) EBSD and (b) TKD measurements require different geometrical arrangements. When the e^- beam hits the sample surface and generates a diffracted signal, diffraction cones are captured as Kikuchi patterns on the phosphor screen of the detector. The resolution of a measurement is influenced by the electron interaction volume and is significantly improved for TKD.

In this work,TKD measurements were conducted on cross sections of indents with a depth ranging from 150 nm to 2000 nm. The step size was kept between 7 nm for shallow indents to 17 nm for bigger indents. It was adjusted depending on the size of the deformed region and with respect to the measurement time. The influence of step size on the characterization of dislocation

density is discussed in chapter 6. The influence of two EBSD systems used is crosschecked and discussed in chapter 6.

4.3.4 Analysis of TKD data

The raw output of TKD measurement contains information about the position of the individual points (x, y) and the crystallographic orientation as the three Euler angles $(\varphi_1, \Phi, \varphi_2)$, according to the Bunge convention [129]. They describe the relative angles between the tungsten crystallographic system and the reference system, i.e. the sample system related to specimen installation. Further analysis was conducted using MATLAB and the open-source toolbox MTEX [130, 131]. The analysis process is summarized in Figure 4.9 as a flow chart.

First, the raw TKD data were pre-processed, i.e. the region of interest was cropped in order to reduce calculation time. The boundary of the indexed area must be defined to avoid artifacts, and therefore the unindexed indent regions need to be removed. The redefined analysis region after these two processes is indicated as purple area in Figure 4.9.

For further calculation, especially for the GND calculation, the data was smoothed, to account for unindexed individual points in the analysis region. The misorientation $\mathrm{d}\theta$, depends on the indexed neighboring points, and errors due to unindexed points will therefore increase. In the smoothing process, the unindexed points are corrected using a spline function. The estimated value is fitted with the data from neighboring points, as the deformation is continuous and the rotation is small between two neighboring points.

The GND density was determined by kernel average misorientation (KAM) and the Kröner tensor [114, 115], the crystallographic orientation mapping, lattice rotation, and curvature distribution were calculated. The results are presented and discussed in chapter 6 and 7.

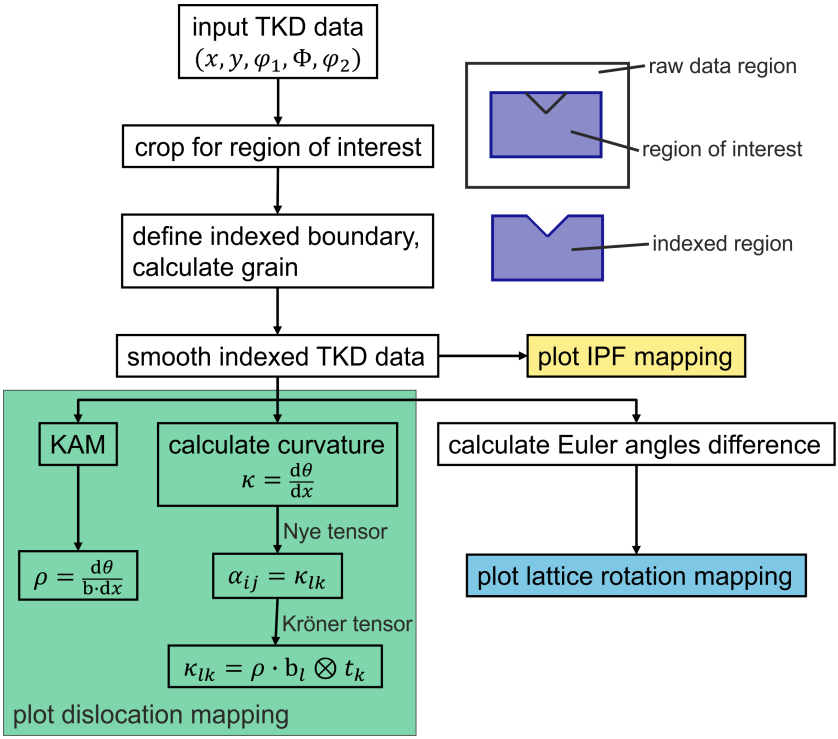

Figure 4.9
Flow chart describes the general analysis process of TKD data using MATLAB and MTEX-toolbox [130, 131]. The TKD data would be pre-processed for further analysis. By using this analysis process, results such as inversed pole figures, lattice rotation maps, and dislocation distributions are able to be plotted.

5 Nanoindentation results

In this chapter the results obtained from Berkovich nanoindentation are presented. First, the ISE determined following different experimental approaches (see section 4.2.3) is described in section 5.1.

The following section 5.2 then reports the analysis of the activation volume from the pop-in behavior (see section 4.2.2) and the strain rate dependent hardness.

5.1 Bi-linear ISE of single-crystalline tungsten

Nanoindentation testing has been undertaken using different nanoindentation methods and setups (see section 4.2.3). Consistently, all experiments showed the same trend of the results of tungsten single crystals, namely a bi-linear ISE (see Figure 2.4 in section 2.2) of single-crystalline tungsten. First, the depth-dependent behavior is shown in details for an indentation strain rate $\dot{P}/P$=0.05 s^{-1} for indentation into a (001) tungsten single crystal. The behavior of a (112) out-of-plane orientated tungsten single crystal is similar. The data can be found in chapter 7 (Figure 7.3).

5.1.1 Influence of different indentation methods

As described in section 4.2.3, both dynamic and quasi-static nanoindentation experiments using a Berkovich tip were performed on the tungsten (001) and (112) single crystals. Typical load-displacement curves to different depths of tungsten (001) single crystal are shown in Figure 5.1.

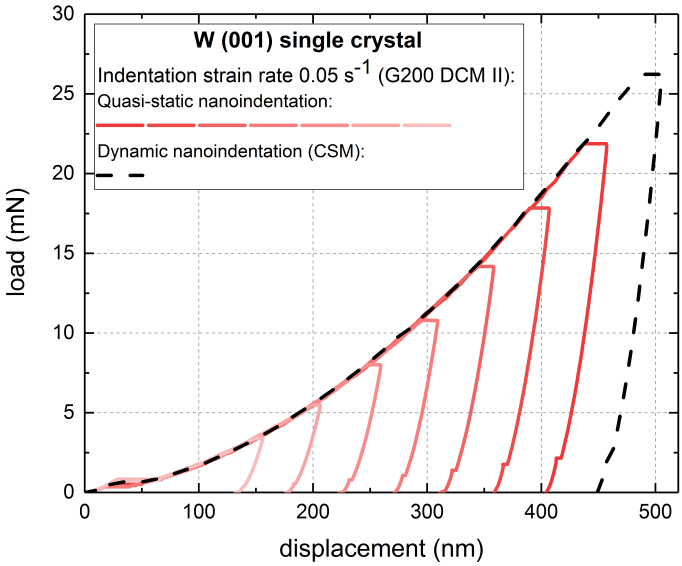

Figure 5.1
Typical load-displacement curves of tungsten (001) single crystal using the G200 DCM II. Indentation strain rate for both quasi-static and dynamic nanoindentation experiments was 0.05 s^{-1}. The quasi-static indents were conducted to different depths ranging from 150 nm to 450 nm (red solid lines). The dynamic (CSM) indents were made to a depth of 500 nm (black dashed line).

Good agreement between the curves obtained by different methods can be seen. In addition good agreement of elastic modulus values was observed, as shown in the Appendix A.1.

The hardness obtained from the different sets of experiments are plotted over indentation depth in Figure 5.2(a). For comparison indentation data from the literature [41, 63] has been added (gray lines and squares in Figure 5.2). The hardness data determined by different indentation methods show good agreement with each other (green and blue areas in Figure 5.2), and exhibit strong ISE following an identical tendency like the literature data.

Taking the Nix-Gao model [9] into account, the hardness data are plotted in the form of H^2 over $1/h$ in Figure 5.2(b). Beside the indentation data, the predicted H^2-$1/h$ behavior according to equation 2.7 is shown as the red solid line. Its intercept, as shown in Figure 5.2(b), equals to H_0^2, where H_0 is the depth-independent hardness [9]. As indicated by the red line, the Nix-Gao model could only describe the indentation behavior of single crystalline tungsten in the depth regime of 500 nm to 2000 nm. Noticeable bi-linear behavior of H^2-$1/h$ curves was observed, which is independent of the nanoindentation methods and modules (Figure 5.2(b)). A transition of the bi-linear ISE occurs at the depth around 300 nm, for both the indentation data of this work and from the literature [41, 63]. The similar bi-linear ISE was observed on different materials [41, 57–63], and has been shown in Figure 2.4 in chapter 2.

Generally, the bi-linear ISE of single-crystalline tungsten cannot be affected by using different testing modules, i.e. G200 XP or DCM II (see the overlap of blue and green bands in Figure 5.2). Comparing to the hardness values determined by the dynamic nanoindentation, quasi-statically measured hardness often shows lower values at the same indentation depth (gray and green symbols in Figure 5.2). The reason of the lower hardness values has been discussed in previous literature [132], and turns out to be a lower effective strain rate due to the quasi-static measurement. The tendency of the two data sets, though, are identical.

According to the experimental results (Figure 5.2(b)), the bi-linear ISE of single-crystalline tungsten is independent of the testing method and setup used. The possibility of non-linear ISE caused by the limitation of CSM technique

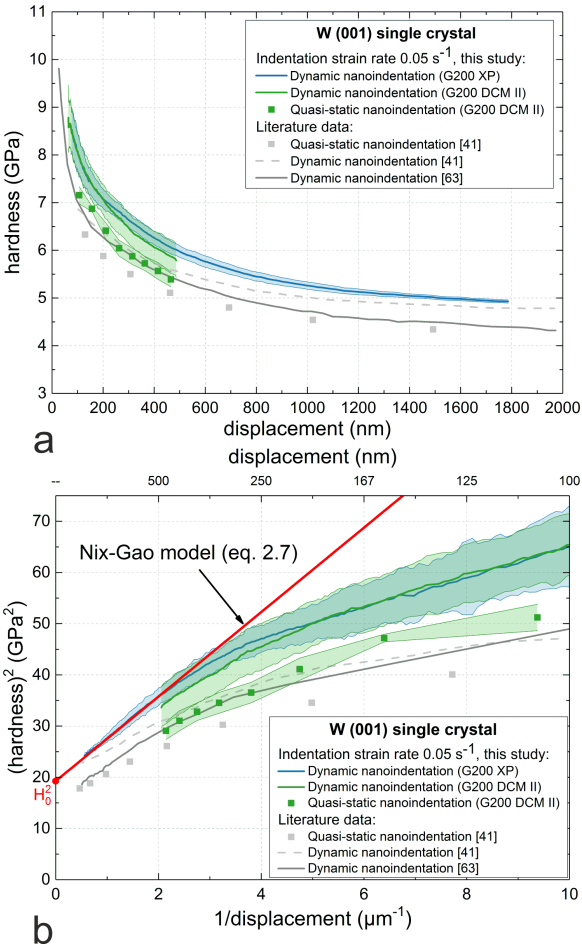

Figure 5.2
Hardness-displacement plot in (a) and H^2-$1/h$ plot in (b). The blue and green lines show the averaged hardness value of the dynamic measurements using the G200 XP and DCM II. The red line predicts the indentation behavior of CSM data with H_0 determined by the intercept, according to the Nix-Gao model [9]. Results from quasi-static measurements are denoted by the green squares. The standard deviations are shown as the light blue and green shaded areas. For comparison, Berkovich hardness data from the literature [41, 63] have been added and are shown as grey lines and symbols.

[70,71] is, therefore, not appropriate for the case of single-crystalline tungsten. As the transition of bi-linear behavior occurs at the depth of 300 nm, this particular bi-linear ISE is differed from those effects, which are related to the tip blunting and the rough surface [10, 63]. The bi-linear ISE of single-crystalline tungsten is rather a material behavior than an artifact caused by the measurement technique. In chapter 7, a quantitative description of the bi-linear ISE observed in the tungsten single crystal is proposed.

5.1.2 Strain rate dependency of the ISE

A series of CSR experiments was applied at nine different strain rates ranging from 0.005 s^{-1} to 0.5 s^{-1}, as described in section 4.2.3. For each strain rate, 20 indents were performed on the (001) tungsten single crystal.

Representative load-displacement curves are shown in Figure 5.3(a). The effective indentation strain rate of each test over depth is shown in Figure 5.3(b) together with the measured Young's modulus indicated by the blue lines. The average value of Young's modulus at different strain rates was calculated and indicated by the orange symbols. In Figure 5.3(c), the complete overview of the mean values of Young's modulus over depth at nine different strain rates are shown with standard deviations, respectively.

With increasing strain rate, the load at the maximum depth increases (Figure 5.3(a)). The nine indentation strain rates were designed equally spaced, and implemented effectively in the CSR tests (Figure 5.3(b)). In general, the strain rates reach the targeted values after a certain depth. Relatively, the higher strain rates stabilize at smaller depth. From the depth of 250 nm, all the nine strain rates exhibit constant values. For strain rates ranging from 0.005 s^{-1} to 0.16 s^{-1}, the dynamic measurement allowed a reliable analysis of Young's modulus, while at the two highest strain rates 0.25 s^{-1}, and 0.5 s^{-1} , the dynamic stiffness could not be determined well. With strain rate increasing, the standard deviation of Young's modulus also increases (Figure 5.3(c)). The

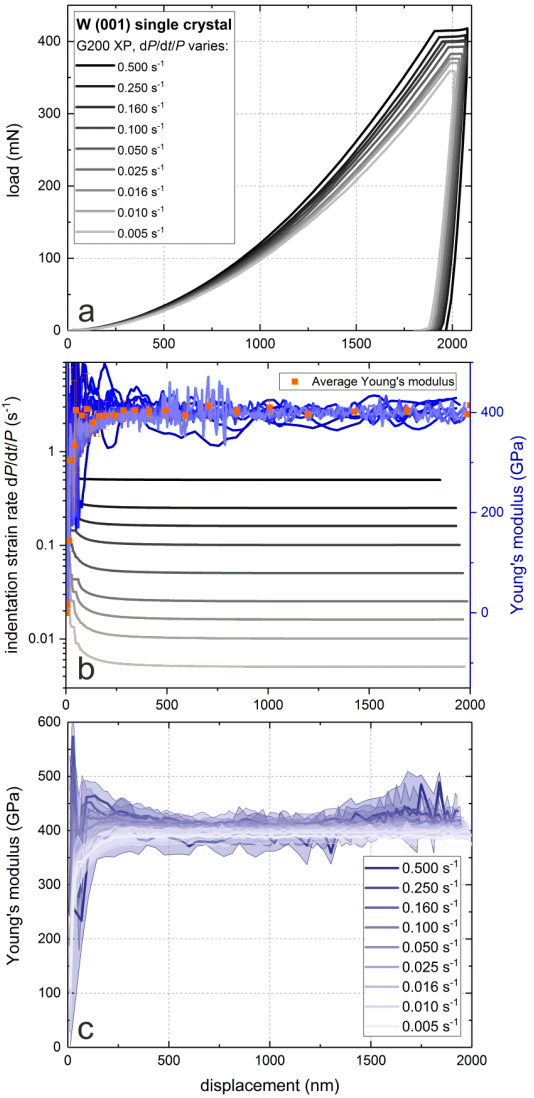

Figure 5.3

(a) Load-displacement curves of CSR test at nine different indentation strain rates; (b) Indentation strain rate and Young's modulus over indentation depth, The average value of Young's modulus is shown as the orange symbols with standard deviation; (c) Average values of Young's modulus for nine CSR tests with standard deviation showing as shaded areas. Color density of lines decreases with decreasing strain rate.

Young's modulus values obtained at the highest strain rates exhibit a significant variation as shown by the two darkest blue lines in Figure 5.3(b). Nevertheless, the variation is reducing as the indentation depth increases. From the depth of 200 nm, the average values of Young's modulus in Figure 5.3(b) reveal significantly small standard deviation. The average Young's modulus value in Figure 5.3(b), as well as the values of all the CSR tests in Figure 5.3(c) show perfect agreement with the literature data (410 GPa) [133].

Similar to Figure 5.2, hardness determined by nine different strain rates has been plotted in the form of $H - h$ and $H^2 - 1/h$, in Figure 5.4(a) and (b), respectively.

Generally, the hardness increases with increasing strain rate. Significant ISE is observed in all the CSR experiment series. By the maximum depth of 2000 nm, the hardness values of nine strain rates have not yet reached the constant values. The depth-independent hardness values, i.e. H_0, extrapolated by using Nix-Gao model [9] (see Figure 5.2(b)) are ranging from 3.98 GPa to 5.10 GPa, while the indentation strain rate ranges from 0.005 s^{-1} to 0.5 s^{-1}. The H_0 values are comparable to the literature values (4.2 GPa [36] and 4.3 GPa [63] measured at 0.05 s^{-1}), and can be found in Table B.2 in Appendix. Bi-linear ISE is not only observed by 0.05 s^{-1} as it was shown in Figure 5.2(b) but repeatedly appears in experiments at other strain rates. In all measurement series, the transition between the two regimes happens at a similar depth around 300 nm (see green dashed line in Figure 5.4(b)), but shifted towards lower depths with increasing strain rate. The higher the strain rate, the less pronounced the bi-linear effect. Another remarkable phenomenon in this figure is that the hardness curves at different strain rates are not parallel. The difference of the hardness at two strain rates in the larger depth regime, for instance at 2000 nm, is smaller than the hardness difference in the lower depth regime, for example at 200 nm. Therefore, in the two depth regimes reflected in the bi-linear ISE, the response of the dislocation structure to a strain rate change might be different.

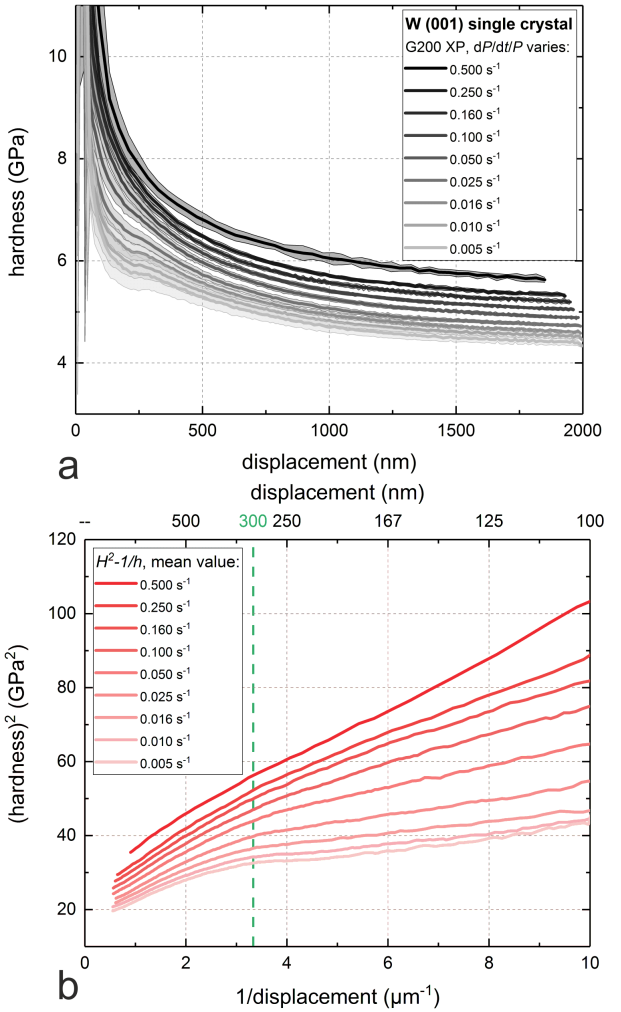

Figure 5.4
Hardness-displacement curves at nine strain rates in (a) and $H^2 - 1/h$ plot in (b). The mean values are shown in solid lines and the standard deviations of hardness values in gray shaded areas. Color density of lines decreases with reduced strain rate.

5.2 Activation volume for plasticity evolution

While the nanoindentation depth ranging from several nanometers to micrometers, the elastic deformation of single-crystalline tungsten sample develops to elastic-plastic.

The activation volume reflecting the dislocation nucleation and motion were determined by CLR tests and CSR tests, respectively. The results contain two single-crystalline grains that are introduced in the following section.

5.2.1 Activation volume for dislocation nucleation

CLR tests at various loading rates were performed on (001) and (112) single crystals. In Figure 5.5, typical load-displacement behavior at 0.1 mN/s of two single crystals are plotted to compare together. Only one pop-in was observed in tests of each orientation. It is obvious that the elastic property of two single crystals are identical, which can be indicated by the overlapping loading curves before the pop-in effect. After the pop-in, the loading curves indicating elastic-plastic deformation behave differently. In the elastic regime before the pop-in, the load-displacement behavior can be described by the Hertzian contact equation 4.9, while the proper tip radius R here was estimated as 190 nm. At the on-set point of the pop-in, the corresponding load $P_{\mathrm{pop-in}}$ was recorded and used as input for equation 4.10, which yielded $\tau_{\max}$.

Maximum shear stress $\tau_{\max}$ of all CLR tests are summarized in Figure 5.6 as cumulative probability distribution. The individual values $\tau_{\max}$ were arranged according to their magnitude and assigned the index j. While the total number of tests is known as n, the cumulative distribution function (CDF) f for each point can be determined by $f = j/(n+1)$ [134]. Plotting the cumulative probability f over $\tau_{\max}$, the median values of $\tau_{\max}$ (see the black dashed line

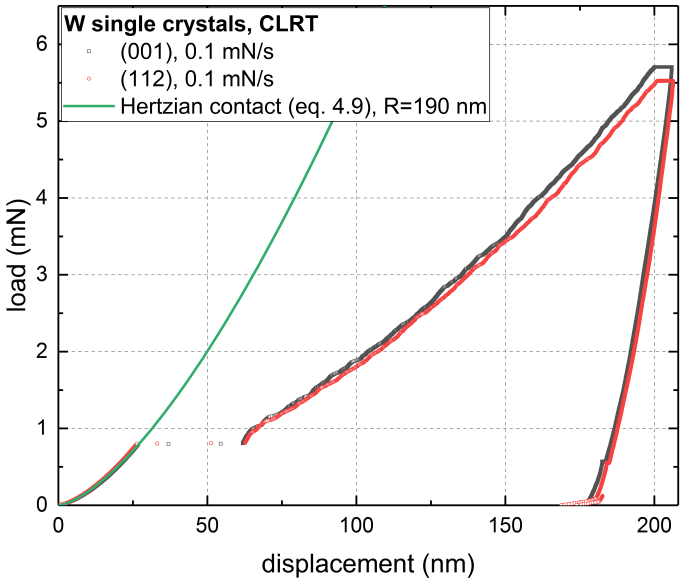

Figure 5.5
Typical load-displacement curves of (001) and (112) single crystals indented at constant loading rate of 0.1 mN/s.

in Figure 5.6) and the deviations, i.e. the scattering of data points, of each data set can be intuitively presented.

According to the experimental results shown in Figure 5.6, most of the data points are found in the range from 22 GPa to 23.5 GPa. Median values of each CDF curve are located at ∼23 GPa with a fairly small deviation of ±0.25 GPa, which is very close to the theoretical shear strength $\mu/2\pi$ (24.2 GPa), with μ being the shear modulus. In the loading rate range from 0.05 mN/s to 0.5 mN/s, the CDF distributions of τ_{max} at individual loading rate reveal similar median value and scattering shape. Comparing the median values at four loading rates on (001) single crystal, no significant loading rate dependence of τ_{max} was observed. Moreover, τ_{max} values measured on (112) single crystal do not

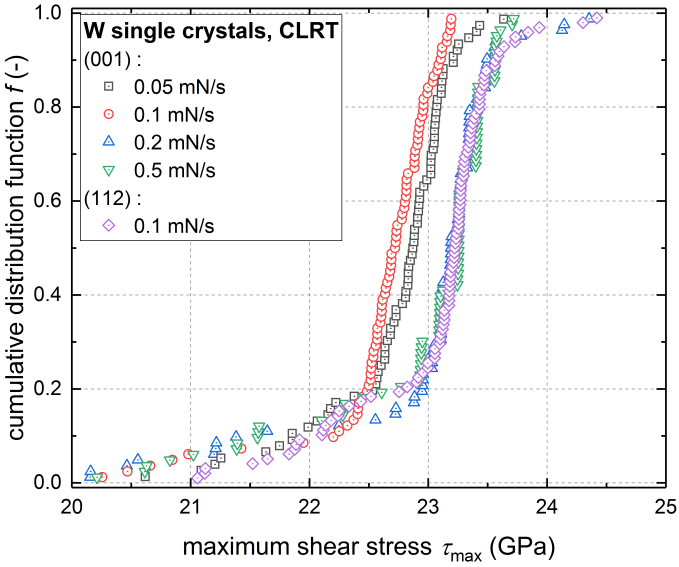

Figure 5.6
Cumulative probability distribution of τ_{max} for two different crystal orientations measured by CLR tests at different loading rates.

give a pronounced difference compared to (001). The difference between both measurements at the same loading rate of 0.1 mN/s is only 2%.

There are several data points in the lower τ_{max} region (20-22 GPa), which are believed to be caused by the variation of the local surface quality, for example, shallow etch pits resulting from the electro-polishing. For the further analysis of the activation volume V_y^* (see equation 4.11 and 4.12 in chapter 4), these data points were excluded.

The main part of each data set approximately exhibits linear behavior as can be seen in Figure 5.7. Therefore, the individual slopes were estimated by a linear fit, as shown in Figure 5.7 by the solid lines. Activation volume under every testing condition was calculated and then normalized by b^3. The number of

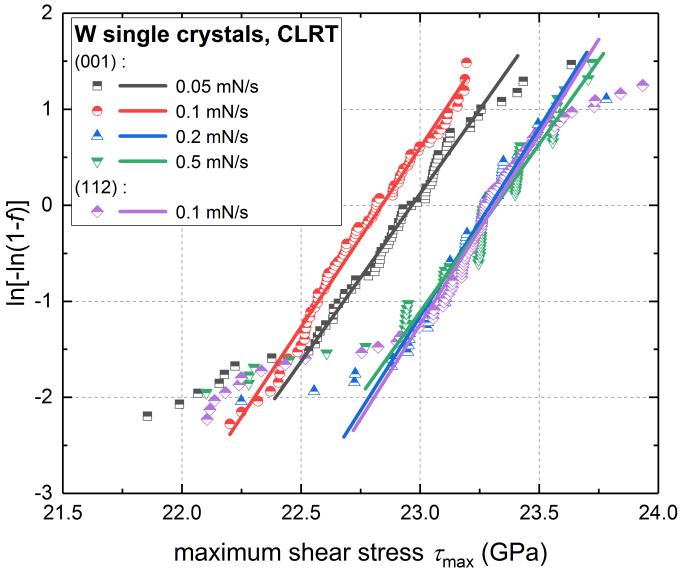

Figure 5.7
Estimation of V_y^* for five data sets of different constant loading rates and crystalline orientations. Most of the data points (shown as symbols) reveal a linear behavior of $\ln[-\ln(1-f)]$ to τ_{max}. According to equation 4.12, a linear fit (solid lines) was applied on each data set and the slope was determined.

atoms that would be involved in this activity is also calculated. The results are summarized in Table 5.1.

The experimentally determined activation volumes for dislocation nucleation on tungsten single crystals are in a range from 0.7 b^3 to 0.8 b^3. This magnitude of $\sim$1 b^3 is quite comparable to the literature [30, 135] and typical of bcc metals. The number of atoms involved in the nucleation process was estimated as 1, suggesting that in the tungsten single crystals, dislocation nucleation is more likely related to heterogeneous than homogeneous loop nucleation, because the activation volume for the latter process is much larger and would involve more atoms [24, 135]. As indicated in Figure 5.6 for τ_{max}, also V_y^*, does not exhibit

Table 5.1
Activation volume of dislocation nucleation and the number of atoms determined by different loading rates and crystallographic orientations.

crystal orientation	**(001)**				**(112)**
loading rate $\dot{P}$ (mN/s)	**0.05**	**0.1**	**0.2**	**0.5**	**0.1**
V_y^* **(Å^3)**	14.39	15.37	16.15	14.34	16.23
V_y^* **(b^3)**	0.70	0.75	0.79	0.70	0.79
number of atoms	1	1	1	1	1

a loading rate dependence at room temperature. The estimated V_y^* for (112) single crystal reveals a similar value to (001), as shown in Table 5.1. The comparable values, i.e. τ_{max} (Figure 5.6 and Figure 5.7) and V_y^*, of both crystals indicate that the crystal orientation could hardly influence the dislocation nucleation of single crystalline tungsten at room temperature. In chapter 7, the nucleation mechanism is discussed in detail.

5.2.2 Activation volume for dislocation motion

Single crystalline tungsten exhibits remarkable strain rate sensitivity, as shown in Figure 5.4. For increasing strain rate, the hardness also increases. Experimentally, strain rate sensitivity m and activation volume V^* were determined by CSR tests at nine indentation strain rates. Specifically, m (see equation 4.7 in 4.2.1) was estimated by the slope of hardness over the strain rate in the double logarithmic plot, while V^* was calculated after equation 4.8. Figure 5.8 shows the m and V^* determined by the depth-independent hardness H_0 of two crystal orientations. As shown in Figure 5.2(b), H_0 values at nine strain rates were extrapolated according to the Nix-Gao model [9] in equation 2.7 using data in the range from 500 nm to 2000 nm, to avoid the transition of two regimes.

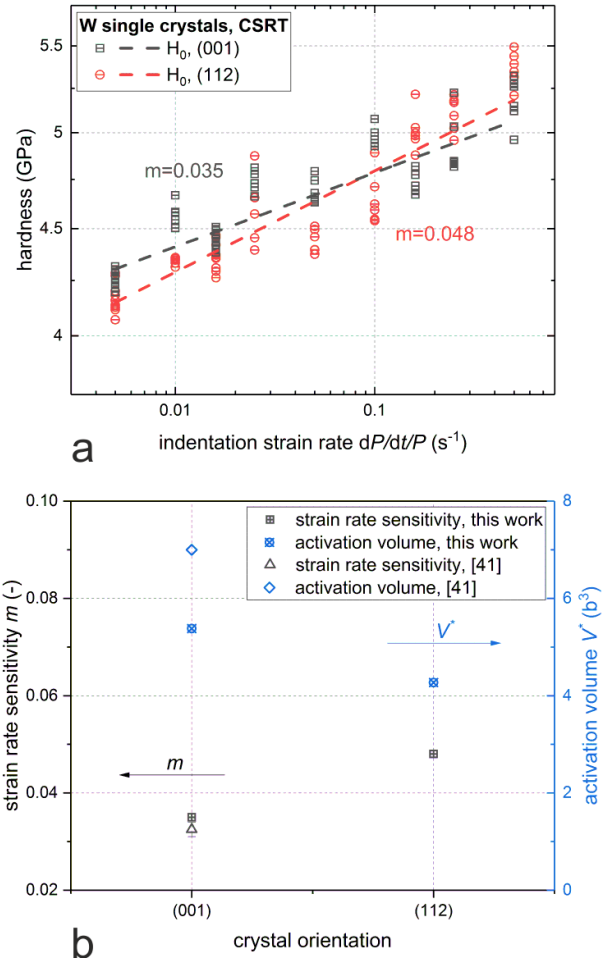

Figure 5.8
(a) Determination of strain rate sensitivity m using linear fit shown as the dashed lines; (b) m and activation volume of dislocation motion V^* for two single crystals. For comparison, values for m and V^* determined from strain rate jump tests published in [41] were added.

Basically, the H_0 values determined of both orientations increase linearly with the strain rate in the double log plot. The slope of the linear fit, i.e. the

strain rate sensitivity m of two orientations was determined as 0.035 for the (001) single crystal and slightly higher (0.048) for the (112) crystal orientation. Compared to the literature results [41] of strain rate jump tests shown in Figure 5.8(b), the values for the (001) single crystal are in very close range, where m and V^* were determined as 0.031, and 7 b^3 for the (001) tungsten single crystal at the depth of 2000 nm [41], respectively. Compared to the activation volume for dislocation nucleation V_y^* shown in Table 5.1, V^* is one order of magnitude larger, that (001) crystal has 5.38 b^3, and (112) 4.27 b^3. Thus, in tungsten single crystals, dislocations first nucleate heterogeneously benefiting from pre-existing defects in the lattice, such as vacancies or impurities, then the dislocations propagate and move towards the defect-free body by the kink-pair mechanism. During this process, the activation volume increases, as the size of the characteristic dislocation structures increases.

The evolution of plasticity was analyzed further by determining the activation volume dynamically during the indentation process. To avoid the pop-ins, V^* of both orientations were determined continuously at every 100 nm depth in the range from 200 nm to 2000 nm. The results are presented in Figure 5.9.

In general, the activation volumes of single crystalline tungsten calculated in this work match well with the literature data by other approaches [22, 41]. Moreover, there are several remarkable points worth highlighting in this figure. First of all, for each orientation, the activation volume increases with increasing indentation depth. A similar phenomenon was also seen in the pillar compression tests of (001) orientated tungsten [22]. At depths > 1000 nm, V^* of both crystal orientations reach a plateau, which corresponds to the value determined from depth-independent hardness H_0. This trend shows, on one hand, that the measurement of activation volume at different depths is reliable. On the other hand, it reflects the evolution of the dislocation structures in tungsten single crystals. Furthermore, the plateau of V^* for (001) and (112) orientations occur at different values of V^*. The predominant kink-pair mechanism might, thus, vary in different orientations as V^* is associated directly with the

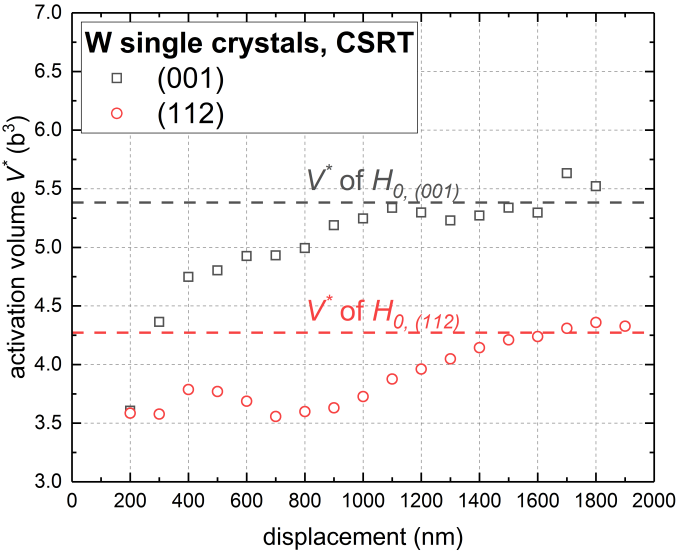

Figure 5.9
Activation volume of dislocation motion over indentation depth. Each value of V^* was determined from hardness values at different depths of CSR tests, at nine strain rates. As a reference, values of V^* determined by the H_0 values for two orientations are shown as the black and red dashed lines, respectively.

kink-pair structure. Also, at the smaller depth, both (001) and (112) have a minimum at 3.5 b^3. For (001), at 200 nm depth, V^* starts at the minimum value, then rises monotonously with the depth until saturation. For (112), V^* is generally smaller than for (001), but not smaller than 3.5 b^3, which suggests the existence of a lower limit for activation volume of dislocation motion in tungsten single crystals.

Activation volume is an intuitive quantity to study the evolution of dislocation structure, from nucleation to motion. In chapter 7, V^* will be further analyzed in the context of kink-pair mechanism.

6 Quantitative analysis of dislocation structure

Wedge indentation was applied on (001) oriented tungsten single crystal along the [110] direction (section 4.3.1). From the middle of the indents, cross section of the deformed material underneath an indent was prepared as electron-transparent lamella by FIB. Using TKD, the dislocation structures, i.e. the geometrically necessary dislocations (GNDs), their density and distribution were quantitatively characterized.

6.1 Analyzing TKD results

As introduced in section 4.3, the characterization of GND structures was conducted by the TKD measurement in an SEM, and subsequent analysis with MATLAB based on the MTEX toolbox [130, 131]. The GND analysis based on Nye's and Kröner's tensor [98,114,115] was implemented in MATLAB, the code used was modified based on an open-source code in GitHub [130, 131]. The detailed process of implementation is introduced step by step in the following sections, for a wedge indent to 2000 nm using the 90° wedge tip at indentation strain rate of 0.05 s^{-1}. The general analysis process is described in the sections from 6.1.1 to 6.1.4, then the reliability of this analysis is proved by comparing to the conventional analysis, i.e. KAM in section 6.1.5. Section 6.1.6 focuses on the influence of experimental setups on the results.

6.1.1 Orientation maps of wedge indents

The crystallographic orientation of the cross section was first determined and plotted as inversed pole figures of three orthogonal directions. Figure 6.1(a)-(c) shows IPF maps of x (RD, from left to right), y (TD, from up to down) and z (ND, out-of-plane) directions. Note that here the x, y, z directions are equivalent to the x_1, x_2, x_3 directions defined in Figure 2.7 in chapter 2. The data points of the three maps are plotted individually in Figure 6.1(d) in the IPF triangle. Due to the huge data volume of one TKD measurement (524288 data points of this measurement), one tenth of the data points were randomly plotted in each IPF triangle. The information about crystallographic orientation is indicated by the position of each point.

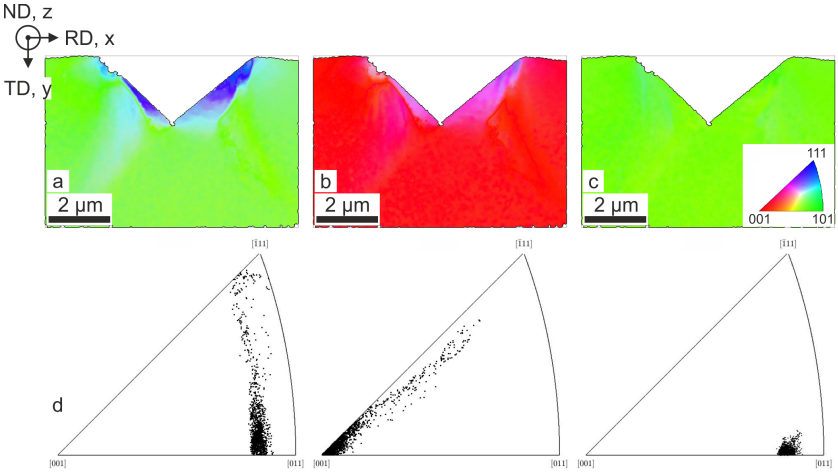

Figure 6.1
IPF map of three orthogonal directions (a) x (RD), (b) y (TD) and (c) z (ND). The corresponding IPF triangle is shown in the inset in (c); (d) individual data point positioned in IPF triangles. Most of the data points identified the orientation of the cross section in three directions, i.e. [011] in RD, [001] in TD and [011] in ND.

The IPF maps of *x*, *y*, *z* directions reflect the orientation in three dimensions. Before deformation, the original crystallographic orientation was confirmed [011], [001] and [011] (section 4.3.2). After wedge indentation, localized plastic deformation was observed near the indented surface. The change of color in Figures 6.1 (a) and (b) indicates that the orientation changes due to deformation and indicates the formation of subgrains and low angle boundaries. The orientation of the subgrains is not yet homogeneous, and the orientation gradient indicates that the stress-induced crystallization is not yet completed.

In Figure 6.1(d), the IPF triangles show the orientation of the individually measured points. In *x* and *y* directions, rotation happened in-plane. The lattice tends to rotate towards [111] orientation from its initial orientation, which was [011] in *x* and [001] in *y*. The measured orientation in *x* and *z* directions revealed a small deviation of $<10^{\circ}$ from the original orientation. This deviation is related to the misalignment between the TKD lamella and the detector. The lamella was likely tilted along the *y* axis resulting from the FIB preparation process and lamella mounting.

Both IPF maps and triangles give similar information, summarized as follows: Localized plastic deformation was observed close to the indent, concentrating symmetrically near the surface. Stress-induced crystallization occurred in this region; subgrains and low angle grain boundaries were generated. The lattice rotated in-plane in *x* and *y* directions over the *z* axis, while the orientation in *z* (out-of-plane) remains constant. The lattice rotation in *x* and *y* directions tends towards [111] orientation. These features were observed in all lamellae studied, which were prepared from indents under different loading conditions.

6.1.2 Lattice rotation calculated from Euler angle differences

As shown in Figure 6.1, the lattice rotation of wedge indentation experiments on bulk tungsten occurs in-plane. The quantitative characterization of lattice rotation is achieved by comparing the value of Euler angles from the deformed area to the Euler angles of the undeformed area (schematic shown in Appendix A.2). According to the definition [129], Euler angles describe the relation between two coordinate systems by three Bunge angles, φ_1, Φ and φ_2. After the three rotation processes, one coordinate system, e.g., x-y-z, can be rotated to match the other system. Here, the two coordinate systems are the sample system and the crystallographic system. Specifically, φ_1 describes the first rotation over the original z axis. After the first rotation, the original coordinate system x-y-z turned to x'-y'-z'. Φ is the rotation over x' axis after the first rotation. The coordinate system after the second rotation was denoted as x''-y''-z''. Then φ_2 is related to the rotation over z'' axis after the second rotation. φ_1 and φ_2 contain the information of in-plane lattice rotation, and Φ is related to the out-of-plane lattice rotation. Additionally, as the wedge indentation was designed for a plane strain deformation, according to Volz [136], Φ and φ_2 should remain constant before and after indentation, and only φ_1 should vary.

In the IPF maps (Figure 6.1), both deformed and undeformed areas were measured under the same condition on one cross section. Euler angles of the initial undeformed material were determined from the area far away from the indent, which can be identified in Figure 6.1(a)-(c). Euler angles of each measured point were then compared to the undeformed values, and the differences are directly related to lattice rotation angles. In Figure 6.2, the changes of the three Euler angles are shown.

As expected, the main angle difference occurs in $\mathrm{d}\varphi_1$ while $\mathrm{d}\Phi$ is approximately to zero. In the third map, $\mathrm{d}\varphi_2$ is observed to vary between -5° to 5°,

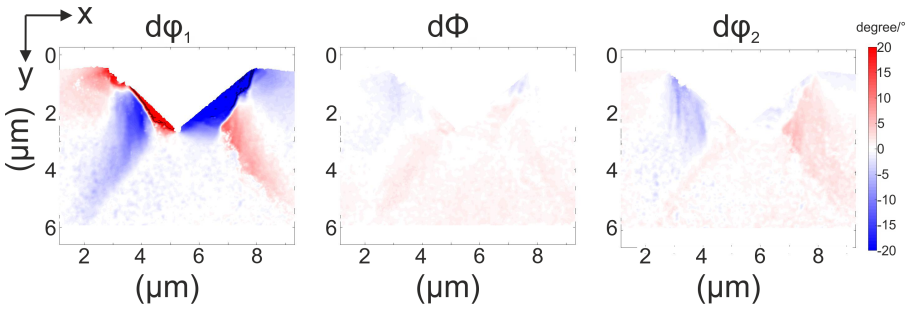

Figure 6.2
Deviation of three Euler angles from the original values. From left to right, the maps of $d\varphi_1$ (left), $d\Phi$ (middle) and $d\varphi_2$ (right) are shown. *x* and *y* axis describe the position of the measurement points in µm.

which is not surprising due to the misalignment (Figure 6.1). The lattice rotation can therefore be determined in terms of in-plane and out-of-plane angles, as shown in Figure 6.3.

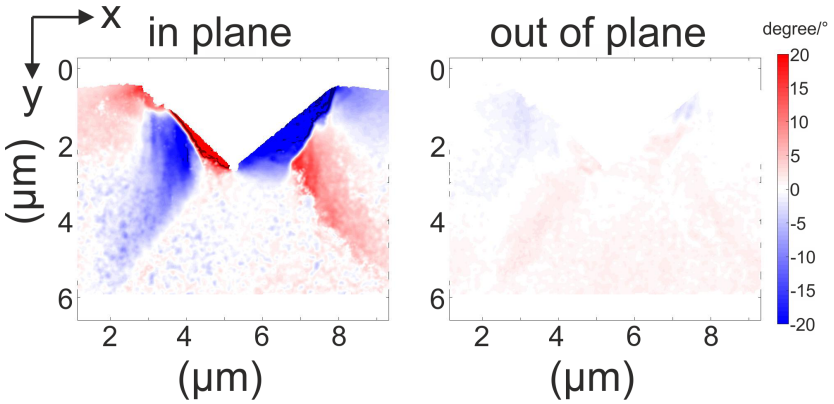

Figure 6.3
Lattice rotation map showing in-plane (left) and out-of-plane (right) rotation angles.

The lattice rotated in-plane anti-symmetrically on the left and right side of the indent, as indicated by the blue and red colors. The rotation angle reaches

values up to $\pm 20°$, and the maximum angles are found close to the deformed surface in the subgrain regions. The lattice rotation exhibits opposite direction on both sides of the indent. Directly beneath the indent, no lattice rotation has been detected, neither in-plane nor out-of-plane. Again, the non-existent lattice rotation out-of-plane confirms the plane strain condition of the experiment.

6.1.3 Calculating and visualizing curvature tensor

According to Nye's work [114], the dislocation tensor α_{ij} can be determined by the curvature tensor κ_{lk}, which is calculated as $\partial\theta_l/\partial x_k$ [98] (section 2.3.2 and 2.3.3). Experimentally, $\partial\theta_l$ is determined by the rotation around axis l and ∂x_k is the step size along axis k. As explained in section 2.3.3, under the plane strain condition only one non-zero $\partial\theta_3$ exists. As a result, only two vectors, κ_{31} and κ_{32} in the 3×3 curvature tensor are not equal to zero. In this context, for clarity, the x, y, z axes are denoted as x_1, x_2 and x_3.

In Figure 6.4, the distribution of curvature vectors are plotted in their recorded positions in x_1 and x_2. Data points of small values in $\pm 0.5\ \mu m^{-1}$ were removed for clarity. Data points of absolute values $>|0.5|\ \mu m^{-1}$ were shown by two colors reflecting their signs, i.e. positive in red and negative in blue. The full dislocation tensor α_{ij} is visualized as:

$$\alpha_{ij} = \begin{pmatrix} 0 & 0 & \kappa_{31} \\ 0 & 0 & \kappa_{32} \\ 0 & 0 & 0 \end{pmatrix} =$$

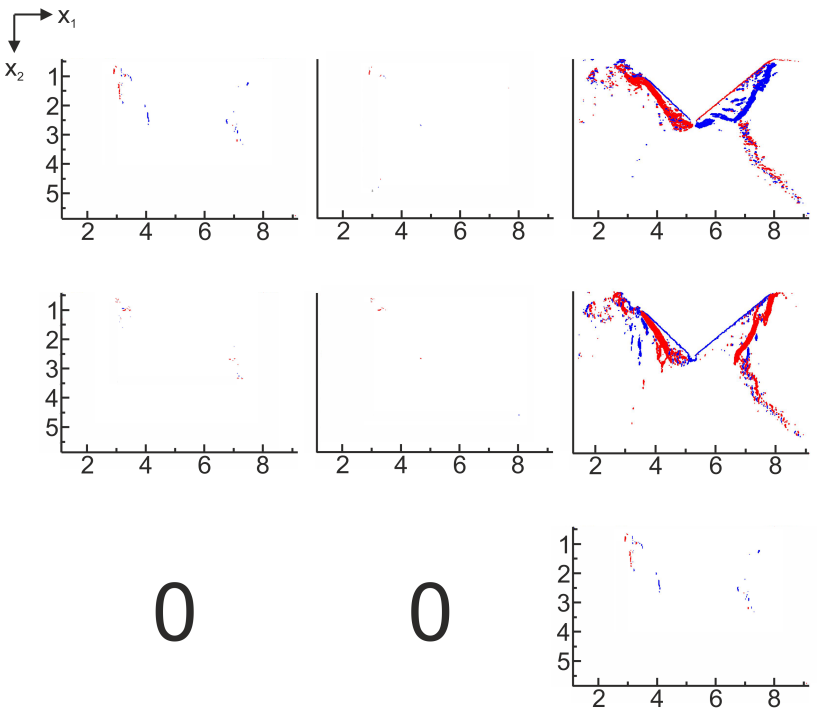

Figure 6.4
Plot of full dislocation tensor calculated by curvature tensor according to Nye [114] for plane strain deformation. The red points reflect the positive values of curvature vectors and the blue points are negative. Only the data points of curvature values >|0.5| μm^{-1} are shown in the plot, to figure the distribution of curvature and dislocation tensors. The position of individual data point can be read in x_1 and x_2 directions in µm.

Figure 6.4 shows the resulting dislocation tensor in two directions x_1 and x_2. Considering the scan direction during the TKD measurement, the two colors reflecting the opposite signs indicate the rotations in two opposite directions. Except for $\alpha_{13} = \kappa_{31}$ and $\alpha_{23} = \kappa_{32}$, α_{ij} approximate to zero. In the x_1 direction, κ_{31} reveals opposite values on the left and right-hand side, similar to the results in Figure 6.3. κ_{32} has the same sign on both sides of the indent, which confirms that the deformation in x_2 direction proceeds from top to bottom along the loading direction.

6.1.4 GND density of individual slip system

Since the dislocation tensor α_{ij} has been determined, the dislocation density of the individual slip system can be calculated independently according to Kröner tensor [115]. The slip systems were defined by assigning the corresponding Burgers vector $\vec{\mathrm{b}}_i$ and line vector $\vec{t}_j$ into the Kröner tensor. For bcc metal, the following glide systems are analyzed: $\{110\}\langle 111\rangle$, $\{112\}\langle 111\rangle$, $\{123\}\langle 111\rangle$. The line vector for edge dislocations $\vec{t}_e$ is therefore determined by the Burgers vector $\vec{\mathrm{b}}$ and the normal vector of the slip plane $\vec{n}$ as $\vec{t}_e = \vec{\mathrm{b}} \times \vec{n}$, and for screw dislocations $\vec{t}_s = \vec{\mathrm{b}}$ along the $\langle 111\rangle$ directions [98]. An example of a calculated GND map of the four systems, i.e. three edge dislocation systems and one screw dislocation system, is shown in Figure 6.5.

At indentation depth of 2000 nm loaded at $\dot{P}/P$=0.05 s^{-1}, the $\{110\}\langle 111\rangle$ system is the main and the only activated slip system for edge dislocations. In $\{112\}\langle 111\rangle$ and $\{123\}\langle 111\rangle$, almost no GNDs were observed as it can be seen in Figure 6.5(b) and (c). No screw dislocations were determined as shown in Figure 6.5(c), which confirms the dislocation tensor for plane strain deformation, as calculated in section 6.1.3.

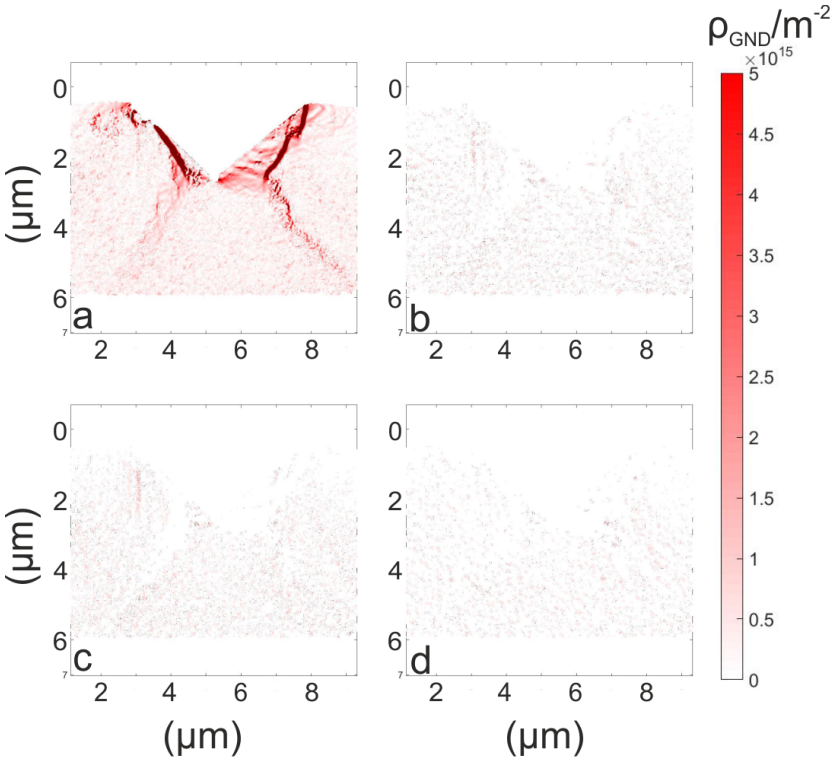

Figure 6.5
GND density distribution of individual slip systems of a wedge indent to 2000 nm at an indentation strain rate of 0.05 s^{-1}: (a) $\{110\}\langle 111\rangle$ edge dislocations, (b) $\{112\}\langle 111\rangle$ edge dislocations, (c) $\{123\}\langle 111\rangle$ edge dislocations, (d) $\langle 111\rangle$ screw dislocations. The distances on the x and y axes is shown in µm. The colorbars show the same range of dislocation density up to 5×10^{15} m^{-2}.

6.1.5 GND distribution and KAM map

As the GND density of the individual slip system was determined, resolving total GND density is easily achieved by adding up the densities of all systems, because they are independent of each other. The total GND density distribution of the sample presented in Figure 6.5 is shown in Figure 6.6(a). For comparison, the dislocation density calculated with KAM (see section 2.3.1) is shown in Figure 6.6(b).

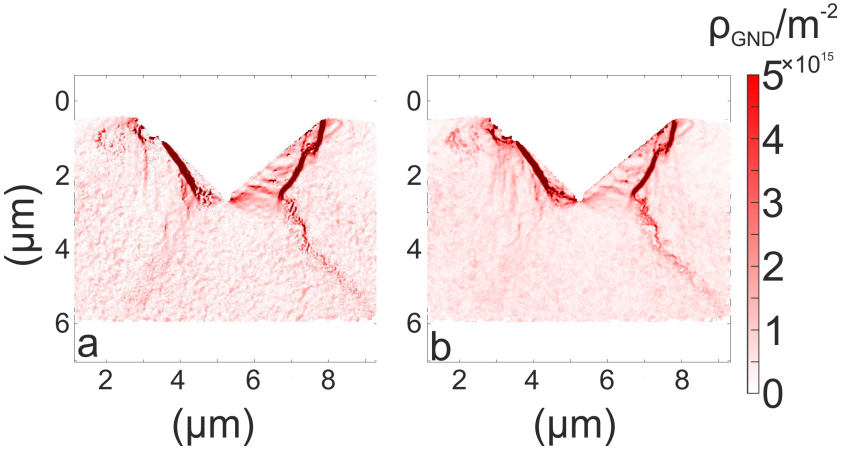

Figure 6.6
Total GND density distribution determined by (a) Kröner tensor (b) and KAM. Dimensions on *x* and *y* axes are in μm.

The GND density (m^{-2}) determined from KAM is a simple conversion from misorientation (rad). This output reflects directly the experimentally measured result. The GND density determined using the Kröner tensor and based on 2D TKD measurements is usually regarded as a lower limit of dislocation density. In this work, the GND density estimated by these two approaches yield very similar results compare Figure 6.6 (a) and (b). This confirms on one hand, that the implementation of the Kröner tensor analysis is robust and indeed reflects

the experimental result. On the other hand, 2D TKD measurement is an accurate method for determining plastic deformation on the premise of plane strain condition.

The magnitude of GND density (10^{15} m^{-2}) determined here shows good agreement with literature data [17, 19]. In Figure 6.6, some characteristic features should be pointed out: On the free surface, a small material pile-up can be seen at the edge of the wedge indent. Distinctive regions with the highest dislocation densities can be seen in the vicinity of the indent to the left and right. From the pile-up into the bulk of the material, low angle grain boundaries (LAGB) have formed. Basically, the butterfly-shape LAGBs are symmetric from the both sides of the indent. At the bottom of the indent, starting from the LAGB, lines of higher GND density have occurred, lying out on angle of $\sim 35^{\circ}$ to the vertical axis. No GNDs were observed right underneath the indenter tip.

6.1.6 Reproducibility

The last validation of this analysis process is to confirm the reproducibility and to ensure, that the results do not depend on the experimental setups used. In addition to the measurement by the high definition EBSD detector $e^{-}Flash^{HD}$ (QUANTAX EBSD, Bruker Nano GmbH, Berlin, Germany), another sample was indented using the identical parameters, and the TKD measurement was repeated using an AZtec EBSD system (Oxford Instruments GmbH, Wiesbaden, Germany). The TKD results were analyzed the same way, and the total GND density distributions are compared in Figure 6.7. The step size of the two measurements were 17 nm and 20 nm, respectively.

The measurement for Figure 6.7(a) was completed within 1 hour, while the scan for Figure 6.7(b) took more than 4 hours. The long scan time caused drift resulting in the horizontal shifts at a depth around 1.5 µm and underneath the indent (marked by the dashed frames in Figure 6.7(b)). Overall, use of

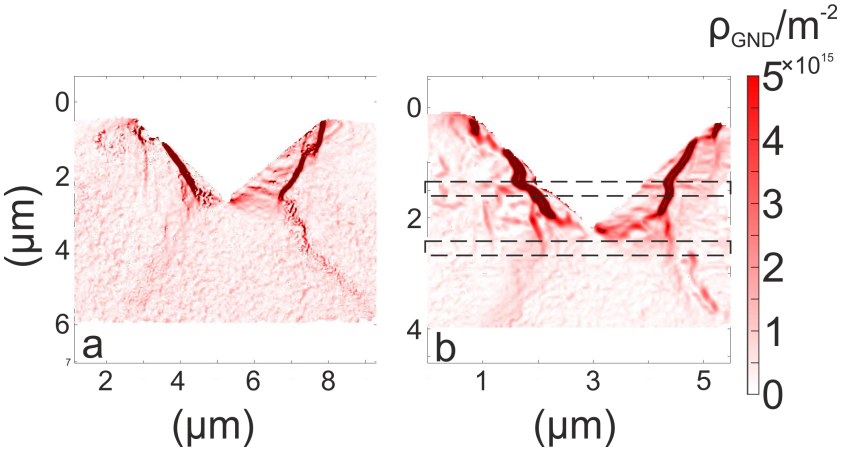

Figure 6.7
Total GND density distribution based on experimental data recorded using two different EBSD systems: (a) e$^-$Flash^{HD} (QUANTAX EBSD, Brukers), and (b) AZtec EBSD system (Oxford Instruments). In scan (b), the dashed frames mark the horizontal shifts due to the long operation time.

different EBSD detectors resulted in the same characteristics of the dislocation structures.

Furthermore, the effect of the step size of the TKD measurement on the GND density was investigated. The same TKD lamella was scanned twice using different step sizes, i.e. 12 nm and 23 nm using the e$^-$Flash^{HD} (QUANTAX EBSD, Brukers). The comparison is shown in Figure 6.8.

The different step size only influences the resolution of the GND maps but has no significant effect on the calculation of density. While the reduced step size gives a higher resolution of the structure, the noise signal increases. A suitable step size balancing resolution and noise needs to be selected. For the characterization of tungsten a step size in the range from 10 nm to 20 nm was considered suitable.

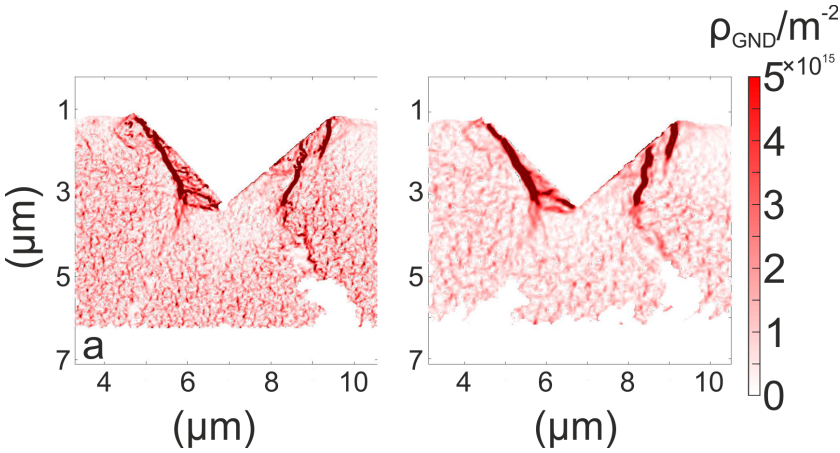

Figure 6.8
Total GND density distribution based on experimental data recorded using e⁻Flash^{HD} (QUANTAX EBSD, Brukers). The step size of the scan was (a) 12 nm and (b) 23 nm.

6.2 Depth dependence of GND distribution

As shown in chapter 5, tungsten exhibits a bi-linear ISE of the hardness. In the framework of strain gradient plasticity, depth-dependent hardness is associated with the GND density. Thus, the GND structure is expected to be different at different depths. In this work, the transition of the two depth regimes was observed at ∼300 nm. Wedge indents using the 90° wedge were conducted on (001) oriented tungsten at an indentation strain rate of 0.05 s^{-1} to four depths, i.e. 150 nm, 200 nm, 500 nm, and 2000 nm. The TKD measurement was conducted using the AZtec EBSD system (Oxford Instruments). The calculated total GND density distribution of the four samples are shown in Figure 6.9.

Since the TKD scan for the 500 nm and 2000 nm depths took longer than two hours, the unavoidable drift caused horizontal distortion in Figure 6.9 (c) and (d) (marked by the dashed frames). A higher noise signal appears in (b) due to the curved lamella during the FIB preparation. The change of the GND

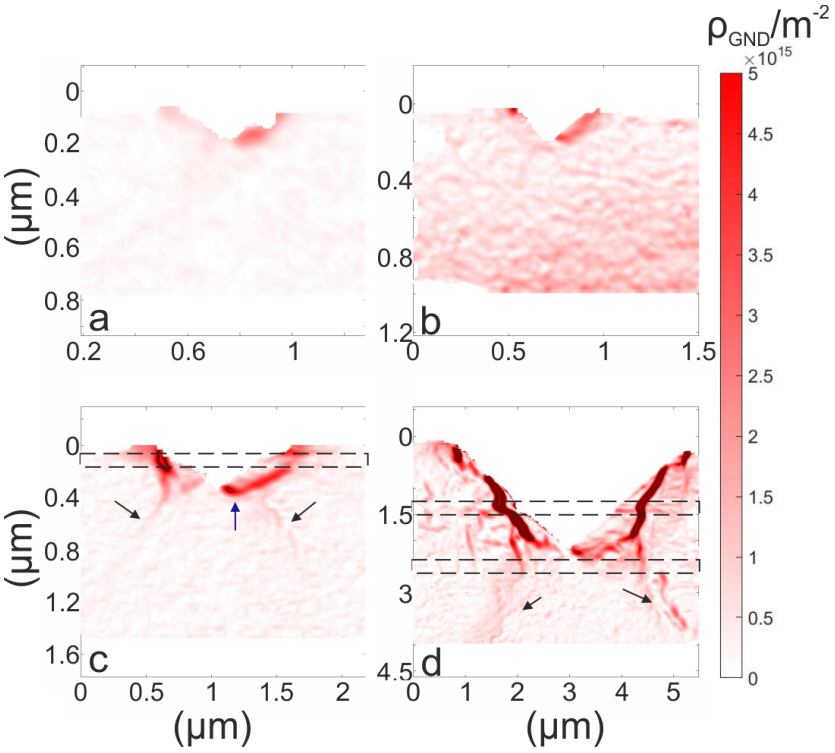

Figure 6.9
Total GND density distribution at different indentation depths: (a) 150 nm, (b) 200 nm, (c) 500 nm, (d) 2000 nm. Scan caused horizontal shifts were marked by the black frames. From 500 nm indentation depth, subgrains formed, marked by the blue arrow. The black arrows indicate the lines containing higher GND density. Note, that the size of the scans increases from (a) to (d). The *x* and *y* axes are shown in μm.

structure with increasing displacement is significant. At the smaller depth (Figure 6.9 (a) and (b), the GNDs concentrated quite locally around the indent; the highest density occurs near the surface. There is no significant difference between the two shallow indents. However, with increasing depth, a GND dense line reaches from the surface into the bulk and subgrains appear in Figure 6.9(c) showing the indent at 500 nm (see the blue arrow). In addition, two symmetric lines of higher GND density were generated beneath the subgrains (marked by the black arrows), at $\sim 35^{\circ}$ to the vertical axis. From 500 nm to 2000 nm indentation depth (Figure 6.9 (c) and (d)), GND density increases, and more GNDs concentrated at the low angle grain boundaries. In conclusion, the dislocation structures at the smaller depths of 150 nm and 200 nm are comparable. With increasing depth, i.e. from 200 nm to 500 nm, the GND structure changed. At larger depth, i.e. 2000 nm, no further changes were observed and the GND structure remained stable.

From the small to the large depth regime, the GND structure became less sensitive to misalignment between the indenter tip and the sample surface. The asymmetric distribution at small depth became more symmetric with increasing depth. Additionally, another region of highly concentrated GND was observed under the pile-up, which became larger for larger depth. The size-dependent evolution of dislocation structures corroborates the observation in hardness testing, which revealed a bi-linear ISE (section 5.1), and gives direct evidence of the microstructural changes.

6.3 Strain rate dependence of GND distribution

As shown in Figure 5.4, the hardness is highly strain rate dependent. Moreover, the strain rate sensitive hardness even exhibits different behaviors in the large and small depth regime, similar to the bi-linear ISE. Therefore, the effect of two

different indentation strain rates, i.e. 0.5 s^{-1} and 0.005 s^{-1}, on the resulting GND structures was investigated for 2000 nm and 200 nm indentation depth. The GND maps of slow and fast indents are compared in Figure 6.10.

In Figure 6.10, GND maps of slow and fast indents are shown in the left column (Figure 6.10 (a), (c), (e)) and in the right column (Figure 6.10 (b), (d), (f)), respectively. The total GND density is shown in Figure 6.10 (a) and (b), while distribution of edge dislocations for $\{112\}\langle111\rangle$ and $\{123\}\langle111\rangle$ systems are shown in Figure 6.10 (c), (d) and (e), (f), respectively.

Comparing the total GND density of slow and fast indents in (a) and (b), no significant change in GND structure has been observed. However, two differences need to be mentioned. Dislocation density has increased in the subgrains near the indent center when the strain rate was increased (marked by the black arrows in Figure 6.10(a)). Furthermore, at the higher strain rate, vertical lines containing higher dislocation density can be seen, as marked by the blue frames in Figure 6.10. According to the GND densities of the individual slip systems (compare Figure 6.5), the main GND density is contributed by the $\{110\}\langle111\rangle$ edge slip system. While the indentation in Figure 6.5 was made at a strain rate of 0.05 s^{-1}, this is still the case for the slower and faster strain rates of 0.005 s^{-1} and 0.5 s^{-1}. However, at the higher strain rate, the $\{112\}\langle111\rangle$ and $\{123\}\langle111\rangle$ systems started to be active (compare Figure 6.10). The occurrence of $\{112\}\langle111\rangle$ and $\{123\}\langle111\rangle$ dislocations at higher strain rate confirms that, $\{110\}\langle111\rangle$ is the most easily activated edge slip system at lower strain rate at room temperature. The activation of $\{112\}\langle111\rangle$ and $\{123\}\langle111\rangle$ is thermal, which requires usually higher temperature [43], or at higher strain rate as being observed in this work.

The difference between slow and fast indents is much more significant at 200 nm indentation depth. In Figure 6.11(a), at a strain rate of 0.005 s^{-1}, the dislocation density is much lower and no distinct regimes of higher concentration can be observed, while the dislocation density at the higher strain rate was apparently high enough to allow for the formation of low angle grain boundaries

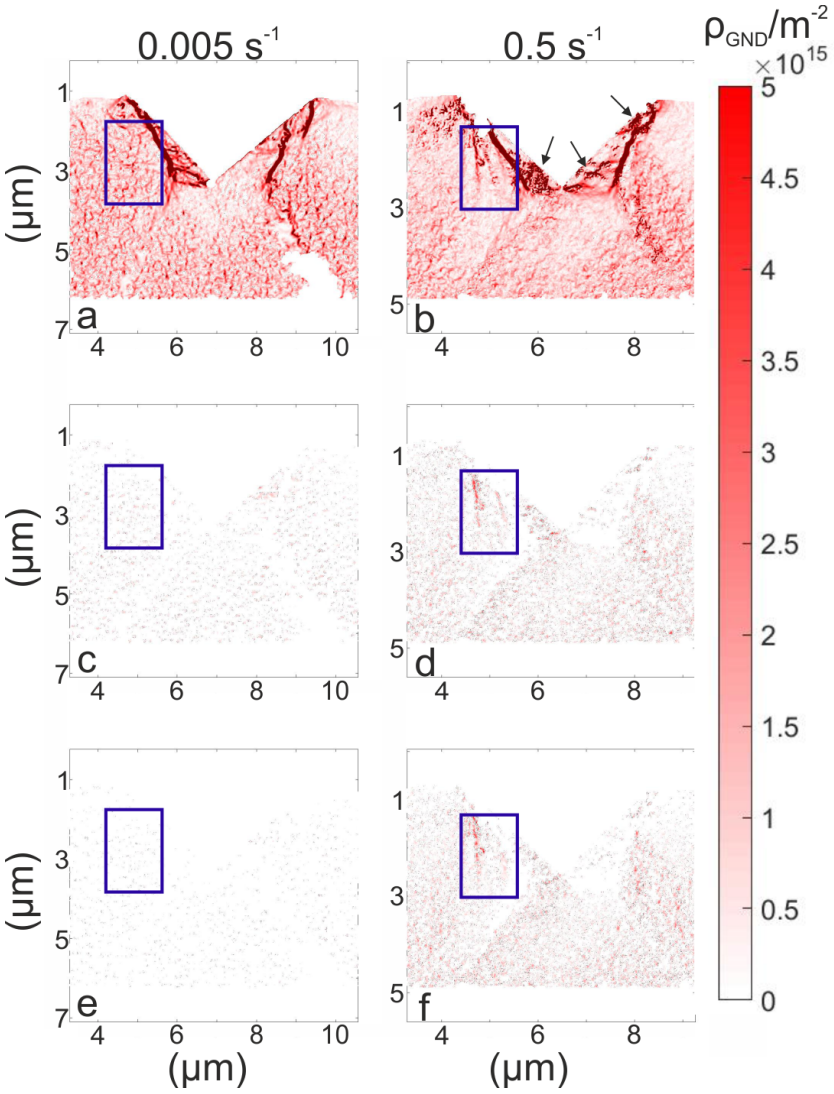

Figure 6.10

GND density distribution at two different strain rates: the total GND density is shown in (a) for 0.005 s^{-1} and (b) for 0.5 s^{-1} indents. Higher GND density was found in the center of the fast indent, as shown by the black arrows. (c), (d) show the GND density distribution of $\{112\}\langle 111\rangle$ edge dislocation system for 0.005 s^{-1} and 0.5 s^{-1}, respectively. (e), (f) show the GND density distribution of $\{123\}\langle 111\rangle$ system for 0.005 s^{-1} and 0.5 s^{-1}. In the blue frames in (c)-(f), GNDs reveal different densities at the two strain rates.

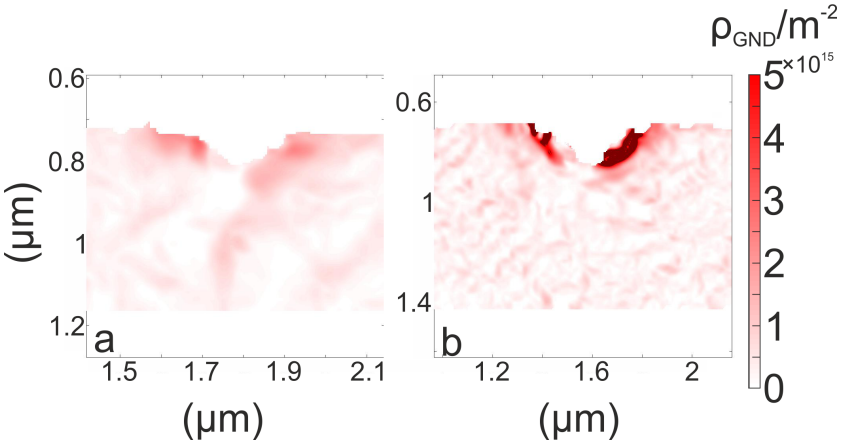

Figure 6.11
Total GND density distribution of (a) slow and (b) fast indents to 200 nm. Colorbar unified up to 5×10^{15} m^{-2}.

(Figure 6.11(b)). Comparing Figure 6.11 with Figure 6.9(b), the increase of GND density with increasing strain rate and the consequent occurrence of low angle grain boundaries is recognizable. At small indentation depth, the strain rate apparently has a more pronounced influence on dislocation structure than at the larger depths.

Furthermore, the mean GND densities of the four samples shown in Figure 6.10 and 6.11 were calculated along the x axis averaging the data over a defined distance in the y-direction of the respective x position. The number of data points at each x position was kept constant by selecting the same depth range from the surface, i.e. 200 nm for the shallow indent and 2000 nm for the deep indent. In Appendix A.3, a schematic diagram is shown in Figure A.3 for explaining the analysis of mean GND densities. The results are shown in Figure 6.12. The position along the x axis has been normalized by the lateral size of the indent.

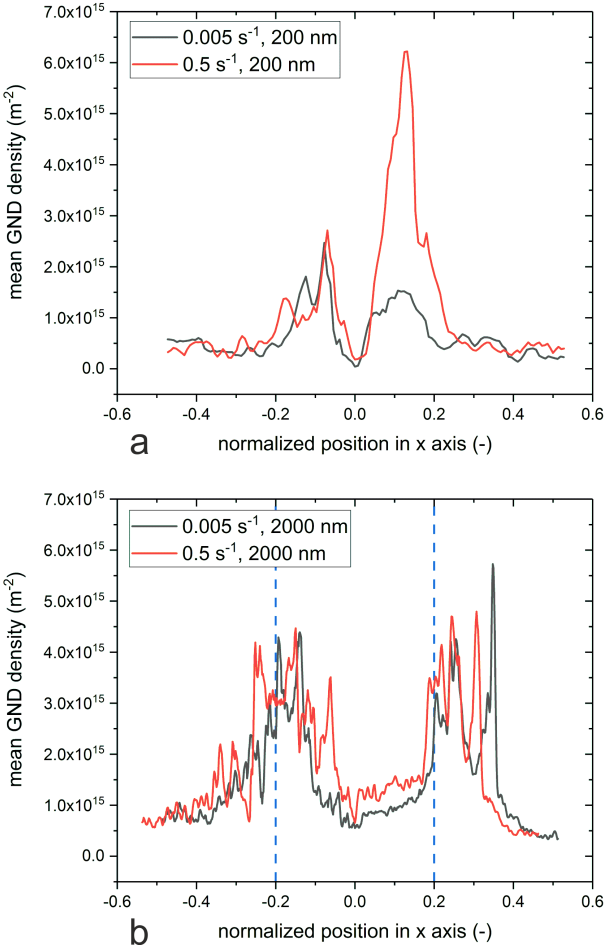

Figure 6.12
Comparison of mean GND density at (a) 200 nm indentation depth (a) and (b) 2000 nm for two different strain rates, i.e. 0.005 s^{-1} and 0.5 s^{-1}. The densities at the different x positions were averaged over a defined distance along the y axis. The center of the indent is located at x=0 and the x positions were normalized by the width of the scanned area. Two blue dashed lines mark the center region of the indent to 2000 nm depth.

Misalignment between the normal loading axis and the sample surface plays an important role at the small depth and its influence becomes less when the indentation depth increases. The GND density to the left and right of the indent is quite asymmetric at the small depth (Figure 6.12(a)) and becomes more symmetric at the larger depth (Figure 6.12(b)). In the middle where x is zero, the GND density has a minimum for both depths. This analysis also indicates, that the difference of GND density between two strain rates is larger at the small depth than at large depth. With increasing strain rate, more GNDs were generated in the center region of the indent, i.e. between the positions of -0.2 to + 0.2 along the x axis in Figure 6.12(b) (see the blue dashed lines).

6.4 Constraint effects

In order to understand the influence of the material constraints on the dislocation structure, three different conditions were considered: Wedge indentation with two different wedge angles, i.e. 60° and 90°, and indentation of a thin section, i.e. "bridge", using the 90° wedge (see section 4.3.1). The corresponding IPF maps are shown in Figure 6.13 along three orthogonal directions x, y and z.

For the case of the "bridge" (Figure 4.6), the TKD lamella was carefully prepared by FIB from the middle section of the bridge. The GND densities under the three conditions are shown in Figure 6.14.

In Figure 6.13, all the three samples reveal in-plane deformation, that the most rotations were observed occurring in x and y directions (Figure 6.13 (a)-(f)). For the cases of the two wedge indentations on bulk material, the in-plane deformation is expected as a result of plane strain condition. For the case of "bridge", since the TKD measurement was conducted on the middle slice, a plane strain deformation is able to be captured. Comparing to 90° wedge indentation on bulk material shown in Figure 6.13 (b), (e), (h), the deformation

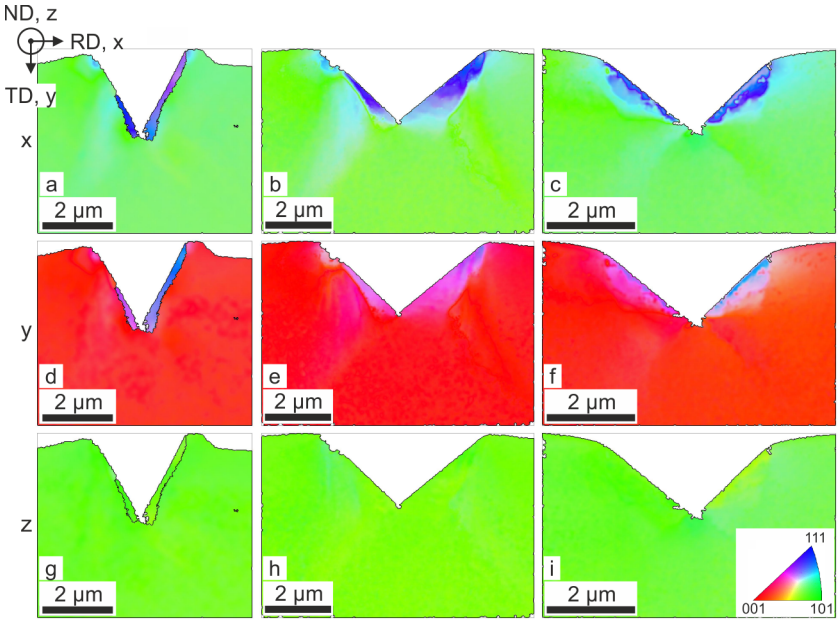

Figure 6.13
IPF maps of wedge indents to 2000 nm indentation depth with different constraint conditions along (a)-(c) *x*, (d)-(f) *y*, (g)-(i) *z* scan directions. IPF maps of 60° wedge indentation on bulk material are shown in (a), (d), (g) in the left column. (b), (e), (h) in the middle column show the IPF maps of 90° wedge indentation on bulk material. The right column represents the IPF maps of 90° wedge indentation for the "bridge" case. The IPF triangle is shown in the inset in (i).

by the 60° wedge was more localized with a higher lattice rotation angle (Figure 6.13 (a), (d), (g)). The difference of lattice rotation angles between the left and right side reached a maximum of ±40°. Low angle grain boundaries, which were found beneath 90° wedge indents, were replaced by high angle grain boundaries in the case of 60° wedge indents. The grain boundaries are indicated by the black lines in Figure 6.13 (a), (d) and (g). Comparing the 90° wedge indents into the bulk and the thin section (Figure 6.13 (c), (f), (i)), the deformed zone exhibits a different feature, that the butterfly-shape subgrains in the bulk became semicircles in the thin section. Also, the color gradient in the

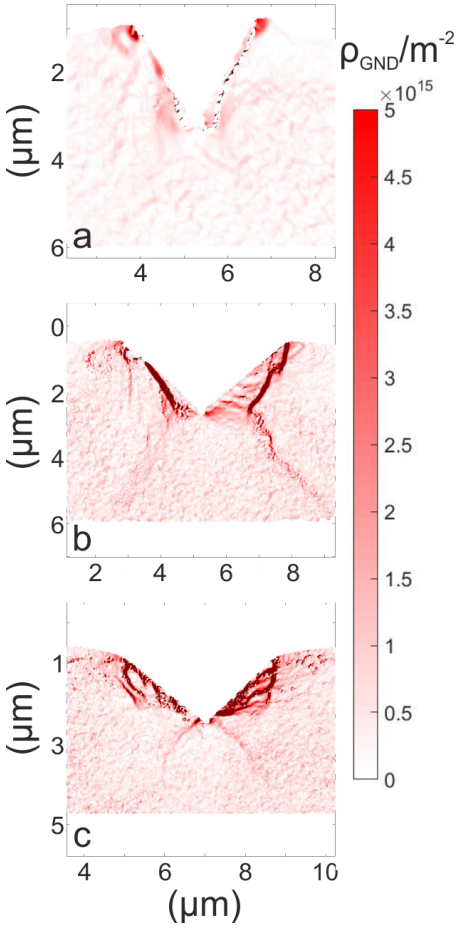

Figure 6.14
Total GND maps under different constraints: (a) 60° wedge indentation on bulk material, (b) 90° wedge indentation on bulk material, (c) 90° wedge indentation on an thin slice.

subgrains of the bulk (Figure 6.13 (b) and (e)) is smoother than the "bridge" sample (Figure 6.13 (c) and (f)), indicates a more uniform microstructure in the subgrains. While less GNDs were found in the subgrains of indent on bulk (Figure 6.14(b)), several curves of concentrated GND density appeared in the subgrain zone of the "bridge" case ((Figure 6.14(c)).

The material constraints of the three cases decrease, shown in Figure 6.13 from the left to the right column. Notable material pile-ups occur on the free surface at the edge of the 60° wedge indent, and become less pronounced at the edge of the 90° wedge indent into the bulk. When the 90° wedge indentation was conducted on the thin section, instead of the pile-up, sink-in appeared. The shape of the (sub-) grains changed from butterfly to semicircle correspondingly (Figure 6.13 and Figure 6.14). In Figure 6.14, the GND density distribution also exhibits different features, as the constraints differed. With disappearing pile-ups, the curves of higher GND density underneath the pile-up vanished (Figure 6.14 (a)-(c)). Lines of higher GND density appear beneath the subgrains, keep showing on the angle $\sim$35° to the vertical axis, which appears to be independent of the constraint effect of the material.

7 Discussion

As indicated by the experimental results (chapter 5), the dislocation nucleation process in single crystalline tungsten is independent of the loading velocity at room temperature. According to the experiments, the maximum shear stress τ_{max} and the nucleation related activation volume V_y^* exhibit no dependency on the varying loading rates ranging from 0.05 to 0.5 mN/s (section 5.2.1). Also, quasi-static CSR indentation at strain rates ranging from 0.005 s^{-1} to 1.6 s^{-1}, revealed no dependency on indentation strain rate for both the pop-in load P_{pop-in} and τ_{max} (see in Appendix A.4).

By contrast, the hardness, or flow stress exhibited clearly strain rate sensitive behavior in the CSR indentation experiments (section 5.2.2). When the strain rate increases, the hardness increases correspondingly. This behavior corroborates that the dislocation motion in tungsten single crystal, as a typical bcc metal, is thermally activated. The strain rate sensitivity of the hardness, together with the bi-linear ISE (Figure 5.4), suggest different behaviors in the different depth regimes. First, a model describing the bi-linear ISE at various strain rates is introduced and validated by the experimental data. Then, the indentation induced dislocation structures are further analyzed, for a better understanding of the plastic deformation mechanisms of the single-crystalline tungsten.

Bi-linear ISE has been observed at indentation strain rates for single crystalline tungsten as shown in Figure 5.2 and Figure 5.4. This behavior was observed using different instruments and indentation methods. Also, the effect of the dynamic measurement was excluded, as shown in Appendix A.5. Rather, the

bi-linear effect is related to the intrinsic properties of single crystalline tungsten.

The observation of two different regimes is supported by the GND maps obtained for indents to different depths (see in Figure 6.9), which suggest a structural transformation of dislocations, in the depth range between 200 nm and 500 nm for the 90° wedge tip. At the smaller depths of 150 nm and 200 nm, dislocations around the deformed surface but yet no concentrated dislocation line was found. At the larger depths, subgrains were formed and clear subgrain boundaries as well as GNDs accumulating along certain directions appeared. At both small depth and large depth, the GND distributions are inhomogeneous, similar as reported in [116, 137].

Qualitatively, ISE is attributed to the increase of GNDs, namely the strain gradients according to strain gradient plasticity [9, 11]. The increased hardness value at smaller depth is directly associated with the GND density. According to the Nix-Gao model [9], H^2 is linearly proportional to $1/h$. However, since the experimental results of single crystalline tungsten reveal significant bi-linear ISE, the Nix-Gao model is cannot describe the complete depth range of the nanoindentation experiments.

7.1 Introduction and validation of the bi-linear ISE model

In the following, the basic assumptions of the Nix-Gao model [9] will be evaluated. Two fundamental conditions were assumed to estimate the GND density beneath an indent: 1), the GND volume is hemispherical and its radius a is equal to the radius of contact area, 2), the spacing between two slip steps, each containing one dislocation, is uniform over the GND volume. In the Nix-Gao model, GNDs are closely packed, so that the constant spacing s can be calculated by $s = a\mathrm{b}/h$, where b is the magnitude of Burgers vector and h the

indentation depth. In this case, the hemispherical volume is saturated with GNDs, which means that GND density is maximum when the volume does not change.

The measured hardness of shallow indents (<300 nm), though, is lower than predicted by the Nix-Gao model (section 5.1.1, Figure 5.2). Considering the relationship between hardness and dislocation density, in this depth range, the assumed GND density, thus, needs to be diluted.

The shortcomings of the Nix-Gao model at smaller length scales were realized [10,59] and modifications of the model suggested [62,63,67,68]. Most of them reduced the GND density by assuming an enlarged GND volume [59, 62]. If the GNDs concentrated in the hemispherical volume, the high density in the volume would move the dislocations outward and the volume would increase. While such an approach is efficient and can reduce the overestimation of the hardness in the Nix-Gao model, the change in behaviors in the different depth regimes has not been addressed.

As pointed out by Swadener et al. [59], the two assumptions in the Nix-Gao model are difficult to be fulfilled at the same time. Either the GND volume needs to be extended, or the GND density needs to change continuously over the volume from maximum to approximately zero during the indentation process. For the case of tungsten single crystals, SEM images of cross sections beneath both Berkovich and wedge indents (Figure 6.14) indicate that even though the deformation zone is not perfectly hemispherical as assumed in the model, the assumption for the range of GND volume is not unreasonable. However, as presented in chapter 6, the GND maps under different conditions show that the GND distribution inside the deformation zone is not uniform. Therefore, it is suggested to rethink the second assumption and adapt the assumption of a uniform dislocation spacing. In this work, the dislocation spacing is assumed non-uniform and dependent on the position r away from the center of the indent.

Furthermore, the non-uniform spacing $s(r)$ of slip steps is assumed to increase from the indent center to the edge, so that the number of GNDs decreases. In the center of the indent ($r = 0$), $s(r)$ is minimal and equal to the constant dislocation spacing $s = \mathrm{b}/\tan\theta$ according to the established Nix-Gao model, with θ describing the tip geometry (see section 2.2). At the edge of the indent ($r = a$), $s(r)$ should approximate to positive infinity, because the indentation induced plastic zone ends. These two boundary conditions can be written as:

$$\frac{s(r)}{s} = \begin{cases} 1, & \text{for } r = 0, \\ +\infty, & \text{for } r = a. \end{cases} \tag{7.1}$$

Introducing the size of GND volume by a and the location of a slip step r, the equation can be rewritten as:

$$\frac{s(r)}{s} = \frac{a}{a-r}. \tag{7.2}$$

According to equation 7.2, $s(r)$ increases linearly from center to edge, from s to positive infinity, respectively. Equation 7.2 can be transformed as follows:

$$s(r) = \frac{a}{(a-r)} \frac{\mathrm{b}}{\tan\theta}. \tag{7.3}$$

The equation 7.3 is the same as equation 22 in Nix' and Gao's original paper [9], which was based on a different assumption, though. For the modification, a constant strain gradient was assumed, as already in the original paper the shortcomings of the assumptions were realized. According to [9], the dislocation spacing would no longer be uniform, when a constant strain gradient would be sustained. Analogous to the Nix-Gao model, the total length of the injected loops $\lambda(r)$ with respect to the location-dependent dislocation spacing can be rewritten as:

$$\lambda(r) = \int_0^a \mathrm{d}\lambda(r) = \int_0^a 2\pi r \frac{\mathrm{d}r}{s(r)} = \frac{\pi h a}{3\mathrm{b}}. \tag{7.4}$$

GND density can be then calculated if the total length of the dislocation loops is determined, using equation (7.4). The GND volume is defined as in the Nix-Gao model because experimental results have shown that the size is reasonable. Thus, diluted GND density based on the modified assumption described above, is:

$$\rho_{G,\text{diluted}} = \frac{1 \tan^2 \theta}{2\text{b}h}. \tag{7.5}$$

Compared to the Nix-Gao model, the GND density of equation 7.5 has been diluted to one-third of the original prediction. Correspondingly, the material characteristic length scale h^*_{diluted} is reduced to one third of the original h^*:

$$h^*_{\text{diluted}} = \frac{27}{2}\text{b}\alpha^2 \tan^2 \theta (\frac{\mu}{H_0})^2 \tag{7.6}$$

with μ as the shear modulus and H_0 the depth-independent hardness. α is the Taylor factor, which came originally from the concept of dislocation core parameter [9, 21, 138]. For a certain material, α is constant as long as the dislocation structure does not change, which might be influenced, though, by varying the strain rate or temperature. In the previous analyses [9, 62, 63], α was always taken as 0.5. The dislocation distribution according to the adapted model described above is illustrated in Figure 7.1:

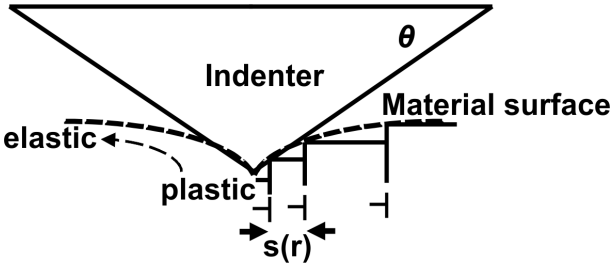

Figure 7.1
Schematic illustration of GND distribution beneath the indent according to the adapted model of diluted GND density.

In contrast to the Nix-Gao model, which describes a saturated hemispherical volume, the GND volume of the adapted model is not yet saturated. The assumption of non-uniformity does not only yield a reduced GND density, but the description of GND distribution also becomes more realistic. The material being indented is considered as continuously deformed from the plastic zone to the elastic zone, where no GND have been generated. Dislocations transmit from center to the edge of the deformation volume due to the dislocation density gradient. With increasing indentation depth, the central part underneath indent will be filled with GNDs eventually, and the saturated state will be achieved. When the indenter continues to penetrate into the material, the ratio of saturated to unsaturated GND volume would continually increase. Such a dynamical picture was recently confirmed experimentally [137]. Javaid et al. [137] indented single crystalline tungsten, and characterized the sample surfaces by EBSD and ECCI. A gradual decrease of GND density from the indent center to the edge at small depth was reported, while the density became more homogenized at a higher load. [137].

For very small h, the influence of the elastic portion of the material is not negligible. As a result, the indenter would first have full contact with the material close to the tip, there the material adapts rigid to the tip geometry. The radius of the full contact zone is defined as r_0. At the start of plastic deformation, there exists only one slip step of height 1b in the full contact zone and the spacing $s = \mathrm{b}/\tan\theta$ equals to the s of closely packed GNDs. With the indenter penetrating deeper into the material, the full contact zone extends further. In the region from the center to r_0, one slip step, that had occupied a large $s(r)$, would then separate into several slip steps of the constant spacing s to fulfill the geometrical condition of the indenter. Thus, more GNDs generate and become closely packed in the full contact volume ($r \leq r_0$), as described in the classic model. With increasing indentation depth, the proportion of saturated to unsaturated GND volume keeps growing, until the influence from the elastic portion of the material becomes negligible and the saturated dislocation distribution is

predominant. From small to large depth regimes, the GNDs gradually fill the diluted spacing of slip steps and the unsaturated volume becomes saturated. In conclusion, the transition of dislocation mechanisms of two regimes can well explain the experimental observations, such as the structural transformation of GNDs at different indentation depths, as well as the bi-linear ISE observed in the nanoindentation hardness testing.

Assuming that the transition of two regimes occurs at the depth h_0, the suggested model combines two dislocation mechanisms describing the bi-linear ISE:

$$H^2 = \begin{cases} {H_0}^2 + {H_0}^2 \cdot \frac{h^*}{h}, & \text{when } h \geq h_0, \\ {H_0}^2 + {H_0}^2 \cdot \frac{2}{3} \cdot \frac{h^*}{h_0} + {H_0}^2 \cdot \frac{1}{3} \cdot \frac{h^*}{h}, & \text{when } h < h_0 \end{cases} \tag{7.7}$$

with the same expression for h^* as in the Nix-Gao model [9],

$$h^* = \frac{81}{2} \mathrm{b} \alpha^2 \tan^2 \theta (\frac{\mu}{H_0})^2. \tag{7.8}$$

The bi-linear ISE model was validated by comparing it to the experimental data. The mean value of hardness for (001) single crystal determined using the dynamic stiffness measurement (CSM) and the Nano Indenter G200 XP (see section 4.2) is shown in Figure 7.2 together with the suggested model described by equations 7.7 and 7.8.

For α in equation 7.8, a value of 0.5 was assumed [9, 62, 63]. Other parameters, such as Burgers vector b, shear modulus μ and equivalent tip angle θ are constant depending on the material and tip geometry. Relevant parameters such as H_0, h^* and h_0 in equation 7.7 were determined as follows: hardness data of large depth regime from 500 nm to 2000 nm were fitted by the original Nix-Gao model, yielding H_0. Then, h^* was calculated according to equation 7.8. Subsequently, h_0 was estimated using the hardness data of the small depth regime from 100 nm to 200 nm using equation 7.7. The size effect as described by the new model expressed as the relation between H^2 and $1/h$, captures the

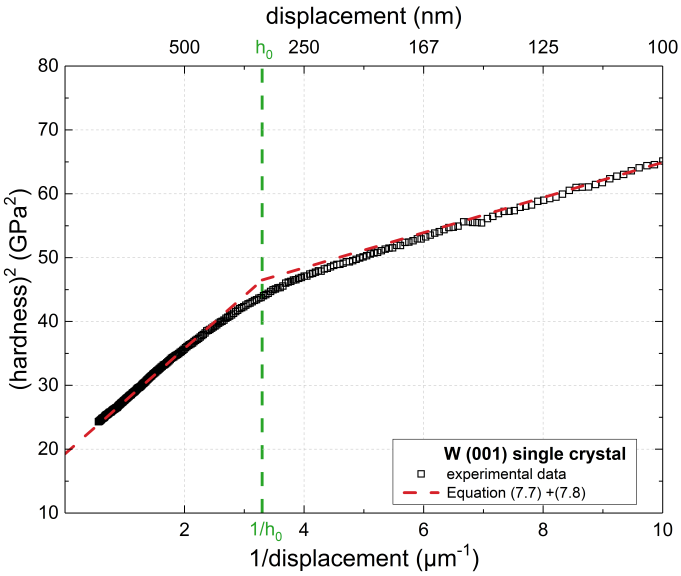

Figure 7.2
Indentation size effect of the (001) tungsten single crystal. The average of 20 indents is shown together with the bi-linear model described by equations 7.7 and 7.8. The experimental details can be found in section 4.2. For H_0 and h_0, 4.39 GPa and 303 nm were determined, respectively.

experimental behavior as indicated by the red dashed line in Figure 7.2. As expected, the transition of the two regimes occurs at h_0. The depth-independent hardness H_0 is determined as 4.39 GPa, which agrees well with the literature data for comparable experimental conditions [36, 41, 63]. The transition of the two regimes in equation 7.7 lies at the depth h_0 of 303 nm, as indicated by the green dashed line in this graph.

The bi-linear ISE model also describes the hardness behavior of the (112) crystal orientation as shown in Figure 7.3. For the (112) orientation, $\alpha = 0.44$ resulted in an improved description of the experimental data and the transition depth h_0 resulted in 286 nm. No significant difference compared to the behavior of the (001) orientation was observed.

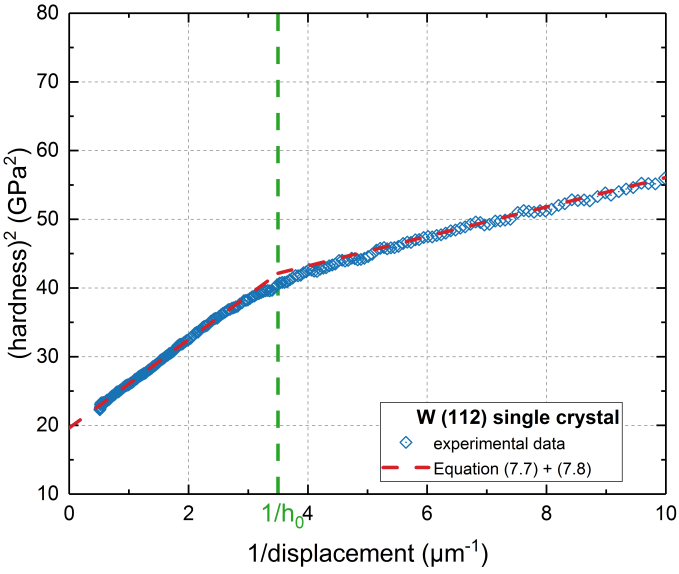

Figure 7.3
Indentation size effect of the (112) tungsten single crystal. The average of 20 indents is shown together with the bi-linear model described by equations 7.7 and 7.8. The experimental details are described in section 4.2. For H_0 and h_0, 4.43 GPa and 286 nm were determined, respectively.

Indentation hardness of single crystalline tungsten can be described very well by the bi-linear ISE model over the whole indentation depth after the onset of plastic deformation. However, experimentally the transition does not happen at a certain depth but rather at a depth range. As shown in Figure 7.2, the transition regime ranges from ∼250 nm to ∼350 nm. Near the transition depth h_0, the two regimes have to overlap since the deformed volume is occupied by dislocations gradually and the predominant GND mechanism has to change. In Figure 7.4, such evolution process of GND distribution at the different depth regimes was schematically represented.

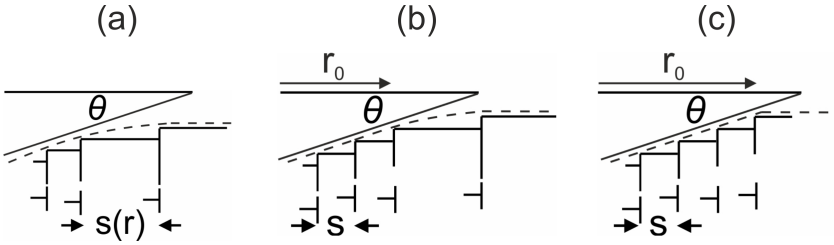

Figure 7.4
Schematic of GND distribution from small depth regime (a) to large depth regime (c). In (a), GND distribution fulfills the adapted model of diluted GND density, while (c) was illustrated after the Nix-Gao model. A mixed state of these two models is shown in (b). The saturated volume radius is characterized by r_0.

In the transition regime ((Figure 7.4(b)), influence from both the unsaturated and saturated GND distributions should not be neglected. Assuming a hemispherical volume with a radius of r_0 inside the total GND volume, in that the GNDs are closely packed, while out of that volume, the GND distribution follows the adapted model of diluted GND density. For h>h_0, the dense GND volume starts to dominate. Thus, it exists geometrically

$$\frac{h-h_0}{r_0} \approx \frac{h}{a} = \tan\theta. \tag{7.9}$$

From $r = 0$ to r_0, the GND spacing is equal to s, and the total length of the dislocation loops λ_1 in the dense GND volume is

$$\lambda_1 = \int_0^{r_0} 2\pi r \frac{\mathrm{d}r}{s} = \frac{\pi(h-h_0)r_0}{\mathrm{b}}, \tag{7.10}$$

while from r_0 to a, the dislocation spacing $s_2(r)$ is non-uniform, and can be described as

$$\frac{s_2(r)}{s} = \frac{a-r_0}{a-r_0-(r-r_0)} = \frac{a-r_0}{a-r}, \tag{7.11}$$

therefore, the length of the dislocation loops $\lambda_2(r)$ from r_0 to a is calculated as

$$\lambda_2(r) = \int_{r_0}^{a} 2\pi r \frac{a-r}{a-r_0}\frac{h}{a\mathrm{b}}\mathrm{d}r = \frac{\pi(h-h_0)}{3r_0\mathrm{b}}(a^2+ar_0-2{r_0}^2). \tag{7.12}$$

The proportion of the saturated volume to the total GND volume can be defined as $n = r_0/a$. According to equation 7.9, $n \approx (h-h_0)/h$. The total dislocation length for the mixed state in the transition regime is therefore calculated:

$$\begin{aligned}\lambda_{\text{trans}} &= \lambda_1 + \lambda_2(r) = \frac{\pi(h-h_0)}{3\mathrm{b}}(r_0 + \frac{a^2}{r_0} + a) = \frac{\pi(h-h_0)a}{3\mathrm{b}}(n+1+\frac{1}{n}) \\ &= \frac{\pi ha}{3\mathrm{b}}(n^2+n+1).\end{aligned} \tag{7.13}$$

The GND density for the mixed state is

$$\rho_{\text{G,trans}} = \frac{1\tan^2\theta}{2\mathrm{b}h}(n^2+n+1) \tag{7.14}$$

with the material characteristic length scale

$$h^*_{\text{trans}} = \frac{27}{2}\mathrm{b}\alpha^2\tan^2\theta(\frac{\mu}{H_0})^2(n^2+n+1) = \frac{1}{3}h^*(n^2+n+1) \tag{7.15}$$

with h^* the same expression in 7.8 from the Nix-Gao model [9]. Unlike the two regimes at large and small depths (Figure 7.4 (c) and (a)), where the slopes and h^* are constant due to the linear relation between H^2 and $1/h$ (equation 7.7), in the transition regime (Figure 7.4(b)), the characteristic length scale $h^*{}_{\text{trans}}$ is no longer constant, but changes gradually because of the increasing ratio of saturated to unsaturated GND volume $n = r_0/a = (h-h_0)/h$.

As a result, the slope in the transition regime equals to ${H_0}^2 \cdot h^*_{\text{trans}}$ and is described as a function of h. Therefore, the model introduced in this section, captures the ISE over the whole depth range after the pop-in. As can be seen in equation 7.15, if r_0 approaches zero, h^*_{trans} gives the same result as in equation 7.7 for the small depth regime. By contrast, when the volume filled the diluted GND distribution is big and r_0 approaches to a, h^*_{trans} approaches the

description of the large depth regime. The behavior of H^2 to $1/h$ can therefore be described quantitatively over the whole depth regime using equations 7.7, 7.8, and 7.15, as shown in Figure 7.5.

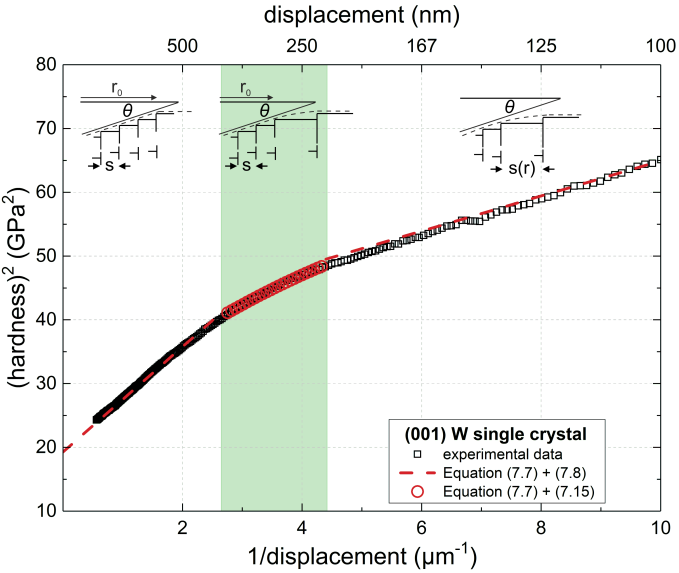

Figure 7.5
Indentation size effect of (001) tungsten single crystal. The average of 20 indents is shown together with the bi-linear model described by equations 7.7 and 7.8. Besides, the transition regime is considered and described by equations 7.7 and 7.15. The transition regime was determined of the depth ranging from 230 nm to 370 nm.

In addition to the data, in Figure 7.5, the corresponding GND model is illustrated for each depth regime. Indicated with the red open circles in Figure 7.5, h_0 is in the range around 300 nm, which is comparable to the transition depth determined by the bi-linear ISE model according to equation 7.7. In the depth range of 230 nm to 370 nm, i.e. $h_0 \pm 70$ nm, the transition regime is well described by equations 7.7 and 7.15.

In the literature, the bi-linear behavior of the ISE of different materials (including single crystalline tungsten) was ascribed to the friction stress, i.e. the Peierls stress or intrinsic lattice resistance [68]. Accordingly, the non-linear ISE was described as a parabolic behavior of H^2 vs. $1/h$ (see equation 34 in [68] or equation A.1 in Appendix A.6). The comparison of this model with the experimental data is shown in Figure 7.6 assuming two varieties of the GND distribution, i.e. the saturated GND distribution (equations A.1 and 7.8) shown as Figure 7.4(c), and the diluted distribution (equations A.1 and 7.6) in Figure 7.4(a). In addition, the friction model (equation A.1) was directly fit to the experimental data in the depth range from 500 nm to 2000 nm.

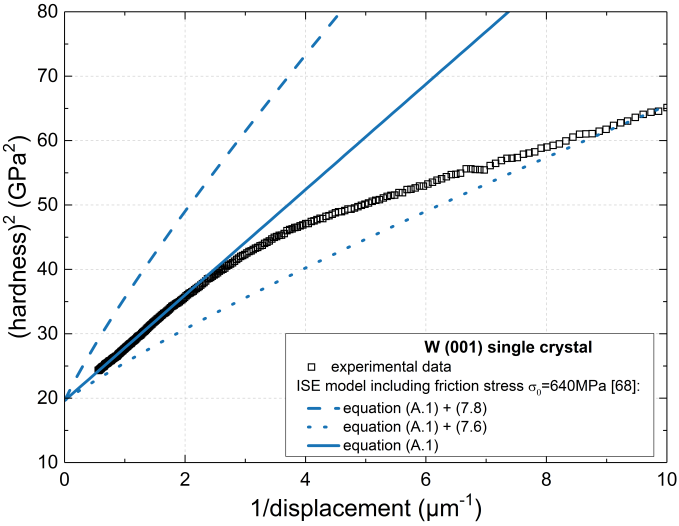

Figure 7.6
Indentation size effect of (001) tungsten single crystal. The average of 20 indents is shown together with the ISE model including Peierls stress σ_0 [68], described by equations A.1 and 7.8 (blue dashed line), equations A.1 and 7.6 in the blue point line, and a direct fit of equation A.1 to the experimental data indicated by the blue solid line. For the three descriptions, σ_0=640 MPa [139] was considered.

In the depth >100 nm, the friction model does not capture the experimental results, which indicates that the friction stress σ_0, although is not negligible in bcc metals, has a limited impact on the non-linear behavior of the ISE. The parabolic behavior according to the friction model does not describe the ISE of single crystalline tungsten properly, even considering different varieties of the GND distribution.

7.2 Strain rate sensitivity of the bi-linear ISE

The bi-linear ISE model has been validated experimentally for constant strain rate testing of single-crystalline tungsten (section 7.1). At the indentation strain rate of 0.05 s^{-1} for a (001) single crystal, the value 0.5 for α was appropriate and the transition of predominant GND mechanisms was observed at the depth h_0 around 300 nm. However, for the (112) orientation, α assumed a value of 0.44, which indicates that α and h_0 might change for different experimental conditions. Thus, a variation of these parameters could be expected since the dislocation mechanism in tungsten is thermally activated and therefore affected by the rate of deformation. In Figure 7.7, the bi-linear ISE model was applied to the experimental data at different strain rates (see also Figure 5.4).

The bi-linear behavior is less pronounced for increasing strain rate. In Figure 7.7, the ISE at the lower strain rates, for instance 0.005 s^{-1} and 0.05 s^{-1} is well described by equation 7.7. The slope of H^2-$1/h$ at the small and large depth regime remains the portion of 1/3, at these strain rates. The transition of the two regimes for 0.005 s^{-1} occurred at larger depth at around 500 nm, compare to 0.05 s^{-1}. The transition becomes less significant for the higher strain rates and it is hard to find a clear h_0 in the 0.5 s^{-1} data. The large depth regime can still be characterized by the standard Nix-Gao model assuming saturated GND density. For smaller depth, the indentation behavior is described by the

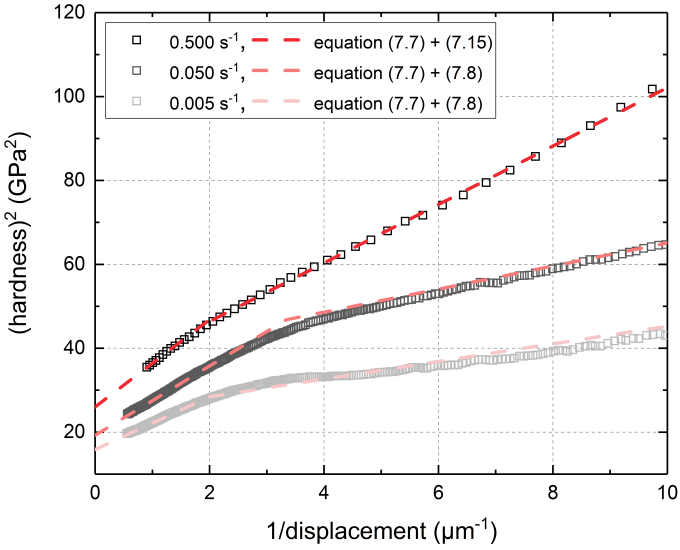

Figure 7.7
Bi-linear ISE at three different strain rates. Average data of 20 indents at each strain rates is shown together with the ISE model in equations 7.7, 7.8, and 7.15.

transition regime of equation 7.15, as shown by the dark red dashed line in the graph.

This behavior is corroborated by microstructural analysis. Band contrast (BC) images of the cross section beneath slow and fast indents at 200 nm depth were compared and are shown together with the 0.05 s^{-1} indent to 500 nm in Figure 7.8. The microstructure at 0.5 s^{-1} is similar to the structure underneath the indent at 0.05 s^{-1}. On both sides of indents in Figure 7.8 (b) and (c), semi-circular dark lines were observed (as marked by arrows in Figure 7.8), which indicate a highly disordered lattice structure likely reflecting the concentration of GNDs or a sub-grain boundary.

As shown in section 6.3, quantitative analysis of averaged GND density along the x direction proved that the difference of GND density between high and low strain rates, i.e. 0.5 s^{-1} and 0.005 s^{-1}, is larger at 200 nm than at 2000 nm

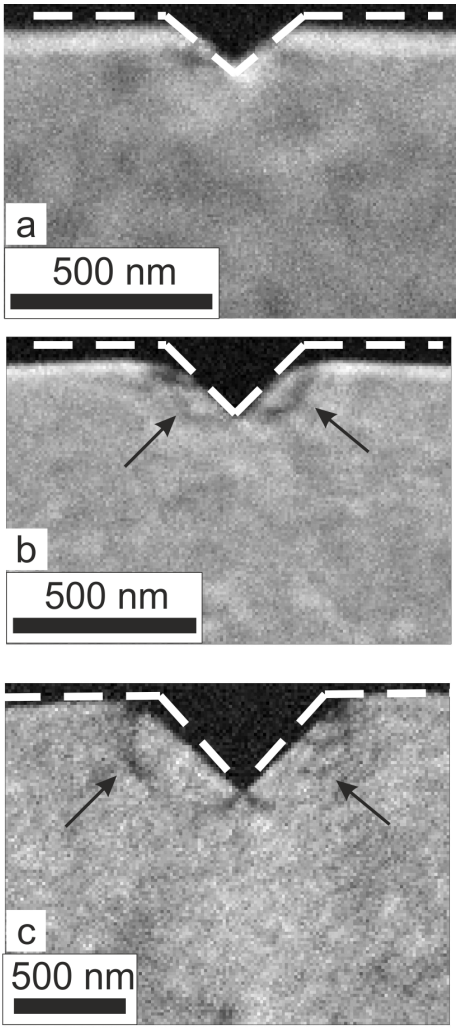

Figure 7.8
Band contrast images of the cross section of indents at different strain rates and depths. (a) 0.005 s^{-1}, 200 nm; (b) 0.5 s^{-1}, 200 nm and (c) 0.05 s^{-1}, 500 nm. Dark lines indicating highly disordered lattice structure are marked by the black arrows.

depth (shown in Figure 6.12). A similar GND structure was observed in the cross section beneath wedge indents at 0.005 s^{-1} and 0.5 s^{-1} at a larger depth, i.e. 2000 nm, while the GND structure at 200 nm exhibited a pronounced difference for these two strain rates (Figure 6.11). The IPF maps of cross sections of wedge indents conducted to 200 nm at two strain rates are presented in Figure 7.9.

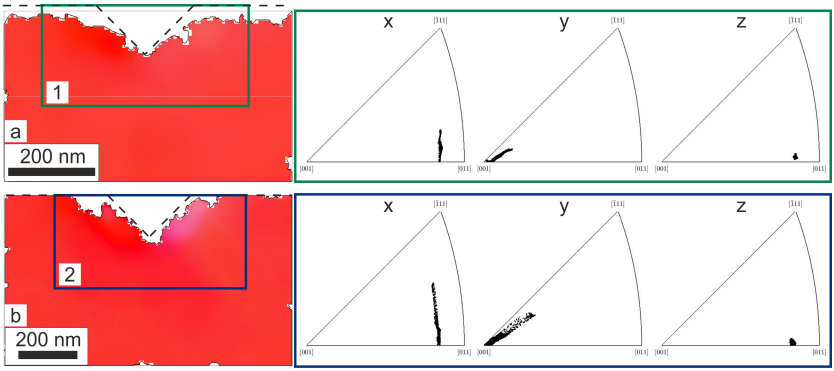

Figure 7.9
IPF maps in *y* direction of slow (a) and fast (b) wedge indents to 200 nm depth. Data in frame 1 (in green) and 2 (in blue) were analyzed and the individual points plotted in IPF.

Only the IPF map of the *y* direction is shown, since both *x* and *y* give similar results. In-plane structural deformation was observed for both strain rates, as indicated by the IPFs showing the rotation in both *x* and *y* directions, while the orientation in the *z* direction remained constant. Unlike indents to 2000 nm, the microstructure at the two strain rates exhibits qualitative differences at the depth of 200 nm. In general, the deformation at the fast strain rate appears more pronounced than at the slower one. For the slower strain rate, the change of orientation appears continuous and no clear subgrain is observed. By contrast, in Figure 7.9(b), deformation appears localized underneath the deformed surface and the formation of a subgrain can be seen, which can be distinguished as faint transition from red to magenta when comparing the undeformed and

deformed regions, respectively. Here, the change of orientation was therefore no longer continuous. Correspondingly, the same phenomenon was noticed in the IPF of frame 2 as well. Nonetheless in Figure 7.9(b), no region of higher GND density was beneath the subgrain as shown in Figure 6.9(c) for a strain rate of 0.05 s^{-1} and depth of 500 nm. It is reasonable to assume that at 0.5 s^{-1} and 200 nm, the indentation induced dislocation structure has developed into an intermediate stage reflecting the transition to lower strain rates. As shown in Figure 6.9(b), at 0.05 s^{-1} and 200 nm no subgrain had yet been generated.

As discussed above, the ISE model presented is based on the assumption of the GND structure. In other words, a dislocation mechanism represents the foundation of the ISE model. Phenomenologically, ISE of single crystalline tungsten can be well rationalized and described quantitatively by the bi-linear model. The earlier occurrence of the subgrains at higher strain rate, though, caused an earlier transition between the two regimes at a smaller depth and resulted in a broadened transition phase. Also, by changing the strain rate, $\alpha = 0.5$ is no longer appropriate but varies with strain rates. In Figure 7.10, the experimentally determined α for (001) tungsten single crystal has been plotted versus indentation strain rate.

With increasing strain rate, the parameter α increases within a range of 0.4 to 0.6. For the strain rate of 0.05 s^{-1}, the fitted α of 0.50, coincided with the literature value [9, 63]. Since α would be influenced by the dislocation structure, the increase of α with increasing strain rate would be expected. Indeed with increasing strain rate, the GND structure needs to adapt and experimentally a clear change was observed, as shown in Figure 6.10; more dislocation systems were activated in the case of 0.5 s^{-1} strain rate compared to 0.005 s^{-1}.

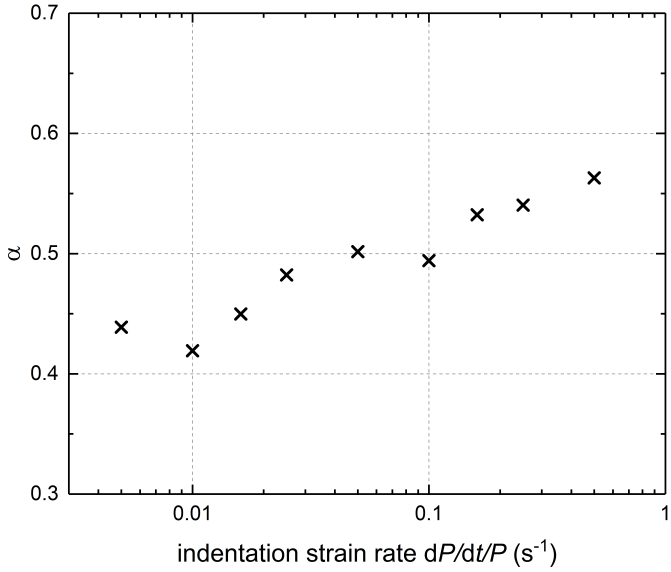

Figure 7.10
α of (001) grain over indentation strain rates from 0.005 s^{-1} to 0.5 s^{-1}. Here *x* axis was plotted in form of logarithm.

7.3 Evaluation of the nanoindentation induced dislocation structure

As described in section 6.1, the series of wedge indentation experiments fulfilling the plane strain condition were conducted. Plane strain deformation is also relevant for the description of crack tip fields [117], and a comparison of the dislocation structures might improve our understanding of the dislocation mechanisms.

As shown in chapter 6, the GND structure exhibits clear differences in the two regimes of smaller and larger depth. Furthermore, the microstructures, such as (sub-) grains and GND distribution, were influenced by the tip geometry. For the series of indents conducted with the 90° wedge at a strain rate of 0.05 s^{-1},

the microstructure evolution is schematically shown in Figure 7.11 (based on the experimental results in Figure 6.9).

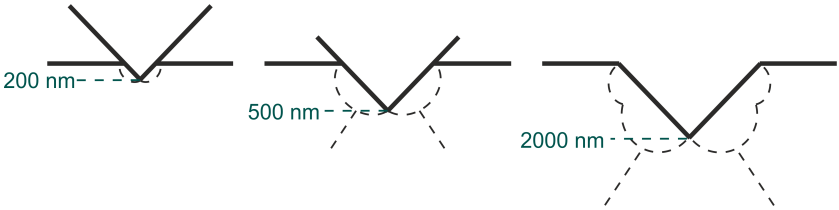

Figure 7.11
Schematic describing the microstructure and GND evolution on the cross section of an indent conducted with the 90° wedge. From left to right, the indentation depth increases. The black dashed lines indicate the positions, where GND concentration were observed. The volume inside the black dashed lines is considered as the GND interaction volume in the following context.

At the very early stage of indentation, while the depth is less than 200 nm (the very left sketch in Figure 7.11), GNDs are generated and concentrate in the vicinity of the tip, while no sub-grains are formed. With increasing depth, GND concentration expands and the GND interaction volume sketched by the dashed lines increases. The material adjacent to this deformation zone also becomes increasingly affected. At the depth of 500 nm, straight lines containing higher GND density are observed. The orientation inside the GND interaction volume changes further and becomes homogeneous gradually, which marks the onset of subgrain formation. For larger depth, the GND interaction volume further increases, while the GND distribution further changes. The straight GND lines grow further into the material at an angle of $\sim 70^\circ$ between the two lines.

The two stages of GND structures can be distinguished by the appearance of the two straight lines of high GND density. The $\sim 70^\circ$ angle was also observed in the lattice rotation maps (Figure 6.2 and 6.3) as well as for different indentation conditions (Figure 6.14).

As discussed by Rice [117], two kinds of crack tip fields occur. While for a growing crack the stress and deformation near the crack tip are supposed to be

fully continuous, both fields near the stationary crack tip exhibit discontinuous changes and the near-tip field can be segmented into angular sectors [117]. Experimentally, the shear sectors were identified by Kysar and Briant using EBSD [140]. Shear and dislocations concentrate along the boundary of these sectors, formed the rays of discontinuity. For fcc materials, the rays are usually parallel to the traces of the activated family of slip planes while for bcc materials, the rays are perpendicular to the activated slip planes [117], as illustrated in Figure 7.12 for a (110) plane of a bcc crystal.

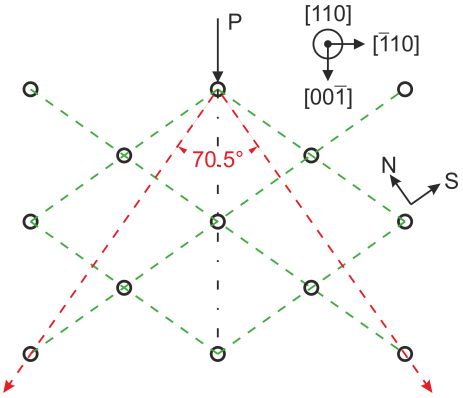

Figure 7.12
Schematic of a (110) crystal plane with atoms denoted by the black circles. When a normal load P is applied along [00$\bar{1}$] direction as indicated by the black arrow and dashed-dotted line, the traces of corresponding {110} slip plane families are highlighted as the green dashed lines. N and S indicate directions normal and parallel to one family of {110} planes. The red dashed lines mark the normal directions to {110} planes with the angle of 70.5° in between.

As described by Rice [117], in bcc materials, the shear concentrated along a ray of kink type, for which a series of dipole dislocations are required expanding along the ray on the slip planes. Thus, the direction of the rays of discontinuity must be normal to the slip planes, as indicated by the red dashed lines in Figure 7.12. Since the cross sections of wedge indents were (110) planes, the possible slip planes to be activated are the {110} families as also indicated by

the GND maps in sections 6.2 to 6.4. Considering the experimental condition, the angle of 70.5° between the two red rays in Figure 7.12 is in perfect agreement with the angle repeatedly discovered in our experiments (Figure 6.9).

Therefore, the GND rays of Figure 6.9 and 7.11 are very likely rays of discontinuity, as described by Rice [117]. The lattice rotation (Figure 6.3) also revealed sectors on the two sides of the rays with the lattice rotation changing discontinuously. The microstructures before and after the appearance of the rays are possibly comparable to the growing crack tip field and the stationary crack tip field, respectively, and with increasing indentation depth, the deformation field near the indent tip changed from continuous to discontinuous.

A comparison of microstructures induced by different wedge angles, i.e. 60° and 90°, is shown in Figure 7.13. Angles of 70.5° were often identified near the indenter tip or in the influenced zone. In addition to the semicircular GND concentrated curves near the indenter tip (marked by the black arrows in Figure 7.13 (a)-(d)), the concentration of GNDs has been found in the region near the sample surface, where the material piled up. A similar configuration can be seen in the GND maps in Figure 6.14. Individual loops can be seen in Figure 7.13 (highlighted by the red arrows and shown at higher magnification in (e) and (f)). Note that the semicircular structures near the tip and the loop structures near the free surface became more isolated when the wedge angle was reduced, as shown in Figure 7.13 (a) and (c).

Such behavior could be related to constraint exerted on the material. For deep indents, if the surface were constrained, more than one independent dislocation source should exist. The GND interaction volume results from all dislocation sources together and is dependent in the indent geometry, i.e. tip angle. A schematic of the formation of the interaction volume considering two dislocation sources under different tip angles is presented in Figure 7.14.

The two regions indicated by red dashed lines near the sample surface and black dashed lines near the indent tip were most likely dominated by different sources. For the sharper wedge, both regions appeared but were clearly located

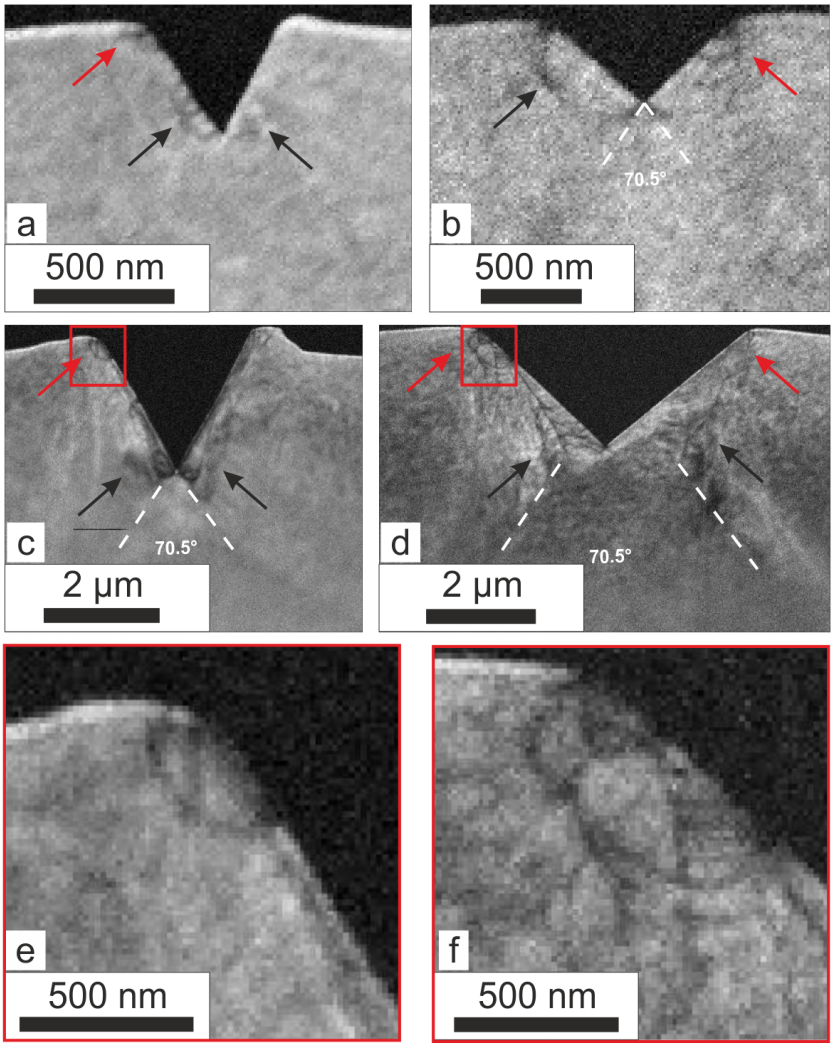

Figure 7.13
BC images of cross sections of indents by wedges with different angles and to different depths. Cross sections of the 60° wedge tip to (a) 500 nm and (c) 2000 nm reveal distinctly different deformation zones. Indents using the 90° wedge to (b) 500 nm and (d) 2000 nm exhibit similar characteristic features. The micrographs in (e) and (f) show the read frames of (c) and (d) at higher magnification.

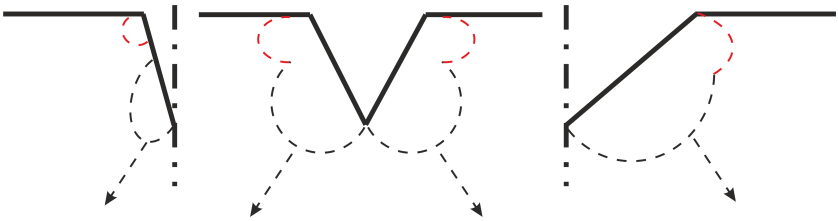

Figure 7.14
Schematic describing the regions related to two dislocation sources and the interaction between the two sources. From left to right, the wedge angle increases, while the regime of two sources overlapped gradually. The arrows represent the 70.5° rays related to the kink-type deformation (Figure 7.12). Here, no material pile-up is assumed occurring on the free surface.

separated without overlap (Figure 6.14 and Figure 7.13). For the larger wedge angle, the two regions overlapped, but the microstructures in the two regions were not identical. Inside the black encircled region near the bottom of the indent (in Figure 7.14), horizontal wave-like traces can be seen in the BC images (in Figure 7.13) and the GND maps (in Figure 6.14). The structures inside the red region (in Figure 7.14) consisted of loops and traces arranged in concentric circles were observed in that region (Figure 7.13).

As discussed by Rester et al. [141] for shallow indents, due to the surface defects such as the fractured oxide layers or pre-existing dislocations, dislocations could be generated preferably from this region then be emitted into the material. The source in the red region, though, is unlikely to be the primary emitting source. Since the region near the bottom of the indent was significantly deformed, more GNDs would be required. When the constraint was reduced as in the case of indenting a thin section of material (section 4.3.1), structures in the red region disappeared, as shown in Figure 6.14. The primary source to facilitate the geometry of the wedge indents should therefore be ascribed to the structures in the black encircled regions.

In Figure 7.15, the deformed structure on the free surface of the indented thin material section is compared to the cross section from the middle of the thin

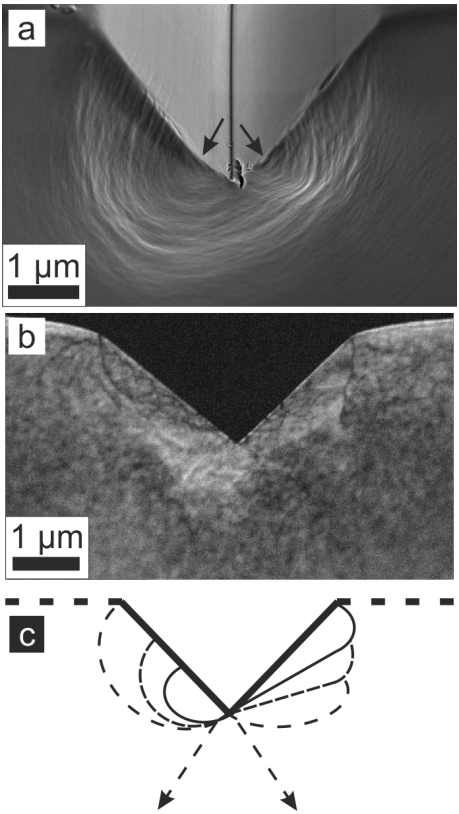

Figure 7.15
(a) SEM image of deformed surface after wedge indentation into a thin section of material. (b) BC image of the indent after thinning the section until its middle was reached. (c) Schematic describing the expansion of the interaction volume without constraint (left hand side) or with constraint considered (right hand side). The black dashed arrows indicate the expansion directions.

section. The thin section indent (Figure 7.15(a)) exhibits a morphology resulting from the least constraint, while the cross section from the middle shows the deformed structure, which had experienced less constraint compared to the regular wedge indents into bulk tungsten, but was still constrained due to the finite thickness of the indented section. In Figure 7.15(a), the slip traces or contour lines are distributed quite symmetrically on the left and right sides of the indent. On both sides, material extrusions can be seen, as marked by the black arrows in Figure 7.15(a). The contour lines close to the black arrows have a greater curvature, while the curvature is reduced for the lines at greater distance. From the center to the outer part, the contour lines became shallower, until they disappeared. Furthermore, several steps can be seen on the edge of the material, matching the slip traces on the side. It is conceivable that the highly deformed regions near the bottom of the indent (marked by the arrows), are the locations of the dislocation sources on the free surface.

By contrast, the microstructure at the center slide appears more complex than the one on the free surface. The BC image in Figure 7.15(b) showed a structure that is very similar to the GND map in Figure 6.14(c). Due to the lateral constraint the deformation (or GNDs) concentrated in the region near the deformed contact surface. Compared to the microstructure underneath the indents on bulk material (Figure 6.14(b)), the profile of the interaction volume has a different shape than the butterfly shape form due to the disappearance of the loop structures close to the surface.

The dislocation source near the sample surface is associated with the material pile-up. It is, however, difficult to distinguish, whether the pile-up causes the concentration of GNDs in that region, or conversely, material piled up due to the concentrated GNDs. According to Figure 7.15 (a) and (b), the following scenario is conceivable: Deformation or GNDs are first generated from the primary sources near the bottom of the indent, from where they expand outwards. If no constraint is exerted, the expansion of the interaction volume is described by the left side of the schematic in Figure 7.15(c), and as observed

in Figure 7.15(a). When the GNDs arrived at the free surface, dislocations escaped and left the steps behind on the surface. Since the surface area was big enough, the dislocations did not accumulate near the surface, and the material did not pile up. When the portion of the free surface was reduced, dislocations could not leave the material and the deformed material was pushed away with increased penetration. The evolution of the interaction volume is described by the right half of the schematic in Figure 7.15(c), which explains the horizontal traces being observed inside the primary-source-governed region in the GND maps of Figure 6.14. Dislocations were able to escape the indented thin section due to the close proximity of the free surfaces and no material pile-up surround the indent was observed.

7.4 Characterizing the kink-pair structure

The strain rate dependent hardness of single crystalline tungsten is attributed to the thermally activated dislocation structure, i.e. the kink-pairs. One kink-pair contains a pair of edge dislocations, which are the kinks, and a screw dislocation line in-between [21, 25]. The volume of this dislocation structure can be calculated according to its geometry [25]:

$$V^* = \mathrm{b} h_{\mathrm{kink}} \lambda^*. \tag{7.16}$$

Here, b is the magnitude of the Burgers vector, h_{kink} and λ^* are the height and critical distance of the two kinks, respectively. In section 5.2.2, the kink-pair-motion related activation volume V^* was determined for both (001) and (112) crystals over the indentation depth ranging from 200 nm to 2000 nm. The results were plotted in Figure 5.9. If the height h_{kink} were determined, the detailed structure of the kink-pair could be resolved.

The height of the kink is the vertical distance between the screw dislocation lines along two neighboring Peierls valleys, which, for a bcc material, is the

distance perpendicular to a $\langle 111 \rangle$ direction on the corresponding slip plane. For single crystalline tungsten at room temperature, the possible slip systems are on the $\{110\}$ and $\{112\}$ planes [43, 142]. Therefore, the two kink heights in the individual systems are:

$$h_{\{110\}} = \frac{2}{3}\sqrt{2}\mathrm{b}, \tag{7.17}$$

$$h_{\{112\}} = \sqrt{3}h_{\{110\}} = \frac{2}{3}\sqrt{6}\mathrm{b} \tag{7.18}$$

respectively [143].

As reported in [43] for single crystalline tungsten at room temperature, there might be an overlap of regime II and regime III according to the kink-pair theory (see section 2.1). For both regimes, the kink-pair structure should be described by the LT (line-tension) model, but the relevant slip planes are $\{112\}$ in regime II and $\{110\}$ in regime III. Additionally, the activation volume V^* would increase from regime III towards regimes II and I. Keeping this in mind and looking at Figure 5.9, the activation volume V^* of (001) and (112) single crystals increased with increasing depth, which should be related to the development of a kink-pair structure. The activation volume then reached a plateau, i.e. 5.38 b^3 for (001) and 4.27 b^3 for (112), at the larger indentation depths. Consequently, the different magnitudes of the activation volume for the same material but two different crystal orientations can be ascribed to the activation of two slip systems, along which the kink-pair could move. Based on the experimental results of this work, the possible kink-pair slip planes for the (001) crystal would be $\{112\}$ and for the (112) crystal $\{110\}$.

Furthermore, according to the kink theory [21, 25], the kink width λ^* is described as:

$$\lambda^* = \left(\frac{\mu \mathrm{b} h_{\mathrm{kink}}}{8\pi\sigma}\right)^{1/2}. \tag{7.19}$$

Here, μ is the shear modulus and σ is the applied stress.

As a typical bcc metal, the Peierls stress σ_P of single crystalline tungsten can be fairly large. Even though it has been shown that the Peierls stress is not responsible for the bi-linear ISE of this material (section 7.1), it is still a notable component contributing to the hardness. The depth-independent indentation hardness H_0 should be [68, 143]:

$$H_0 = 3\sigma_P + 3\sigma. \tag{7.20}$$

The Peierls stress can be calculated as follows:

$$\sigma_P = \frac{1}{3}H_0 - \sigma. \tag{7.21}$$

Assuming the H_0 value at a strain rate of 0.05 s^{-1} from Figure 5.8(a) for the two crystal orientations, which is the median strain rate of the corresponding CSR experiments used to determine the activation volume V^*, the Peierls stress for different regimes, i.e. regime II and regime III, can be determined. Computed values according to equations (7.16) to (7.21) are summarized in Table 7.1. According to Brunner [43], the kink height $h_{\{112\}}$ for regime I and regime II is very close to the theoretical value. However, the experimentally determined $h_{\{110\}}$ for regime III was approximately 20% larger than the theoretical value. The calculation using Brunner's experimental determined $h_{\{110\}}$ [43] is also listed in Table 7.1.

In general, the magnitude of the values in Table 7.1 is in reasonable agreement with the literature [43, 68, 139]. The Peierls stress calculated for the (001) crystal in regime II show almost perfect agreement with the estimation of 640 MPa of Meieran and Thomas [139], while the σ_P determined for the (112) crystal is close to Brunner's result for regime III, i.e. 982 MPa [43]. However, determining the kink parameters of regimes II and III are expected to only yield on estimate, since the applicable LT model does not refer for a fully developed

Table 7.1
Hardness H_0 at 0.05 s^{-1}, kink width λ^*, applied stress σ, and Peierls stress σ_P for (001) and (112) oriented tungsten single crystals. Results calculated using Brunner's parameter [43] were added in brackets. Burgers vector b and shear modulus μ were assumed as 0.27353 nm and 151.99 GPa, respectively.

crystal orientation	H_0 **[GPa]**	λ^* **[b]**	σ **[MPa]**	σ_P **[MPa]**
(001)	4.63	3.3	909.8	633.5
(112)	4.42	4.5 (3.7)	278.0 (505.8)	1197.7 (967.6)

kink-pair, but rather to a bulge shape [21, 44, 54]. The calculation of the kink-pair parameters, though, is based on two well-separated, fully formed kinks. Despite this limitation, nanoindentation can be used to obtain quantitative estimations describing the dislocation structure of bcc crystals.

As described in chapters 5 to 7, the mechanical behavior of single crystalline tungsten, and the corresponding dislocation structure and density were analyzed, with the mechanisms quantitatively characterized. Specifically, hardness determined by nanoindentation reflects a change of the dislocation distribution at different depth regimes, which was sufficiently described by a bi-linear ISE model. The different dislocation distributions were further captured beneath the shallow and deep indents under the plane strain condition, and the indent fields can be comparable to the crack tip fields. The nanoindentation data also reveal the depth and crystal orientation dependence of the activation volume, and indicate the formation and growth of the kink-pair structure.

8 Summary

Nanoindentation experiments were conducted on the (001) and (112) tungsten single crystals under the different experimental conditions. Both orientations reveal a significant bi-linear ISE at different indentation strain rates, that the H^2 vs. $1/h$ exhibits different linear behaviors in the small and large depth regimes. Around the depth of 300 nm, the transition of the two depth regimes was observed. The bi-linear behavior of single-crystalline tungsten cannot be described by the classic Nix-Gao model [9]. In the small depth regime, the Nix-Gao model overestimates the hardness values.

Based on the same framework of [9], an adapted bi-linear ISE model was introduced by reevaluating the two fundamental assumptions in the Nix-Gao model [9]. The GND distribution underneath the indent needs to be rearranged and diluted, to adapt the deformation in the small depth regime.

This adapted bi-linear ISE model was validated by the hardness data of both crystals at nine strain rates ranging from 0.005 s^{-1} to 0.5 s^{-1}. Also, the characterization of the GND structures underneath the indents to different depths was conducted using the TKD measurement. Different GND density distributions were observed in the small and large depth regimes at different strain rates. Furthermore, as the plane-strain deformation was achieved in the experiments, the dislocation structures in the indent fields of this specific deformation condition were able to be captured and are comparable to the prediction for the crack tip field, according to Rice [117].

The dislocation activities of the single-crystalline tungsten were further studied by varying the loading velocity. Activation volumes reflecting the dislocation

nucleation, i.e. V_y^*, and motion, i.e. V^*, were determined from the pop-ins of the CLR tests and hardness values of the CSR tests, respectively. At room temperature, the dislocation nucleation related parameters, i.e. τ_{max} and V_y^*, do not reveal a loading rate dependence. By contrast, the two single crystals exhibit a significant strain rate sensitivity of the hardness, and their V^* increase with increasing indentation depth, until a plateau value of V^* for each crystal was reached. The two plateau values of the (001) and (112) orientations indicate the different kink-pair structures in two regimes referring to the respective slip systems. The configuration of the kink-pairs for the two slip systems can be therefore estimated, and the corresponding Peierls stress of the {110} and {112} planes determined, consequently.

Bibliography

[1] V. Steinbach and F.-W. Wellmer, "Consumption and use of non-renewable mineral and energy raw materials from an economic geology point of view," *Sustainability*, vol. 2, no. 5, pp. 1408–1430, 2010.

[2] J. R. Stephens, "Review of deformation behavior of tungsten at temperature less than 0.2 absolute melting temperature," 1972. [Online, retrieved on 2020.11.23]. Available: https://ntrs.nasa.gov/api/citations/19720006900/downloads/19720006900.pdf

[3] P. Gumbsch, J. Riedle, A. Hartmaier, and H. F. Fischmeister, "Controlling factors for the brittle-to-ductile transition in tungsten single crystals," *Science*, vol. 282, no. 5392, pp. 1293–1295, 1998.

[4] P. Gumbsch, "Brittle fracture and the brittle-to-ductile transition of tungsten," *Journal of Nuclear Materials*, vol. 323, no. 2-3, pp. 304–312, 2003.

[5] D. Rupp, *Bruch und Spröd-duktil-Übergang in polykristallinem Wolfram: Einfluss von Mikrostruktur und Lastrate*. Karlsruhe: Shaker, 2010.

[6] O. Kraft, P. A. Gruber, R. Mönig, and D. Weygand, "Plasticity in confined dimensions," *Annual Review of Materials Research*, vol. 40, pp. 293–317, 2010.

[7] W. C. Oliver and G. M. Pharr, “An improved technique for determining hardness and elastic modulus using load and displacement sensing indentation experiments,” *Journal of Materials Research*, vol. 7, no. 6, pp. 1564–1583, 1992.

[8] M. R. VanLandingham, “Review of instrumented indentation,” *Journal of Research of the National Institute of Standards and Technology*, vol. 108, no. 4, p. 249, 2003.

[9] W. D. Nix and H. Gao, “Indentation size effects in crystalline materials: a law for strain gradient plasticity,” *Journal of the Mechanics and Physics of Solids*, vol. 46, no. 3, pp. 411–425, 1998.

[10] G. M. Pharr, E. G. Herbert, and Y. Gao, “The indentation size effect: a critical examination of experimental observations and mechanistic interpretations,” *Annual Review of Materials Research*, vol. 40, pp. 271–292, 2010.

[11] N. Fleck, G. Muller, M. F. Ashby, and J. W. Hutchinson, “Strain gradient plasticity: theory and experiment,” *Acta Metallurgica et Materialia*, vol. 42, no. 2, pp. 475–487, 1994.

[12] J. Hutchinson and N. Fleck, “Strain gradient plasticity,” *Advances in Applied Mechanics*, vol. 33, pp. 295–361, 1997.

[13] A. A. Gazder, K. I. Elkhodary, M. J. Nancarrow, and A. A. Saleh, “Transmission Kikuchi diffraction versus electron back-scattering diffraction: A case study on an electron transparent cross-section of twip steel,” *Micron*, vol. 103, pp. 53–63, 2017.

[14] P. J. Konijnenberg, S. Zaefferer, and D. Raabe, “Assessment of geometrically necessary dislocation levels derived by 3D EBSD,” *Acta Materialia*, vol. 99, pp. 402–414, 2015.

[15] W. D. Klopp, “A review of chromium, molybdenum, and tungsten alloys,” *Journal of the Less Common Metals*, vol. 42, no. 3, pp. 261–278, 1975.

[16] N. J. V. Schmitt, “Experimentelle Untersuchung des Verformungs- und Bruchverhaltens von ein-, bi- und polykristallinem Wolfram auf der Mikroskala,” Karlsruhe, [2016]. [Online, retrieved on 2020.11.23]. Available: http://dx.doi.org/10.5445/IR/1000062471;http://nbn-resolving.de/urn:nbn:de:swb:90-624716;http://d-nb.info/1120498414/34;http://digbib.ubka.uni-karlsruhe.de/volltexte/1000062471

[17] J. Ast, *Untersuchung der lokalen Bruchzähigkeit und des elastisch-plastischen Bruchverhaltens von NiAl und Wolfram mittels Mikrobiegebalkenversuchen*. Erlangen: FAU University Press, 2016.

[18] J. Ast, M. Göken, and K. Durst, “Size-dependent fracture toughness of tungsten,” *Acta Materialia*, vol. 138, pp. 198–211, 2017.

[19] J. Ast, J. Schwiedrzik, J. Wehrs, D. Frey, M. N. Polyakov, J. Michler, and X. Maeder, “The brittle-ductile transition of tungsten single crystals at the micro-scale,” *Materials & Design*, vol. 152, pp. 168–180, 2018.

[20] X. Li and B. Bhushan, “A review of nanoindentation continuous stiffness measurement technique and its applications,” *Materials Characterization*, vol. 48, no. 1, pp. 11–36, 2002.

[21] J. Hirth and J. Lothe, “Theory of dislocations, 1982” New York: Wiley, 1982.

[22] A. Schneider, C. Frick, B. Clark, P. Gruber, and E. Arzt, “Influence of orientation on the size effect in BCC pillars with different critical temperatures,” *Materials Science and Engineering: A*, vol. 528, no. 3, pp. 1540–1547, 2011.

[23] I.-C. Choi, Y.-J. Kim, B. Ahn, M. Kawasaki, T. G. Langdon, and J.-I. Jang, "Evolution of plasticity, strain-rate sensitivity and the underlying deformation mechanism in Zn–22% Al during high-pressure torsion," *Scripta Materialia*, vol. 75, pp. 102–105, 2014.

[24] C. Schuh, J. Mason, and A. Lund, "Quantitative insight into dislocation nucleation from high-temperature nanoindentation experiments," *Nature Materials*, vol. 4, no. 8, pp. 617–621, 2005.

[25] A. Seeger and P. Schiller, "Bildung und Diffusion von Kinken als Grundprozess der Versetzungsbewegung bei der Messung der inneren Reibung," *Acta Metallurgica*, vol. 10, no. 4, pp. 348–357, 1962.

[26] K. J. Van Vliet, J. Li, T. Zhu, S. Yip, and S. Suresh, "Quantifying the early stages of plasticity through nanoscale experiments and simulations," *Physical Review B*, vol. 67, no. 10, p. 104105, 2003.

[27] J. Li, K. J. Van Vliet, T. Zhu, S. Yip, and S. Suresh, "Atomistic mechanisms governing elastic limit and incipient plasticity in crystals," *Nature*, vol. 418, no. 6895, pp. 307–310, 2002.

[28] C. L. Kelchner, S. Plimpton, and J. Hamilton, "Dislocation nucleation and defect structure during surface indentation," *Physical Review B*, vol. 58, no. 17, p. 11085, 1998.

[29] J. Mason, A. Lund, and C. Schuh, "Determining the activation energy and volume for the onset of plasticity during nanoindentation," *Physical Review B*, vol. 73, no. 5, p. 054102, 2006.

[30] I.-C. Choi, D.-H. Lee, B. Ahn, K. Durst, M. Kawasaki, T. G. Langdon, and J.-I. Jang, "Enhancement of strain-rate sensitivity and shear yield strength of a magnesium alloy processed by high-pressure torsion," *Scripta Materialia*, vol. 94, pp. 44–47, 2015.

[31] L. Wang, H. Bei, T. Li, Y. Gao, E. P. George, and T. Nieh, "Determining the activation energies and slip systems for dislocation nucleation in body-centered cubic Mo and face-centered cubic Ni single crystals," *Scripta Materialia*, vol. 65, no. 3, pp. 179–182, 2011.

[32] F. Seitz, "On the formation of dislocations from vacancies," *Physical Review*, vol. 79, no. 5, p. 890, 1950.

[33] T. F. Page, W. C. Oliver, and C. J. McHargue, "The deformation behavior of ceramic crystals subjected to very low load (nano) indentations," *Journal of Materials Research*, vol. 7, no. 2, pp. 450–473, 1992.

[34] C. A. Schuh and A. C. Lund, "Application of nucleation theory to the rate dependence of incipient plasticity during nanoindentation," *Journal of Materials Research*, vol. 19, no. 7, pp. 2152–2158, 2004.

[35] K. L. Johnson and K. L. Johnson, *Contact mechanics*. Cambridge, United Kingdom: Cambridge University Press, 1987.

[36] D. F. Bahr, D. Kramer, and W. Gerberich, "Non-linear deformation mechanisms during nanoindentation," *Acta Materialia*, vol. 46, no. 10, pp. 3605–3617, 1998.

[37] R. Honeycombe, "The plastic deformation of metals, 1984," London: *Edward Arnold, London. JAERO290© IMechE*, p. 358, 2008.

[38] G. I. Taylor, "The mechanism of plastic deformation of crystals. part I.–theoretical," *Proceedings of the Royal Society of London. Series A, Containing Papers of a Mathematical and Physical Character*, vol. 145, no. 855, pp. 362–387, 1934.

[39] A. Schneider, B. Clark, C. Frick, P. Gruber, and E. Arzt, "Effect of orientation and loading rate on compression behavior of small-scale Mo pillars," *Materials Science and Engineering: A*, vol. 508, no. 1-2, pp. 241–246, 2009.

[40] V. Maier, K. Durst, J. Mueller, B. Backes, H. W. Höppel, and M. Göken, "Nanoindentation strain-rate jump tests for determining the local strain-rate sensitivity in nanocrystalline Ni and ultrafine-grained Al," *Journal of Materials Research*, vol. 26, no. 11, pp. 1421–1430, 2011.

[41] V. Maier, C. Schunk, M. Göken, and K. Durst, "Microstructure-dependent deformation behaviour of BCC-metals–indentation size effect and strain rate sensitivity," *Philosophical Magazine*, vol. 95, no. 16-18, pp. 1766–1779, 2015.

[42] J. Rösler, H. Harders, and M. Bäker, *Mechanisches Verhalten der Werkstoffe*. Wiesbaden: Springer-Verlag, 2012.

[43] D. Brunner, "Comparison of flow-stress measurements on high-purity tungsten single crystals with the kink-pair theory," *Materials Transactions, JIM*, vol. 41, no. 1, pp. 152–160, 2000.

[44] K. Srivastava, "Atomistically-informed discrete dislocation dynamics modeling of plastic flow in body-centered cubic metals," Ph.D. dissertation, Karlsruhe, 2014, Karlsruhe, Karlsruher Institut für Technologie (KIT), Diss., 2014IMD-Felder maschinell generiert (GBV). [Online, retrieved on 2020.11.23]. Available: http://digbib.ubka.uni-karlsruhe.de/volltexte/1000042367;http://d-nb.info/1054989516/34;http://nbn-resolving.de/urn:nbn:de:swb:90-423672

[45] W. Bollmann, "Partial dislocations," in *Crystal Defects and Crystalline Interfaces*. Heidelberg: Springer, 1970, pp. 78–97.

[46] F. Minami, E. Kuramoto, and S. Takeuchi, "Motion of screw dislocations under stress in a model BCC lattice," *physica status solidi (a)*, vol. 12, no. 2, pp. 581–588, 1972.

[47] F. Minami, E. Kuramoto, and S. Takeuchi, "Computer simulation of motion of screw dislocation in model BCC lattices. I. Effect of inter-atom-row potential on Peierls stress," *physica status solidi (a)*, vol. 22, no. 1, pp. 81–88, 1974.

[48] E. Kuramoto, F. Minami, and S. Takeuchi, "Computer simulation of motion of screw dislocation in model BCC lattices. II. Orientation dependence of slip," *physica status solidi (a)*, vol. 22, no. 2, pp. 411–419, 1974.

[49] M. a.-S. Duesbery and V. Vitek, "Plastic anisotropy in BCC transition metals," *Acta Materialia*, vol. 46, no. 5, pp. 1481–1492, 1998.

[50] K. Ito and V. Vitek, "Atomistic study of non-Schmid effects in the plastic yielding of BCC metals," *Philosophical Magazine A*, vol. 81, no. 5, pp. 1387–1407, 2001.

[51] M. Mrovec, R. Gröger, A. G. Bailey, D. Nguyen-Manh, C. Elsässer, and V. Vitek, "Bond-order potential for simulations of extended defects in tungsten," *Physical Review B*, vol. 75, no. 10, p. 104119, 2007.

[52] R. Gröger, A. Bailey, and V. Vitek, "Multiscale modeling of plastic deformation of molybdenum and tungsten: I. Atomistic studies of the core structure and glide of 1/2< 1 1 1> screw dislocations at 0 K," *Acta Materialia*, vol. 56, no. 19, pp. 5401–5411, 2008.

[53] R. Gröger, V. Racherla, J. Bassani, and V. Vitek, "Multiscale modeling of plastic deformation of molybdenum and tungsten: II. Yield criterion for single crystals based on atomistic studies of glide of 1/2< 111> screw dislocations," *Acta Materialia*, vol. 56, no. 19, pp. 5412–5425, 2008.

[54] R. Gröger and V. Vitek, "Multiscale modeling of plastic deformation of molybdenum and tungsten. III. Effects of temperature and plastic strain rate," *Acta Materialia*, vol. 56, no. 19, pp. 5426–5439, 2008.

[55] R. Gröger and V. Vitek, "Directional versus central-force bonding in studies of the structure and glide of 1/2< 111> screw dislocations in BCC transition metals," *Philosophical Magazine*, vol. 89, no. 34-36, pp. 3163–3178, 2009.

[56] Q. Ma and D. R. Clarke, "Size dependent hardness of silver single crystals," *Journal of Materials Research*, vol. 10, no. 4, pp. 853–863, 1995.

[57] K. McElhaney, J. J. Vlassak, and W. D. Nix, "Determination of indenter tip geometry and indentation contact area for depth-sensing indentation experiments," *Journal of Materials Research*, vol. 13, no. 5, pp. 1300–1306, 1998.

[58] Y. Liu and A. W. Ngan, "Depth dependence of hardness in copper single crystals measured by nanoindentation," *Scripta Materialia*, vol. 44, no. 2, pp. 237–241, 2001.

[59] J. Swadener, E. George, and G. Pharr, "The correlation of the indentation size effect measured with indenters of various shapes," *Journal of the Mechanics and Physics of Solids*, vol. 50, no. 4, pp. 681–694, 2002.

[60] G. Feng and W. D. Nix, "Indentation size effect in MgO," *Scripta Materialia*, vol. 51, no. 6, pp. 599–603, 2004.

[61] N. Stelmashenko, M. Walls, L. Brown, and Y. V. Milman, "Microindentations on W and Mo oriented single crystals: an STM study," *Acta Metallurgica et Materialia*, vol. 41, no. 10, pp. 2855–2865, 1993.

[62] K. Durst, B. Backes, and M. Göken, "Indentation size effect in metallic materials: Correcting for the size of the plastic zone," *Scripta Materialia*, vol. 52, no. 11, pp. 1093–1097, 2005.

[63] K. Durst, B. Backes, O. Franke, and M. Göken, "Indentation size effect in metallic materials: Modeling strength from pop-in to macroscopic

hardness using geometrically necessary dislocations," *Acta Materialia*, vol. 54, no. 9, pp. 2547–2555, 2006.

[64] K. Durst, O. Franke, A. Böhner, and M. Göken, "Indentation size effect in Ni–Fe solid solutions," *Acta Materialia*, vol. 55, no. 20, pp. 6825–6833, 2007.

[65] K. Durst, M. Göken, and G. M. Pharr, "Indentation size effect in spherical and pyramidal indentations," *Journal of Physics D: Applied Physics*, vol. 41, no. 7, p. 074005, 2008.

[66] B. Backes, Y. Huang, M. Göken, and K. Durst, "The correlation between the internal material length scale and the microstructure in nanoindentation experiments and simulations using the conventional mechanism-based strain gradient plasticity theory," *journal of Materials Research*, vol. 24, no. 3, pp. 1197–1207, 2009.

[67] Y. Huang, F. Zhang, K. Hwang, W. Nix, G. Pharr, and G. Feng, "A model of size effects in nano-indentation," *Journal of the Mechanics and Physics of Solids*, vol. 54, no. 8, pp. 1668–1686, 2006.

[68] X. Qiu, Y. Huang, W. Nix, K. Hwang, and H. Gao, "Effect of intrinsic lattice resistance in strain gradient plasticity," *Acta Materialia*, vol. 49, no. 19, pp. 3949–3958, 2001.

[69] D. E. Stegall, M. A. Mamun, B. Crawford, and A. Elmustafa, "Indentation size effect in FCC metals: An examination of experimental techniques and the bilinear behavior," *Journal of Materials Research*, vol. 27, no. 12, p. 1543, 2012.

[70] G. M. Pharr, J. H. Strader, and W. Oliver, "Critical issues in making small-depth mechanical property measurements by nanoindentation with continuous stiffness measurement," *Journal of Materials Research*, vol. 24, no. 3, pp. 653–666, 2009.

[71] B. Merle, V. Maier-Kiener, and G. M. Pharr, "Influence of modulus-to-hardness ratio and harmonic parameters on continuous stiffness measurement during nanoindentation," *Acta Materialia*, vol. 134, pp. 167–176, 2017.

[72] G. Beltz, J. Rice, C. Shih, and L. Xia, "A self-consistent model for cleavage in the presence of plastic flow," *Acta Materialia*, vol. 44, no. 10, pp. 3943–3954, 1996.

[73] D. Kiener, C. Motz, T. Schöberl, M. Jenko, and G. Dehm, "Determination of mechanical properties of copper at the micron scale," *Advanced Engineering Materials*, vol. 8, no. 11, pp. 1119–1125, 2006.

[74] M. Rester, C. Motz, and R. Pippan, "The deformation-induced zone below large and shallow nanoindentations: A comparative study using EBSD and TEM," *Philosophical Magazine Letters*, vol. 88, no. 12, pp. 879–887, 2008.

[75] M. Rester, C. Motz, and R. Pippan, "Indentation across size scales–a survey of indentation-induced plastic zones in copper {1 1 1} single crystals," *Scripta Materialia*, vol. 59, no. 7, pp. 742–745, 2008.

[76] M. Rester, C. Motz, and R. Pippan, "Where are the geometrically necessary dislocations accommodating small imprints?" *Journal of Materials Research*, vol. 24, no. 3, pp. 647–651, 2009.

[77] Z. L. Wang, "New developments in transmission electron microscopy for nanotechnology," *Advanced Materials*, vol. 15, no. 18, pp. 1497–1514, 2003.

[78] J. Ahmed, A. Wilkinson, and S. Roberts, "Study of dislocation structures near fatigue cracks using electron channelling contrast imaging technique (ECCI)," *Journal of Microscopy*, vol. 195, no. 3, pp. 197–203, 1999.

[79] S. Zaefferer, “Electron channelling contrast imaging (ECCI): An amazing tool for observations of crystal lattice defects in bulk samples,” *Microscopy and Microanalysis*, vol. 23, no. S1, pp. 566–567, 2017.

[80] I. Gutierrez-Urrutia, S. Zaefferer, and D. Raabe, “Coupling of electron channeling with EBSD: toward the quantitative characterization of deformation structures in the SEM,” *JOM*, vol. 65, no. 9, pp. 1229–1236, 2013.

[81] S. Zaefferer, S. Kleindiek, K. Schock, and B. Volbert, “Combined application of EBSD and ECCI using a versatile 5-axes goniometer in an SEM,” *Microscopy and Microanalysis*, vol. 19, no. S2, pp. 1306–1307, 2013.

[82] J.-l. Zhang, S. Zaefferer, and D. Raabe, “A study on the geometry of dislocation patterns in the surrounding of nanoindents in a TWIP steel using electron channeling contrast imaging and discrete dislocation dynamics simulations,” *Materials Science and Engineering: A*, vol. 636, pp. 231–242, 2015.

[83] N. Anderson and I. Dawson, “The study of crystal growth with the electron microscope III. growth-step patterns and the relationship of growth-step height to molecular structure in n-nonatriacontane and in stearic acid,” *Proceedings of the Royal Society of London. Series A. Mathematical and Physical Sciences*, vol. 218, no. 1133, pp. 255–268, 1953.

[84] A. Forty and F. C. Frank, “Growth and slip patterns on the surfaces of crystals of silver,” *Proceedings of the Royal Society of London. Series A. Mathematical and Physical Sciences*, vol. 217, no. 1129, pp. 262–270, 1953.

[85] P. Sadrabadi, K. Durst, and M. Göken, “Study on the indentation size effect in CaF2: Dislocation structure and hardness,” *Acta Materialia*, vol. 57, no. 4, pp. 1281–1289, 2009.

[86] F. Javaid, E. Bruder, and K. Durst, “Indentation size effect and dislocation structure evolution in (001) oriented SrTiO3 berkovich indentations: HR-EBSD and etch-pit analysis,” *Acta Materialia*, vol. 139, pp. 1–10, 2017.

[87] F. Javaid, A. Stukowski, and K. Durst, “3D dislocation structure evolution in strontium titanate: Spherical indentation experiments and MD simulations,” *Journal of the American Ceramic Society*, vol. 100, no. 3, pp. 1134–1145, 2017.

[88] C. Motz, T. Schöberl, and R. Pippan, “Mechanical properties of micro-sized copper bending beams machined by the focused ion beam technique,” *Acta Materialia*, vol. 53, no. 15, pp. 4269–4279, 2005.

[89] A. J. Wilkinson and D. Randman, “Determination of elastic strain fields and geometrically necessary dislocation distributions near nanoindents using electron back scatter diffraction,” *Philosophical Magazine*, vol. 90, no. 9, pp. 1159–1177, 2010.

[90] D. Dingley, “Progressive steps in the development of electron backscatter diffraction and orientation imaging microscopy,” *Journal of Microscopy*, vol. 213, no. 3, pp. 214–224, 2004.

[91] A. J. Wilkinson and T. B. Britton, “Strains, planes, and EBSD in materials science,” *Materials Today*, vol. 15, no. 9, pp. 366–376, 2012.

[92] T. Britton, J. Jiang, Y. Guo, A. Vilalta-Clemente, D. Wallis, L. N. Hansen, A. Winkelmann, and A. Wilkinson, “Tutorial: Crystal orientations and EBSD – or which way is up?” *Materials Characterization*, vol. 117, pp. 113–126, 2016.

[93] G. Nayyeri, W. J. Poole, C. W. Sinclair, S. Zaefferer, P. J. Konijnenberg, and C. Zambaldi, “An instrumented spherical indentation study on high purity magnesium loaded nearly parallel to the c-axis,” *Materials Science and Engineering: A*, vol. 670, pp. 132–145, 2016.

[94] G. Stechmann, S. Zaefferer, P. Konijnenberg, D. Raabe, C. Gretener, L. Kranz, J. Perrenoud, S. Buecheler, and A. N. Tiwari, "3-dimensional microstructural characterization of CdTe absorber layers from CdTe/CdS thin film solar cells," *Solar Energy Materials and Solar Cells*, vol. 151, pp. 66–80, 2016.

[95] J. Konrad, S. Zaefferer, and D. Raabe, "Investigation of orientation gradients around a hard laves particle in a warm-rolled Fe3Al-based alloy using a 3D EBSD-FIB technique," *Acta Materialia*, vol. 54, no. 5, pp. 1369–1380, 2006.

[96] N. Zaafarani, D. Raabe, R. N. Singh, F. Roters, and S. Zaefferer, "Three-dimensional investigation of the texture and microstructure below a nanoindent in a Cu single crystal using 3D EBSD and crystal plasticity finite element simulations," *Acta Materialia*, vol. 54, no. 7, pp. 1863–1876, 2006.

[97] M. Calcagnotto, D. Ponge, E. Demir, and D. Raabe, "Orientation gradients and geometrically necessary dislocations in ultrafine grained dual-phase steels studied by 2D and 3D EBSD," *Materials Science and Engineering: A*, vol. 527, no. 10-11, pp. 2738–2746, 2010.

[98] W. Pantleon, "Resolving the geometrically necessary dislocation content by conventional electron backscattering diffraction," *Scripta Materialia*, vol. 58, no. 11, pp. 994–997, 2008.

[99] D. Wallis, L. N. Hansen, T. B. Britton, and A. J. Wilkinson, "Geometrically necessary dislocation densities in olivine obtained using high-angular resolution electron backscatter diffraction," *Ultramicroscopy*, vol. 168, pp. 34–45, 2016.

[100] J. Kysar, Y. Saito, M. Oztop, D. Lee, and W. Huh, "Experimental lower bounds on geometrically necessary dislocation density," *International Journal of Plasticity*, vol. 26, no. 8, pp. 1097–1123, 2010.

[101] C. Dahlberg, Y. Saito, M. S. Öztop, and J. W. Kysar, "Geometrically necessary dislocation density measurements associated with different angles of indentations," *International Journal of Plasticity*, vol. 54, pp. 81–95, 2014.

[102] T. Ruggles, D. Fullwood, and J. Kysar, "Resolving geometrically necessary dislocation density onto individual dislocation types using EBSD-based continuum dislocation microscopy," *International Journal of Plasticity*, vol. 76, pp. 231–243, 2016.

[103] T. Ruggles, T. Rampton, A. Khosravani, and D. Fullwood, "The effect of length scale on the determination of geometrically necessary dislocations via EBSD continuum dislocation microscopy," *Ultramicroscopy*, vol. 164, pp. 1–10, 2016.

[104] S. Nishikawa and S. Kikuchi, "Diffraction of cathode rays by mica," *Nature*, vol. 121, no. 3061, pp. 1019–1020, 1928.

[105] S. Zaefferer, "A critical review of orientation microscopy in SEM and TEM," *Crystal Research and Technology*, vol. 46, no. 6, pp. 607–628, 2011.

[106] R. R. Keller and R. H. Geiss, "Transmission EBSD from 10 nm domains in a scanning electron microscope," *Journal of Microscopy*, vol. 245, no. 3, pp. 245–251, 2012.

[107] G. C. Sneddon, P. W. Trimby, and J. M. Cairney, "Transmission Kikuchi diffraction in a scanning electron microscope: A review," *Materials Science and Engineering: R: Reports*, vol. 110, pp. 1–12, 2016.

[108] T. Tokarski, G. Cios, A. Kula, and P. Bała, "High quality transmission Kikuchi diffraction analysis of deformed alloys-case study," *Materials Characterization*, vol. 121, pp. 231–236, 2016.

[109] D. Hull and D. J. Bacon, *Introduction to dislocations*. Oxford, United Kingdom: Elsevier, 2011, vol. 37.

[110] J. Burgers, "Geometrical considerations concerning the structural irregularities to be assumed in a crystal," *Proceedings of the Physical Society*, vol. 52, no. 1, p. 23, 1940.

[111] Z. Liu, "Microstructure evolution under tribological loading and its elementary mechanisms," Karlsruhe, [2018], iMD-Felder maschinell generiert (GBV)la. [Online, retrieved on 2020.11.23]. Available: http://dx.doi.org/10.5445/IR/1000085322;http://nbn-resolving.de/urn:nbn:de:swb:90-853224;http://d-nb.info/1165143186/34;https://publikationen.bibliothek.kit.edu/1000085322

[112] K. Mingard, M. Stewart, M. Gee, S. Vespucci, and C. Trager-Cowan, "Practical application of direct electron detectors to EBSD mapping in 2D and 3D," *Ultramicroscopy*, vol. 184, pp. 242–251, 2018.

[113] S. Schreijäg, D. Kaufmann, M. Wenk, O. Kraft, and R. Mönig, "Size and microstructural effects in the mechanical response of α-Fe and low alloyed steel," *Acta Materialia*, vol. 97, pp. 94–104, 2015.

[114] J. Nye, "Some geometrical relations in dislocated crystals," *Acta Metallurgica*, vol. 1, no. 2, pp. 153–162, 1953.

[115] E. Kröner, "Allgemeine Kontinuumstheorie der Versetzungen und Eigenspannungen," *Archive for Rational Mechanics and Analysis*, vol. 4, no. 1, p. 273, 1959.

[116] E. Demir, D. Raabe, N. Zaafarani, and S. Zaefferer, "Investigation of the indentation size effect through the measurement of the geometrically necessary dislocations beneath small indents of different depths using EBSD tomography," *Acta Materialia*, vol. 57, no. 2, pp. 559–569, 2009.

[117] J. R. Rice, “Tensile crack tip fields in elastic-ideally plastic crystals,” *Mechanics of Materials*, vol. 6, no. 4, pp. 317–335, 1987.

[118] S. Bozhko, V. Glebovsky, V. Semenov, and I. Smirnova, “On the growth of tungsten single crystals of high structural quality,” *Journal of Crystal Growth*, vol. 311, no. 1, pp. 1–6, 2008.

[119] K. Rochlus, S. Slawik, and F. Mücklich, “Influences of the edge area preparation suitable for EBSD of ferrous materials of different degrees of hardness: Dedicated to prof. Günter Petzow on the occasion of his 90th birthday,” *Practical Metallography*, vol. 53, no. 7, pp. 393–407, 2016.

[120] J. Chen, “On the determination of coating toughness during nanoindentation,” *Surface and Coatings Technology*, vol. 206, no. 13, pp. 3064–3068, 2012.

[121] J. Den Toonder, J. Malzbender, G. De With, and R. Balkenende, “Fracture toughness and adhesion energy of sol-gel coatings on glass,” *Journal of Materials Research*, vol. 17, no. 1, pp. 224–233, 2002.

[122] Agilent Nano Indenter, “G200,” *User’s Guide, Agilent Technologies*, 2009.

[123] J. Pethica and W. Oliver, “Ultra-microhardness tests on ion implanted metal surfaces,” *MRS Proceedings*, vol. 7, p. 373, 1981.

[124] R. L. Smith and G. Sandly, “An accurate method of determining the hardness of metals, with particular reference to those of a high degree of hardness,” *Proceedings of the Institution of Mechanical Engineers*, vol. 102, no. 1, pp. 623–641, 1922.

[125] W. C. Oliver and G. M. Pharr, “Measurement of hardness and elastic modulus by instrumented indentation: Advances in understanding and

refinements to methodology," *Journal of Materials Research*, vol. 19, no. 1, pp. 3–20, 2004.

[126] B. Lucas and W. Oliver, "Indentation power-law creep of high-purity indium," *Metallurgical and Materials Transactions A*, vol. 30, no. 3, pp. 601–610, 1999.

[127] T. Volz, "Deformation behavior of tungsten single crystals during wedge nanoindentation - a numerical study," Karlsruhe, [2020]. [Online, retrieved on 2020.11.23]. Available: http://dx.doi.org/10.5445/IR/1000120178

[128] F. Humphreys, "Review grain and subgrain characterisation by electron backscatter diffraction," *Journal of Materials Science*, vol. 36, no. 16, pp. 3833–3854, 2001.

[129] H.-J. Bunge, "The orientation distribution function of the crystallites in cold-rolled and annealed low-carbon steel sheets," *physica status solidi (b)*, vol. 26, no. 1, pp. 167–172, 1968.

[130] "MTEX toolbox." [Online, retrieved on 2020.11.23]. Available: https://mtex-toolbox.github.io/

[131] T. Skippon, "GND analysis by MTEX toolbox." [Online, retrieved on 2020.11.23]. Available: https://github.com/tskippon/GND

[132] A. Leitner, V. Maier-Kiener, and D. Kiener, "Dynamic nanoindentation testing: is there an influence on a material's hardness?" *Materials Research Letters*, vol. 5, no. 7, pp. 486–493, 2017.

[133] R. Lowrie and A. Gonas, "Single-crystal elastic properties of tungsten from 24 to 1800°C," *Journal of Applied Physics*, vol. 38, no. 11, pp. 4505–4509, 1967.

[134] B. Bergman, "On the estimation of the Weibull modulus," *Journal of Materials Science Letters*, vol. 3, no. 8, pp. 689–692, 1984.

[135] Y. Ye, Z. Lu, and T. Nieh, "Dislocation nucleation during nanoindentation in a body-centered cubic TiZrHfNb high-entropy alloy," *Scripta Materialia*, vol. 130, pp. 64–68, 2017.

[136] T. Volz, "Unpublished result," 2020.

[137] F. Javaid, Y. Xu, E. Bruder, and K. Durst, "Indentation size effect in tungsten: Quantification of geometrically necessary dislocations underneath the indentations using HR-EBSD," *Materials Characterization*, vol. 142, pp. 39–42, 2018.

[138] A. Argon, *Strengthening mechanisms in crystal plasticity*. Oxford, United Kingdom: Oxford University Press on Demand, 2008.

[139] E. Meieran and D. Thomas, "Structure of drawn and annealed tungsten wire," *Trans. Met. Soc. AIME*, vol. 233, p. 937, 1965.

[140] J. W. Kysar and C. L. Briant, "Crack tip deformation fields in ductile single crystals," *Acta Materialia*, vol. 50, no. 9, pp. 2367–2380, 2002.

[141] M. Rester, C. Motz, and R. Pippan, "Microstructural investigation of the volume beneath nanoindentations in copper," *Acta Materialia*, vol. 55, no. 19, pp. 6427–6435, 2007.

[142] R. Garlick and H. Probst, "Investigation of room-temperature slip in zone-melted tungsten single crystals," 1964. [Online, retrieved on 2020.11.23]. Available: https://core.ac.uk/download/pdf/80679072.pdf

[143] C. R. Weinberger, B. L. Boyce, and C. C. Battaile, "Slip planes in BCC transition metals," *International Materials Reviews*, vol. 58, no. 5, pp. 296–314, 2013.

List of Figures

List of Tables

A Appendix

A.1 Comparing the Young's modulus of dynamic and quasi-static nanoindentation

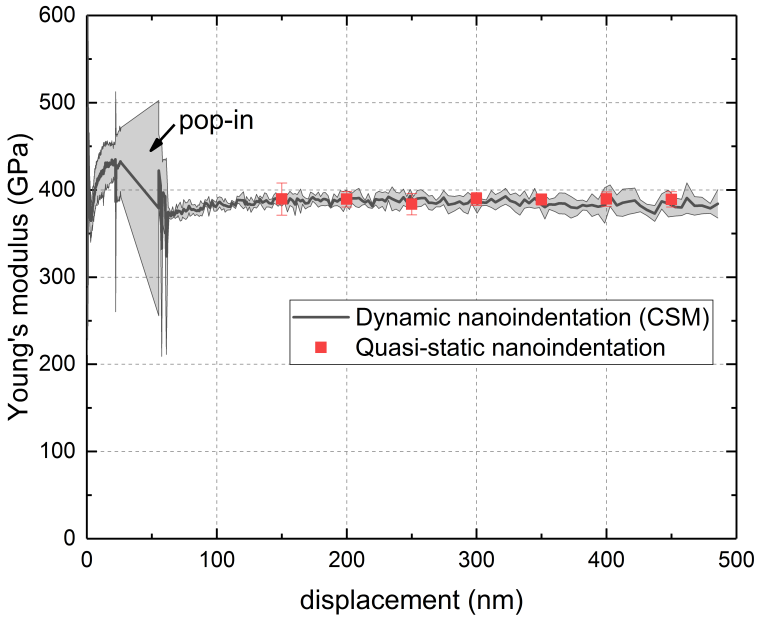

Figure A.1
Young's modulus determined using the dynamic and quasi-static nanoindentation. The measurement was conducted on the (001) tungsten single crystal using the G200 DCM II.

A.2 Schema of determining the lattice rotation maps

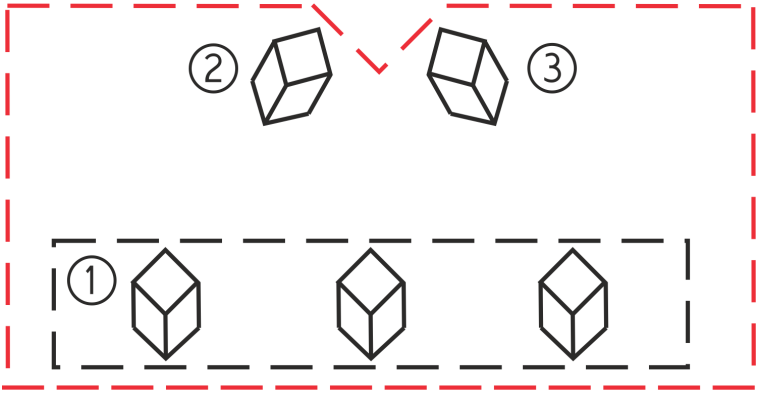

Figure A.2
Schematic of determining the lattice rotation distribution by comparing the Euler angles of materials from the deformed to undeformed area. The cross section framed by the red dash line indicates the area of the TKD measurement. in the area away from the indent, which is marked by the black dashed frame ①, the material does not deform and the Euler angles' values reflect the original crystallographic orientation. These references would be compared to the Euler angles determined from the deformed area beneath the indent, as marked by ② and ③.

A.3 Analysis method to calculate the mean GND density

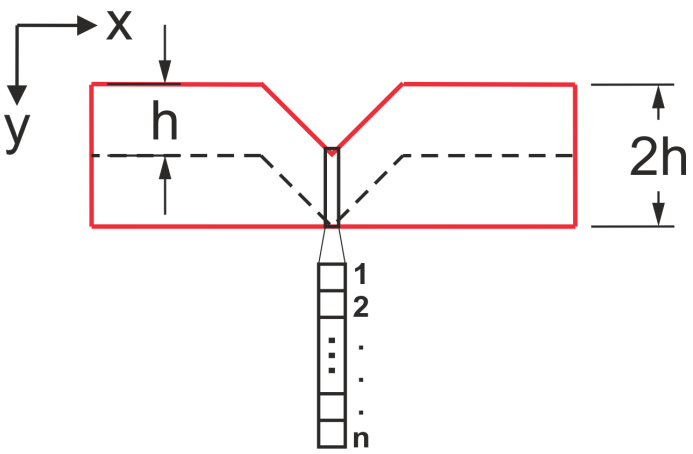

Figure A.3
Schema of the averaging method for the calculation of mean GND density along the *x* direction. Red frame indicated the cropped raw data area. The involved area to average the data was marked by the black dashed line. From the indent center deep down, the data volume of *h* contained *n* indexed points.

A.4 Independency of the pop-in effect to strain rate

Except in the CLR experiments, the pop-in effects were also observed in the CSR tests. For CSM tests, the pop-in load P_{pop-in} at eleven indentation strain rates were determined, then their maximum shear stress τ_{max} in accordance with each strain rate was calculated. Those results had been plotted over strain rates showing in Figure A.4. Both P_{pop-in} and τ_{max} were constant over strain rates, proved that they are strain rate insensitive in the range from 0.005 s^{-1} to 1.6 s^{-1} at room temperature.

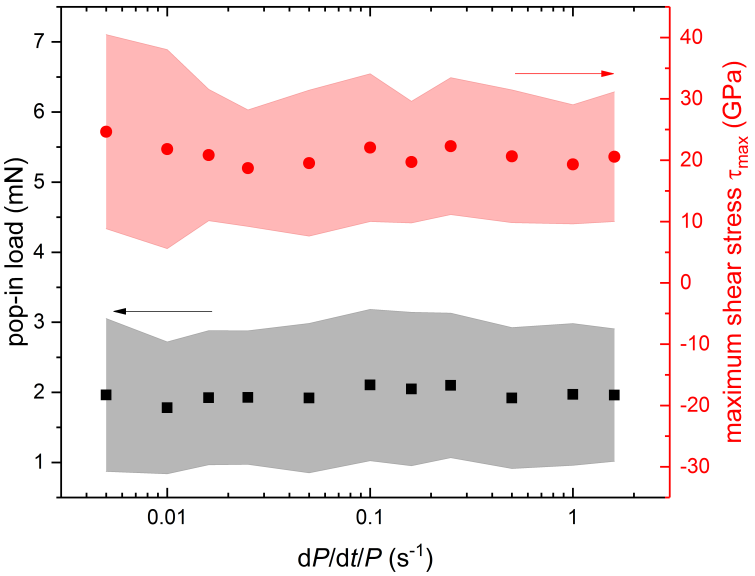

Figure A.4
Pop-in load and the corresponding maximum shear stress over eleven strain rates. The black and red points are the average values of P_{pop-in} and τ_{max} with the standard deviations indicated by the shadowed area, respectively.

A.5 Independency of the harmonic contact stiffness to strain rate

According to [71], non-linear ISE could be ascribed to the curved harmonic contact stiffness, which is related to the E/H ratio of a material. However, the harmonic contact stiffness values at different strain rates ranging from 0.005 s^{-1} to 0.05 s^{-1}, in the range the significant bi-linear ISE was observed (Figure 5.4), overlap and show a linear behavior to the indentation depth (Figure A.5).

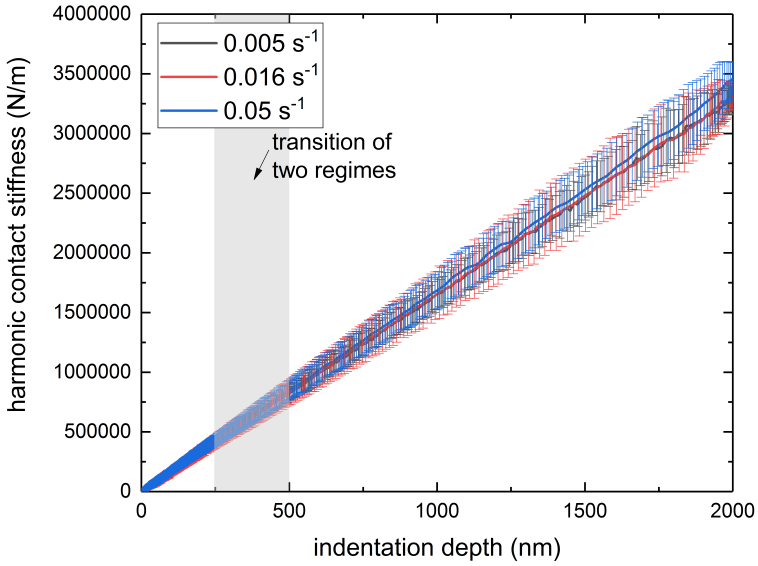

Figure A.5
Harmonic contact stiffness over indentation depth at different strain rates. For each strain rate, average values are shown together with their standard deviations.

A.6 Qiu's friction model

The ISE model introducing the Peierls stress into the Nix-Gao model [9] was carried out by Qiu et al. [68] and shown as:

$$\frac{H}{H_0} = \frac{3\sigma_0}{H_0} + \sqrt{\left(1 - \frac{3\sigma_0}{H_0}\right)^2 + \frac{h^*}{h}} \tag{A.1}$$

with H_0 and h^* the same parameter in Nix-Gao model [9], i.e. the depth-independent hardness and the material characteristic length scale. The Peierls stress σ_0 was introduced.

B Tables

Table B.1
Mechanical and electrolytic polishing process of tungsten single crystals.

	solution	**grind / grain size**	**force / voltage**	**time (flow rate)**
mechanical polishing				
SiC-paper	water	320, 600, 800, 1200	-	10 min
polishing clothes	diamond suspension	9 µm, 6 µm, 3 µm, 1 µm	75 N	15 min
	OP-A	0.06 µm	65 N	30 min
electrolytic polishing				
-	2% NaOH	-	10 V	30 s (10)

Table B.2
The depth-independent hardness H_0 and the characteristic length scale h^* of the (001) tungsten single crystal determined at nine strain rates by fitting the Nix-Gao model to the experimental data. For the strain rate of 0.05 s^{-1}, H_0 and h^* of the (112) orientation were determined and listed in this table in brackets.

Strain rate / s^{-1}	**0.005**	**0.010**	**0.016**	**0.025**	**0.050**	**0.100**	**0.160**	**0.250**	**0.500**
H_0 **/ GPa**	3.98	4.21	4.24	4.22	4.39 (4.43)	4.61	4.67	4.83	5.10
h^* **/ nm**	397.79	324.77	368.44	428.76	427.77 (328.18)	375.74	425.76	410.69	425.66